Characterization and Simulation of Non-Line-Of-Sight Fixed Wireless Links for Smart Grid Applications

by

Sina Mashayekhi

B.Sc., Amirkabir University of Technology, 2008

M.Sc., University of Manitoba, 2011

A THESIS SUBMITTED IN PARTIAL FULFILLMENT OF
THE REQUIREMENTS FOR THE DEGREE OF

DOCTOR OF PHILOSOPHY

in

THE FACULTY OF GRADUATE AND POSTDOCTORAL STUDIES
(Electrical and Computer Engineering)

THE UNIVERSITY OF BRITISH COLUMBIA
(Vancouver)

July 2016

Abstract

Electric power utilities are deploying wireless networks operating in mesh and point-to-multipoint configurations over near- and non-line-of-sight (NLOS) fixed links in tremendous numbers to support advanced metering and distribution automation applications. However, effective techniques for characterizing and simulating NLOS channels are required to support efficient implementation, deployment and operation of such networks.

In Part I, we contribute to techniques for small-scale channel characterization by: 1) proving the equivalence of the Ricean fading distributions observed in the delay, spatial and frequency domains and their relationship to fading observed in the temporal domain, 2) demonstrating the advantages of estimating the Ricean K-factor from channel frequency response data, and 3) revealing the conditions under which the channel impulse response can be estimated from scalar frequency response data using the Hilbert transform. In addition, we propose a method for estimating the noise floor in measurement-based estimates of the channel impulse response that allows more accurate estimation of delay spread.

In Part II, we contribute to the practical use of Loosely Synchronous (LS) pseudorandom codes to characterize dynamic MIMO channels by: 1) revealing the manner in which the autocorrelation and cross correlation properties of LS codes degrade when channel SNR is low and under reduced bit resolution using both simulation and measurement approach and 2) showing how fibre delay lines can be used to permit a single-port channel receiver to effectively measure the response of multiple receiving antennas simultaneously. This allows configuration of channel measurement equipment that captures the channel response in real time faster than the similar single-port channel sounders developed with switches.

In Part III, we contribute to simulation of fixed wireless networks in suburban macrocell environments by demonstrating how shadow fading varies as a function of terminal height and building height distribution and the manner in which it affects the system coverage.

The results contribute to the simulation and modeling framework developed by the National Institute of Standards and Technology (NIST) by more effective characterization and simulation of fixed wireless channels and better coverage and deployment cost estimation for Smart Grid applications.

Preface

This thesis presents research conducted by Sina Mashayekhi under the supervision of Prof. David G. Michelson in the Radio Science Lab (RSL) at the University of British Columbia, Vancouver campus.

Hamed Noori, Zahra Vali and Theodoros Mavridis contributed to the discussions and the simulation results presented in Chapters 2 and 3. Results from Chapter 3 were presented at *IEEE APS/USNC-URSI 2016* in June 2016.

During development of the MIMO channel sounder presented in Chapters 4 and 5, Siamak Bonyadi assisted with thoughtful discussions for developing design formulas. Ajay Singh assisted with simulation analysis of sounding sequences in Chapter 4. Chris Gillis also provided a technical assistant for implementing the MIMO transmitter. Preliminary results from Chapters 4 and 5 were presented at *IEEE APS/USNC-CNC-URSI 2015* in June 2015. Additional results were presented at *IEEE APS/USNC-URSI 2016* in June 2016.

Boubacar Diallo provided the measurement data used in Chapter 6. Preliminary results from Chapter 6 were presented at *IEEE APS/USNC- URSI 2012* in June 2012. A poster based on this chapter was presented at the UTC Canada Conference in September 2012. Additional results were presented at *IEEE APS/USNC-URSI 2016* in June 2016.

Table of Contents

List of Tables

List of Figures

List of Abbreviations

AC	Auto Correlation
ADC	Analog to Digital Convertor
AM	Advanced Metering
AWGN	Additive White Gaussian Noise
BER	Bit Error Rate
BS	Base Station
BW	Band Width
CC	Cross Correlation
CDM	Code Division Multiplexing
CDMA	Code Division Multiple Access
CFR	Channel Frequency Response
CIR	Channel Impulse Response
CW	Continuous Wave
DA	Distribution Automation
DR	Dynamic Range
DSSS	Direct Sequence Spread Spectrum
EM	Expectation Maximization
FDM	Code Division Multiplexing
FFT	Fast Fourier Transformation
GMM	Gaussian Mixture Model
GTD	Geometric Theory of Diffraction
HT	Hilbert Transform
IFFT	Inverse Fourier Transformation
IFW	Interference Free Window

KS	Kolmogorov Smirnov
LO	Local Oscillator
LOS	Line-of-Sight
LS	Loosely Synchronous
LTI	Linear Time Invariant
LTV	Linear Time Variant
MIMO	Multi Input Multi Output
ML	Maximum Likelihood
MoM	Method of Moment
MPC	Multipath Component
MS	Mobile Station
NB	Narrow Band
NIST	National Institute of Standards and Technology
NLOS	Non-Line-of-Sight
PDP	Power Delay Profile
PN	Pseudo Noise
PPS	Pulse Per Second
RBH	Random Building Height
RMS	Root Mean Square
PRBS	Pseudorandom Binary Sequence
Rx	Receiver
SF	Shadow Fading
SG	Smart Grid
SINR	Signal to Interference and Noise Ratio
SISO	Single Input Single Output
SNR	Signal to Noise Ratio

STD	Standard Deviation
TDM	Time Division Multiplexing
TS	Terminal Station
TWDP	Two-Wave with Diffuse Power
Tx	Transmitter
USRP	Universal Software Radio Peripheral
VNA	Vector Network Analyzer
ZCZ	Zero Correlation Zone

List of Symbols

r	Signal's amplitude
a_{i}	i'th multipath component's amplitude
t	Time parameter
τ_{i}	i'th multipath component's time of arrival
θ_{i}	i'th multipath component's phase
N	Number of multipath components
$h(.)$	Channel impulse response
f	Frequency parameter
$H(.)$	Complex frequency response
PDP	Power delay profile
P_0	Power of spike component in exponentially decaying power delay profile model
α	Slope of exponentially decaying power delay profile model
$u(.)$	Step function
$\delta(.)$	Delta Dirac function
K_τ	Ricean K-factor obtained from delay domain data
K_f	Ricean K-factor obtained from frequency domain data
τ_{N}	The delay instant when the applied noise threshold intersects power delay profile
N_{Th}	Noise threshold level
τ_{RMS}	RMS delay spread
τ_0	Mean excess delay
$V[.]$	Variance function
$E[.]$	Expected value
M_i	number of zeros inside the unit circle
P_i	number of poles inside the unit circle
M_o	number of zeros outside the unit circle
P_0	number of poles outside the unit circle
$\psi(.)$	Hilbert operator

LS_i	*i*'th Loosely Synchronous code
W_0	Interference free window zone length in bits
L_{Gol}	Length of Golay sequence
η	Energy efficiency
$R_{ij}(.)$	Cross correlation between sequence *i* and *j*
M	Family size of the sequence
L	Sequence length
B	Channel bandwidth
N_0	Noise power spectral density
L_S	Length of the sequence in bits
T_{IFW}	Window of interference free window in bits
T_c	chip rate
T_s	Time resolution
t_0	Absolute delay of propagation channel
T_D	Delay due to fibre delay line
τ_{max}	Environment maximum excess delay
N_f	number of frames captured within each trigger
ε	Delay line dielectric permittivity
$L(.)$	Propagation pathloss
L_0	Free space pathloss
L_{md}	Multiple-diffraction loss
L_{rtr}	Last building to receiver loss
λ	wavelength
μ_{hB}	Mean building height
σ_{SF}	Shadow fading standard deviation
$H_k(.)$	Field strength on k'th screen
h_{BS}	Base station height
Γg	Ground reflection coefficient
b	Building separation
P_{edge}	Edge coverage probablity

P_{area}	Area coverage probablity
α_{i}	Mixing portion of i'th component of mixture distribution
μ_{i}	Mean of i'th component of mixture distribution
σ_{i}	Standard deviation of i'th component of mixture distribution
D	Separation of the means relative to their width in GMM model

Acknowledgements

I would like to express my sincere appreciation and gratitude to my supervisor, Prof. David G. Michelson without whom the completion of this undertaking could not have been possible. His unwavering support, mentorship and valuable advice inspired me to continue challenging journey of Ph.D. program with more strength and confidence.

I would also like to express my profound gratitude to my committee members, Prof. Cyril Leung and Prof. Jane Wang for reviewing the dissertation. I would also like to thank the experts from BC Hydro and Powertech Labs who were involved in different stages of this thesis including Eugene Crozier, Vidya Vankayala and Sol Lancashire by providing valuable technical consultations.

I would like to thank the National Science and Engineering Research Council of Canada (NSERC), NSERC Smart Microgrid Network (NSMG-Net) and UBC Graduate and Postdoctoral Studies for supporting my Ph.D. research through Graduate Research Assistantships and Award. The kind support from Rhode and Schwarz (R&S) for providing us with measurement equipment is also acknowledged.

Finally, I wish to extend my profound gratitude to my parents and all individuals at UBC specially my friends at Radio Science Lab (RSL) for providing me with unfailing support and continuous encouragement throughout my years of study and through the process of researching and writing this thesis. This accomplishment would not have been possible without them. Thank you.

Dedication

To my dear parents.

Chapter 1:
Introduction

Electric power utilities rely on wireless communications to help monitor and control the geographically dispersed elements of the electric power distribution system. The system is conventionally divided into four functional blocks: Generation, Transmission, Distribution, and Customer, as depicted in Figure 1.1. Until the advent of grid modernization, the bulk of the wireless communications equipment used by electric power utilities was deployed within the generation and transmission infrastructure and used to implement a relatively small number of highly engineered and highly reliable point-to-point line-of-sight links. As grid modernization extends the wireless communications infrastructure past the distribution substations into the distribution grid and customer premises, wireless networks with hundreds of thousands to millions of nodes are being deployed to support Advanced Metering (AM) and Distribution Automation (DA) applications. Unlike the generation and transmission wireless infrastructure, such networks operate in mesh and point-to-multipoint configurations over near- and non-line-of-sight (NLOS) paths and individual links cannot be engineered. Accordingly, a different approach to link modeling and design is required.

Many organizations and user groups have developed guidelines and standards for such communication systems during the past decade [1]–[3]. Of particular note is the modeling and simulation framework developed by the U.S. National Institute of Standards and Technology

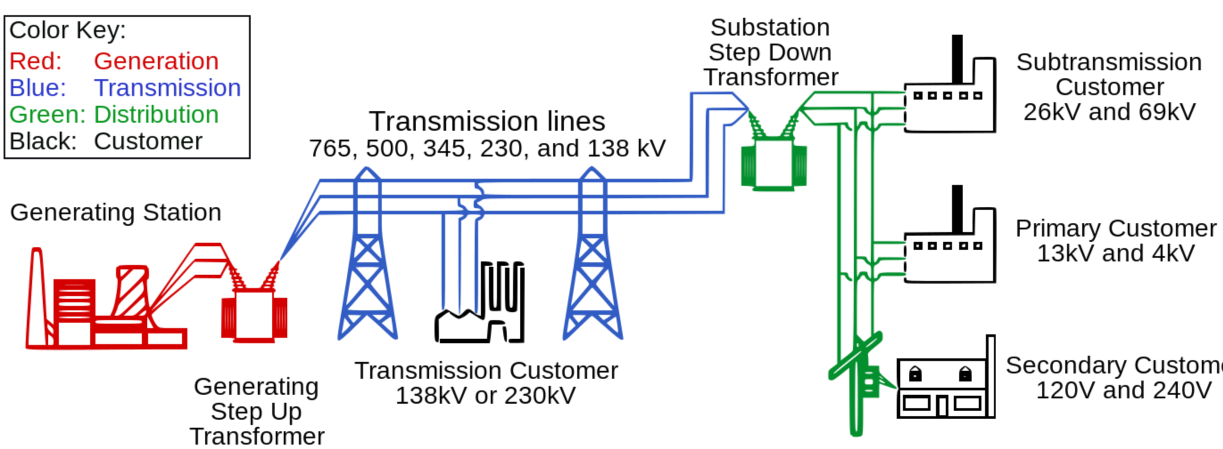

Figure 1-1: Elements of the electric power distribution system.

(NIST) to assist those charged with assessing the performance of alternative wireless technologies for use in such applications [4], [5]. The stringent performance requirements of such systems and the harsh environment in which they are being deployed put significant burden on the designers. What works for common carriers or legacy point-to-point control systems dates from several decades ago may not work for today's utility modernized system. This is mainly because design of Smart Grid (SG) systems is totally driven by the geographical location and distribution of sensors and Intelligent Electronic Devices installed in the field. As the number of these links increases dramatically, they cannot be engineered individually to achieve expected coverage and performance because of the huge cost associated with it. The general modeling framework developed by NIST PAP02 working group produces an analytical structure that is flexible for users to employ a variety of modeling techniques and the proposed wireless technology's parameters. The main building blocks of this tool are depicted in Figure 1-2 [4]. The main components are the PHY model, MAC sublayer, a module that performs coverage analysis, a channel propagation model and a model for multi-link. As seen in this figure, the propagation model block is an important part of this tool and the results obtained in higher sublayers directly depends on the accuracy of this block.

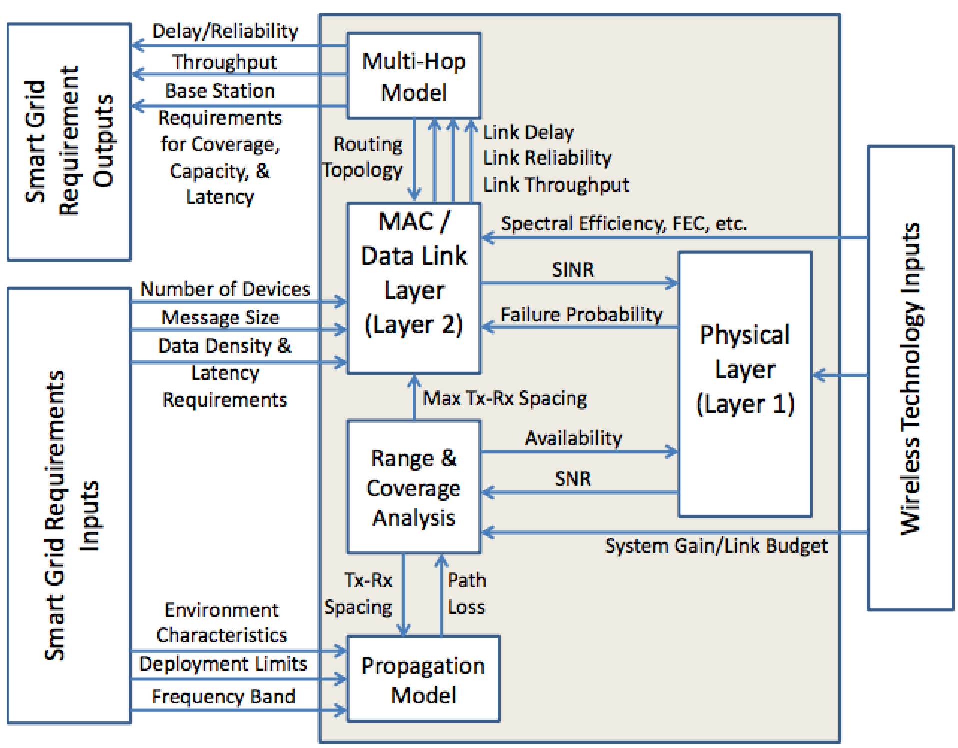

Figure 1-2: NIST wireless modeling tool framework building blocks [4]

The measurement setups in order to collect experimental data and the techniques to analyze them to generate reliable propagation model needs to be cost/time effective and at the same time accurate enough. The current thesis is mainly emphasizes on identifying the gaps and improving them within this module by several contributions which is described thoroughly in the rest of this section and within each of the chapters.

Effective techniques for characterizing and simulating NLOS channels are required to support efficient implementation, deployment and operation of such networks. Due to large number of communication nodes, a statistical approach to simulate and characterize of these links will be the key. Although several solutions have been proposed for NLOS SG communications, propagation impairments and over/under estimation of their impacts on system performance have been cornerstone and a serious challenge [6], [7]. In a typical macrocell environment, due to NLOS, propagation impairments such as fast fading and slow fading are the main factors degrading signal quality therefore systems capacity and coverage and need to be carefully studied. Multiple-Input Multiple-Output (MIMO) has been proven as an effective wireless technology to increase diversity and mitigate the effects of channel fading [8], [9].

Accurately characterized MIMO channels will give valuable insights in designing systems that are more resistant to propagation impairments. Based on the urgent needs of our industry partners, importance and relevance of the subject, the limitations we observed in the NIST framework model, and motivations from previous works, we have devoted this thesis to study NLOS fading characterization, mainly focusing on developing techniques to estimate Ricean K-factor in the presence of noise, study the effect of large scale fading on system performance in a suburban SG propagation environment and developing a novel technique for MIMO channel sounding applicable to those environments, as described briefly in the following paragraphs and in more details through the next chapters.

Ricean fading naturally occurs when NLOS wireless channels include both a strong direct component and weaker scattered components. The instantaneous amplitude of the received signal is characterized by a Ricean distribution of which the K-factor is a parameter. The Ricean K-factor is an important metric of channel quality and much effort has been devoted to developing techniques for estimating the Ricean K-factor [10]–[13]. These methods have been mainly using narrow band (NB) signal measurements to estimate K-factor, *i.e.*, using measured Channel Impulse Response (CIR) of NB channels and Continuous Wave (CW) space-domain measurements. This is mainly because historically CW measurement in spatial domain was easy to do compared to frequency domain one. However, today VNA-based measurements are more frequent and easier to perform which signifies importance of developing practical methods to estimate channel parameters such as Ricean K-factor and RMS delay spread from Channel Frequency Response (CFR).

Traditionally, estimation of K-factor from such measurements is carried out by transferring data into time domain using Inverse Fourier Transformation (IFFT) and applying proper noise thresholding and filtering techniques in order to clean the response. This has been proven to be a rigorous task specially the effect of environment noise on measured response makes accurate detection of specular and diffused multipath components even more difficult. Few previous studies have developed frequency models to obtain K-factor directly from CFR[14]. However, the relationship between different Ricean distribution traditionally observed in time and space with the one obtained from frequency domain response and effect of channel signal to noise ratio (SNR) on estimation of K in each domain has not been presented. Hilbert transform technique has been proven to be a useful method to estimate time domain CIR from scalar response considering the fact that it is generally easier to measure scalar than complex CFR [15]. However, the conditions under which this technique reveals an acceptable estimation error is not very well defined to be practical for on-site measurements.

In Part I of the thesis, we contribute to techniques for estimating the Ricean K-factor and overcome key limitations of previous work. In Chapter 2, we: 1) prove the equivalence of the Ricean fading distributions observed in the delay, spatial and frequency domains and their relationship with fading observed in the temporal domain and 2) demonstrate the advantages of estimating the Ricean K-factor from channel frequency response data. In addition, 3) we propose a method for estimating the noise floor in measurement-based estimates of the channel impulse response that allows more accurate estimation of delay spread. In Chapter 3, we reveal the conditions under which the channel impulse response can be estimated from scalar frequency response data using the Hilbert transform and we study the amount of error Hilbert may cause in different metrics of the Ricean channel, *e.g.* delay spread, in a quantified representation.

During the past fifteen years, MIMO wireless technology has emerged as an important technique for improving the capacity and reliability of NLOS links. Many options exist for measuring static and semi-static MIMO channels such as Single-Input Single-Output (SISO), Time Domain Multiplexing (TDM), Frequency Domain Multiplexing (FDM) and Code Division Multiplexing (CDM)-based MIMO channel sounders [16]–[19]. However, measuring dynamic MIMO channels is more challenging. Most conventional techniques for characterizing MIMO wireless channels are only suitable for characterizing quasi-static channels [20]. Current popular channel sounders in which switches are used to alternate between different polarizations of transmitter antennas in MIMO measurements suffer from additional delay due to switching time which affects the accuracy of the measurement in fast varying channels [21].

More sophisticated MIMO channel sounders that employ spread spectrum transmitters and receivers with multiple channels, each connected to dedicated antennas, allow all possible transmit and receive antenna combinations to be characterized simultaneously and therefore obtain accurate fading correlation estimates but at considerable added expenses [22]. Moreover, simultaneous measure of channels requires the spreading codes to be carefully chosen to ensure highest possible peak value of auto-correlation function and lower correlation peaks (side-lobes) at non-zero time-shifts in order to eliminate the effects of multiple access interference at the receiver. But no such code family exists which possess both characteristics simultaneously according to Welch bounds [23]. There has been an exhaustive effort to evaluate the peak correlation characteristics of various spreading codes and suggest suitable solutions [24]. Certain sets of Loosely Synchronous (LS) codes exhibit good auto and cross correlation properties, they can be transmitted together and used to recover the channel impulse response over different transmission paths simultaneously [16]. However, most previous analyses have assumed ideal SNR (*i.e.*, noise free) and ideal bit resolution.

Considering the challenges mentioned above, there is a need to reform the architecture of MIMO channel sounder in order to overcome limitations in measuring MIMO channel responses in fast varying environments. In Part II of the thesis, we contribute to the practical use of LS pseudorandom codes to characterize dynamic MIMO channels. In Chapter 4, particularly we reveal the manner in which the autocorrelation and cross correlation properties of LS codes degrade with decreasing SNR and reduced bit resolution. In Chapter 5, we show how LS coded transmissions can be combined with our new technique for using fibre delay lines to permit a single channel receiver to effectively characterize multiple receiving antennas simultaneously to realize a particularly simple and effective dynamic MIMO channel sounder.

Simulation of entire wireless networks requires that large scale phenomena to be characterized and system models to be developed. SG application requirements impose different deployment scenarios compared to traditional cellular networks such that the devices supporting these applications can be in locations that are not ideal for wireless communications since their siting requirements are based on meeting their utility requirements rather than meeting common and third party carrier's requirements. For an example, today many DA field devices are mounted on pole-top heights and are expected to perform better in terms of link budget compared to low height installations [209]. However, the behavior of Shadow Fading in Macrocell suburban environment with respect to terminal height may indicate otherwise resulting unexpected system connectivity and coverage degradation.

Variation of path loss with terminal height in suburban environments is well-characterized [26]–[28] but only anecdotal observations of the variation in shadow fading with terminal height have been reported [29], [30]. Most of the works in this area are based on the assumption of having static shadow fading with static standard deviation which doesn't change regardless of terminal heights and recent studies have emphasized on a need for developing models for it [31]. A comprehensive understanding of the shadowing behavior with terminal height will play a key role in designing these emerging SG wireless networks. In Part III (Chapter 6), we contribute to simulation of fixed wireless networks in suburban macrocell environments. We demonstrate how shadow fading varies as a function of terminal height and building height distribution and the manner in which this affects the system link budget and coverage.

In Chapter 7, we conclude the thesis with a discussion of the effectiveness of our proposed schemes, any unexpected outcomes that we encountered, and the implications for current practice and future research, including more effective characterization and simulation of fixed wireless channels for SG applications. Aligned with the NIST framework's model, the final outcome of this thesis will be proposing significant improvements to methods used to estimate small-scale channel parameters, characterize MIMO wireless channels, simulate large scale wireless networks in suburban environments aiming for reducing the risk of over/under designing the communication networks, thereby incurring unwanted expenses.

Chapter 2:
Practical Factors in the Estimation of Ricean K-factor in the Time, Frequency and Spatial Domains

2.1 Introduction

As described in Chapter 1, K-factor is a parameter of the Ricean distribution which models the instantaneous amplitude of received signal in a fading channel. Ricean K-factor is an important metric of channel quality and accurate estimation of it is critical for channel characterization, link budget calculations and adaptive modulation [32]. Moreover, the capacity and performance of MIMO channels and accuracy of velocity estimators in a wireless systems are a function of K-factor [33], [34]. Today, estimation of K-factor is even more importance. Back in 1970-80 traditional radios and mobile networks didn't require the knowledge of the Ricean K-factor since they were designed for the worst case operational scenario, *i.e.*, under Rayleigh fading assumption [35]. K-factor became an issue in mid-90s when the concept of NLOS fixed wireless system was introduced and became popular. These channels were varying but weren't mobile. In next 10 years, several papers were written showing up interests in estimation methods of K-factor. These methods were mostly using NB single carrier measurements to estimate K-factor [36]. This was mainly because historically CW measurement in spatial domain was easy to conduct compared to frequency domain measurement. However, today due to advent of high performance VNAs and multi-carrier channel sounders, such measurements can be routinely conducted [36]. So, clarifications on estimation of channel parameters specifically the Ricean K-factor from different domains, is an essential for efficient use of the data within each domain.

2.1.1 Methods for Estimating Ricean K-factor

K-factor can be difficult and tricky to measure in a physically meaningful manner because of challenges with isolating the direct signal from the scattered components. Moreover, having to deal with measurement data captured in different domains of frequency, time, and space, influence of environment such as noise, and deciding on a proper scenario of collecting data such as sampling rate and density can add to this complexity. There have been several works in the literatures concerning the estimation of the K-factor. One approach is to compute the distributions of the measured data, then compare the result to a set of hypothesis distributions using a suitable goodness-of-fit test [32]. Another approach has been the method of maximum likelihood (ML) [10], [37] which chooses the parameters of the Ricean distribution by solving nonlinear equations using an Expectation Maximization (EM) algorithm such that it maximizes the joint probability density of the observed outcome.

However, both of these approaches are relatively cumbersome and time consuming. The method of moment (MoM) can be generalized to be used with different moments of the recorded data [11], [12], [38]. *E.g.*, [11] uses the second and fourth moments of the signal to estimate K-factor. The MoM estimators are more practical compared to other methods to be applied in time, space and frequency domain fading data since it requires the power samples only [39]. However, other methods of Ricean K-factor estimation has been explored in previous studies such as using in-phase and quadrature components [13], Frequency domain approach [14], [40], and using the delay profile data [39], [41]. Despite the large number of literatures studying Ricean parameters the relation between the K-factors obtained from the data recorded in different domains is not clearly stated. This emphasizes on importance of studying the difference/relationship between Ricean K-factor observed by sampling in space, frequency, and delay domains.

2.1.2 Noise Thresholding

Estimating the channel parameters, especially the Ricean K-factor, is challenging in temporal and spatial domain measurements due to the difficulty of selecting proper noise threshold value to extract LOS and multipath components out of noisy CIR. It has been shown that noise threshold does not have a large effects on the calculation of the path loss, but does affect the calculation of the mean excess delay and RMS delay spread [42]. Interestingly, choosing different threshold level doesn't have linear effect on predicted channel parameters such as delay spread but has random discrepancy [43]. Not only isolating the direct signal from the scattered components is difficult, sometimes additional steps are required to also verify if LOS component exist in the Doppler delay spectrum (*e.g.*, by using GPS location of mobile and geographical map of the measurement site to verify LOS/NLOS records).

The ultimate consequence of the noise is causing the false detection and masking the weak rays in the responses especially under low channel SNR. This issue is more problematic in high frequencies in where the delay spread value reaches a maximum value far before the threshold used for delay spread calculation reaches the noise floor [44]. Effect of thresholding on channel parameter estimation has been shown in many studies [43], [45], *e.g.*, the impact on RMS delay spread was studies in [43] using three selected threshold values on measured data concluding that different threshold values can make large effects on estimated channel parameters. Or it was shown in [45] that 9 dB change of threshold value, can affect the predicted RMS delay spread value by a factor of two.

The problem of finding proper noise threshold value to separate multipath components and noise from time domain impulse response has gone under several studies [20], [25], [44], [46]. In [44] specific percentage of detected multipath components (MPC) is chosen such that the sum of the power of the selected paths reaches a desired ratio of total power. In [46], the lowest 25% of the delay profile amplitude points are sorted, and then the highest and the lowest 25% of these low amplitude points are removed (median filtering). The remaining low amplitude points are averaged to yield a power level that is the dynamic range noise floor. In [25], the noise level introduced by side-lobes of the windowing function which was used to obtain the time domain impulse response was assumed much higher than measurement noise floor. As a result, the side-lobe level of the rectangular window was selected as noise threshold.

In [20], the noise threshold was argued to be selected as a function of noise level since only thermal noise was considered. Similar method was used in [42], [47]. Beside these methods, many authors also have considered specific dB value below the peak of the CIR (15-30 dB) as noise cut off [48], [49] or a varying threshold decision which depends on the dynamical noise floor and the peak value of CIR [50], [51]. However, most of the above mentioned algorithms are complicated to implement, requiring rigorous impulse response inspection or are based on assumptions which may not be valid in the environment which measurements are taken. Therefore, a better-standardized technique is needed for interpretation and presentation of measured channel impulse response data. This problem is addressed in our work along with a proposed solution to estimate the noise threshold more accurately.

In the remainder of this chapter, we will show the equivalence of the Ricean fading distributions observed in the delay, spatial and frequency domains and demonstrate the advantages of estimating the Ricean K-factor from channel frequency response data especially when channel SNR is low. Then, we will propose an algorithm to estimate the noise threshold more accurately compared to conventional noise threshold estimators. We will explain our simulation details along with the results and will conclude the work in the discussion section.

2.2 Concept

2.2.1 Equivalence of Ricean K Factors in the Space, Delay and Frequency Domains

Unlike many studies that have considered spatial/temporal domain Ricean channel, several other related quantities can also follow equivalent Ricean distribution in a RF channel. To show this, consider the relation between delay and frequency domain representation of a channel response. The instantaneous complex envelope of the signal is phasor summation of the individual multipath components within a single channel impulse response as [52], [53]

$$r(t) = \sum_{i=0}^{N-1} a_i(t,\tau)\exp(j\theta_i(t,\tau)), \tag{2.1}$$

where $a_i(t)$ and $\theta_i(t)$ are ith MPC instantaneous amplitude and phase, respectively and N is the total number of components including LOS and MPCs. When the MPCs at each instant are summed to yield the resultant complex amplitude, the Central Limit Theorem applies and the it becomes a complex Gaussian process. When no dominant component is present, the envelope follows a Rayleigh distribution whereas when it is present, the envelope follows a Ricean distribution [54]–[56].

Considering tap-delay CIR model,

$$h(t,\tau) = \sum_{i=0}^{N} a_i(t)\delta(\tau - \tau_i),$$

where h(τ) is delay domain channel response and considering the linear time invariant (LTI) systems where dependence of $h(t,\tau)$ to parameter t can be ignored, then applying operation of Fourier transform on a snapshot of complex delay profile will result in

$$H(t_0, f) = \sum_{i=-\infty}^{+\infty} h(t_0,\tau_i)\exp(j2\pi f \tau_i)), \tag{2.2}$$

where $H(f)$ is the frequency domain channel response**.**

This indicates that each frequency point is in fact summation of effects of all multipath components phases and amplitudes and because of the randomness of these components (*i.e.*, randomness of only phases component in LTI channels and both phases and amplitude components in LTV channels), the Central Limit Theorem again applies here and results in a complex Gaussian process. As a result, the frequency domain data's amplitude will follow

Ricean distribution. Therefore, calculation of K-factor from frequency domain amplitude will be physically meaningful. The following paragraph argues that not only the amplitudes follow Ricean distributions in different domains, but also the first order statistics (*i.e.*, the K-factor) of these distributions are equal.

Rapid changes in the relative phases of multipath components may occur with shifts in frequency, position of the receiver, or the position of the scatterers over time. Because of the conservation of the energy, regardless of the type of the shift that occurs, the relative energy in the direct and scattered components is identical. So the Ricean K-factors that describe the fading distribution are also identical. As a consequence, we should see the same first-order distribution whether we vary the frequency, the position of the receiver or the position of the scatterers over time; only the sequences will be different. In next section we show the problem with estimating K factor from delay domain data (we will call it the *delay domain K-factor*) and show that noise threshold selection is the main challenge which can lead to biased calculations. Using the equivalence of K-factors in both domains we show the merits of using frequency domain data instead for calculating the K-factor (we will call it *frequency domain K-factor*).

2.2.2 Ricean K Factor Estimation in the Presence of Noise

Exponential decaying power delay profile with a spike has been observed and modeled in many typical propagation channels [41], [57]. PDP of such channel is expressed in (2.3) and is plotted in Figure 2-1.

$$PDP(\tau) = p_0\delta(\tau) + p_1 e^{-\alpha\tau} u(\tau)\,, \tag{2.3}$$

where p_0 and p_1 are amplitudes defined in Figure 2-1, α is exponential slope, $\delta(.)$ and $u(.)$ are Dirac and step function, respectively.

According to the definition of delay domain K-factor,

$$K = \frac{p_0}{\int_0^{\tau_N} PDP(\tau)d\tau}\quad , \tag{2.4}$$

where $\boldsymbol{\tau}_N$ is the delay instant when the applied noise threshold (the absolute value in dB) intersects the PDP. *i.e.*,

$$p_1 e^{-\alpha\tau} = N_{Th} \Rightarrow \tau_N = -\frac{1}{\alpha}\ln\frac{N_{Th}}{p_1}\ . \tag{2.5}$$

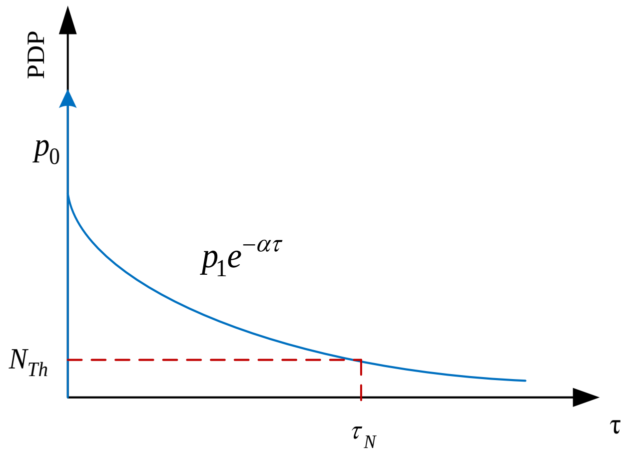

Figure 2-1: Exponentially decreasing power delay profile shape with a spike at LOS position.

In the case of a noise-free scenario, the upper bound of the integration in (2.4) becomes infinite. Using (2.3) and (2.4) K-factors can be calculated as (in linear units)

$$K_{NoiseFree} = \frac{p_0}{p_1}\alpha \ , \tag{2.6}$$

$$K_{Noise} = K_{NoiseFree}\frac{p_1}{p_1 - N_{Th}} \ , \tag{2.7}$$

where K_{Noise} is the calculated K-factor when PDP is thresholded By N_{Th}. Using (2.6) and (2.7) one can show the relative error of calculated K-factors in dB due to noise thresholding as

$$\text{Relative Error} = \frac{\Delta K}{K_{NoiseFree}} = \frac{K_{Noisefree}(dB) + 10\log_{10}(\frac{p_1}{p_1 - N_{Th}}) - K_{Noisefree}(dB)}{10\log_{10}(\frac{p_0}{p_1}\alpha)} \ , \tag{2.8}$$

$$\text{Relative Error} = \frac{\Delta K}{K_{NoiseFree}} = \frac{\log\frac{p_1}{p_1 - N_{th}}}{\log\frac{p_0}{p_1}\alpha}, \quad 0 \le \mathrm{N_{Th}} < p_1 \tag{2.9}$$

which shows dependence of the error on the value of noise threshold and parameters of the PDP, *i.e.*, exponential factor, α, and the specular and diffuse component amplitudes. The plots of relative error versus selected noise threshold will be presented in the result section of this chapter, later. It should be noted that in practice the effects of noise on channel response is not only at the tail of PDP but on every multipath component as well. For simplicity, here we present the effects of noise just at the tail of the PDP to show the effect and trend of noise thresholding and truncating on parameters of the channel. The dependence of RMS delay spread on noise threshold also can be investigated in the same manner as [58], [59]

$$\tau_{RMS} = \sqrt{\frac{\int_0^{\tau_N} (\tau - \tau_0)^2 PDP(\tau) d\tau}{\int_0^{\tau_N} PDP(\tau) d\tau}} = \sqrt{\tau_2 - \tau_0{}^2} \,, \tag{2.10}$$

where τ_2 is the second moment of the PDP and τ_0 is the mean delay spread and are defined as

$$\tau_0 = \frac{\int_0^{\tau_N} \tau PDP(\tau) d\tau}{\int_0^{\tau_N} PDP(\tau) d\tau} \,,$$
$$\tau_2 = \frac{\int_0^{\tau_N} \tau^2 PDP(\tau) d\tau}{\int_0^{\tau_N} PDP(\tau) d\tau} \,. \tag{2.11}$$

For noise-free PDP and zero specular component, (2.10) results in

$$\tau_{RMS} = \frac{1}{\alpha} \,, \tag{2.12}$$

which is consistent with previous studies [60]. In order to show the effect of noise thresholding on RMS delay spread for a channel with finite SNR, (2.10) is studied numerically and the results are presented later in this chapter. It is concluded that both Ricean K-factor and RMS delay spread in delay domain will depend on selected noise threshold value. This can make it a challenge to analyze measurement records when there is small LOS component or SNR is low since in these scenarios considering that noise has a random effect in time domain, it can change the amplitude of the recorded impulse response such that in NLOS and semi-NLOS channels distinguishing noise and MPC becomes difficult. This results in inaccurate K-factor estimation from delay domain records.

In the frequency domain, however, spectrum of the noise is spread over entire band and this makes noise effect less troublesome to calculate Ricean K-factor. This emphasizes the merits of using frequency domain data to calculate K-factor more accurately. Later, we will present the results on how frequency domain K-factor calculation is more robust to noise compared to delay domain and will conclude that obtaining K-factor from frequency domain will result in more accurate estimation. This robustness to noise also is used to develop an algorithm to estimate a noise floor for measurement data explained in next section to overcome the challenge of calculating channel parameter such as RMS delay from delay domain data.

2.2.3 A Bisection Algorithm for Estimating the Noise Threshold

As explained, the delay domain and frequency domain Ricean K-factors are equivalent. Considering this, the relation between noise threshold and Ricean K-factor developed in previous section and noting that K-factor calculation is more accurate in frequency domain than delay domain, a bisection algorithm is proposed as following. Given the frequency scalar response, K-factor can be estimated using MoM or Ricean fitting approach. Using IFFT, the CIR can be obtained which is noisy and based on different threshold value the profile shape will vary. By varying the noise threshold, in steps of 1 dB for example, and obtaining delay domain K-factor at each step, the plot or table of noise threshold versus K-factor can be created. Then the proper noise threshold will correspond to the value for which the delay domain K-factor is closest to the value calculated in frequency domain. The flowchart in Figure 2-2 summarizes these steps.

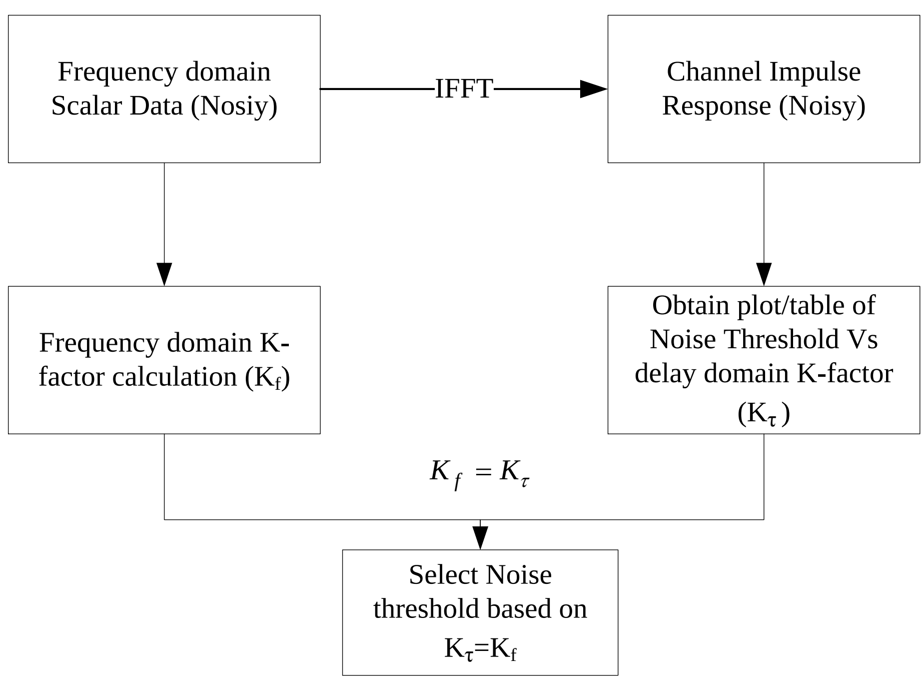

Figure 2-2: Flowchart of proposed bisection noise threshold detection algorithm.

2.3 Implementation

In this section, we will describe our MATLAB based Monte Carlo simulations and the methods we used in order to obtain K-factor parameter. In order to generate Ricean channel impulse responses with specific Doppler spectrum profile, we used the *ricianchan* object of the MATLAB [61]. The function requires sampling period, Doppler spectrum type, maximum Doppler shift, paths delays and average path gains. Without loss of generality, for the purpose of the simulations we chose these parameters for a typical channel with 25MHz channel bandwidth with Gaussian Doppler profile and a CIR with 12 multipath components of fixed arrival times. The average path gains were calculated as input of the ricianchan based on the exponential decaying function and desired K-factor [41]. Every time within the chapter when we talk about the effect of channel SNR on K estimation in delay or frequency domains, the noise is considered as additive white Gaussian.

Table 2-1 summarizes the parameter of the simulation.

Table 2-1: Simulation parameters

Channel BW	25MHz	**Number of MPCs**	12
Sampling period	10ns	**Path delays**	Uniformly distributed with 40ns delay separation
Range of K-factor channels realized with	0 dB - 40 dB with 1 dB step	**Average path gains**	Exponentially decaying, function of K-factor [41]
Range of SNRs simulations repeated with	5 dB - 30 dB with 1 dB step	**Doppler shift**	0Hz
Number of Monte Carlo simulation under each SNR value	1000	**Doppler spectrum**	Gaussian

Every time after the *ricianchan* was called, the response of the channel to the input signal of a Delta Dirac function was obtained using *filter* function. This created a Ricean CIR which we were interested in and we call it a *channel realization*. Noise was then added using *awgn* function of MATLAB based on the specific SNR value provided at the input of the function. The frequency domain transfer function was then obtained by Fourier transform. Following methods were used to calculate Ricean K-factors at each domain for the purpose of this chapter

The *K* in delay domain was calculated based on definition of the Ricean K-factor which is the relative power of LOS component, A^2, over the power of the sum of the other remaining rays constitute the scatter power, $2\sigma^2$. *i.e.,*

$$K = \frac{A^2}{2\sigma^2} \quad . \tag{2.13}$$

The *K*-factor in frequency domain was calculated by fitting the scalar response to MATLAB Ricean fit function and calculating the K-factor of the best fit. For comparison purposes, the K was also calculated using MoM algorithm described in [12]. The algorithm is based on the general expression for the *l*th order moment of the Rice distribution. *i.e.,* if the Rice probability density function of the received signal, *R(t)* is given by

$$f_R(r) = \frac{2(K+1)r}{\Omega}\exp(-K - \frac{(K+1)r^2}{\Omega})I_0(2\sqrt{\frac{K(K+1)}{\Omega}}r), \tag{2.14}$$

$$r \geq 0, K \geq 0, \Omega \geq 0 \,,$$

where $I_n(.)$ is the *n*th order modified Bessel function of first kind and $\Omega=E[R^2]$. Then K-factor can be calculated using

$$K = \frac{\sqrt{1-\gamma}}{1-\sqrt{1-\gamma}} \quad , \tag{2.15}$$

where

$$\gamma = \frac{V[R^2]}{(E[R^2])^2} = \frac{2K+1}{(K+1)^2} \quad , \tag{2.16}$$

and *V*[.] denotes the variance.

2.4 Results

In this section, we present the results obtained from MATLAB simulation for which the details were described above. The results cover all the formulations developed in the concept section and the simulation of the Ricean channel explained in previous section.

2.4.1 Equivalence of Ricean K-factors in the Delay and Frequency Domains

As argued, K-factor calculated in both delay and frequency domains should be equivalent. Here we confirm this using simulation results. Figure 2-3 is the results of 3600 noise-free channel realizations and then calculating both frequency and delay domain K-factor and plotting the scatter plots in dB units (the dB unit is chosen rather than the linear scale for better representation and resolution).

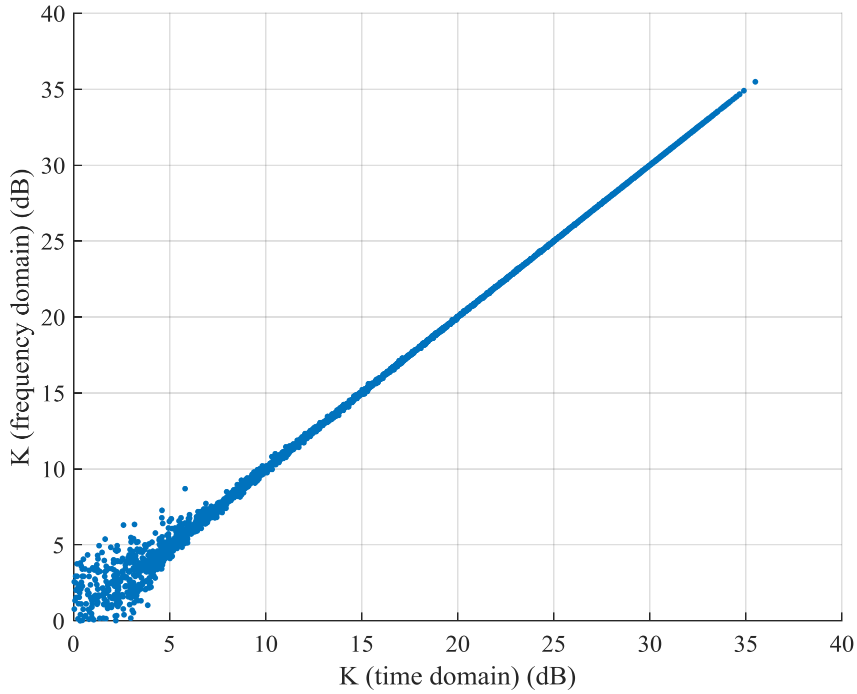

Figure 2-3: Scatter plot of Ricean K-factor in delay and frequency domains.

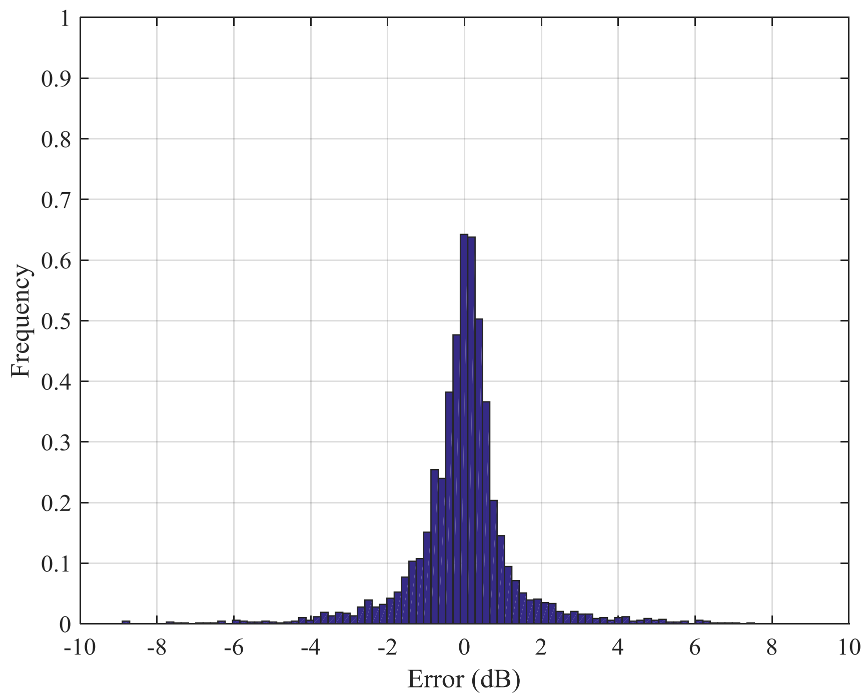

Figure 2-4: The normalized distribution of the error between K factors in delay and frequency domains

It is seen that the K-factor in both domains are well fitted on the linear line therefore there is equivalence relation. The K-factor estimation method in frequency domain loses precision at very low K-factors, *i.e.*, $K \leq 5$ dB. At the same time, the fading distribution does not change much over that range of K, so that imprecision in estimating the K is not impactful. The normalized distribution of this error ($Error = K_f - K_\tau$) is plotted in Figure 2-4. The error distribution is symmetric around the zero mean. It is a good practice to perform the goodness of fit test after applying a K-factor estimator, which usually is missing in many other similar studies. Here since Ricean fit function of MATLAB was used to obtain K-factors in frequency domain, we performed the goodness of fit test using Kolmogorov–Smirnov (KS) [62] null hypothesis test with 0.05 significance level. The results implied that in majority of the channel realizations (around 96%), the channels followed the Ricean distribution. Investigating the CDF of the channels that didn't pass the KS-test didn't show large differences with Ricean CDF and by increasing the significance level even more channels could pass this test.

2.4.2 Impact of Noise on Ricean K-factor Estimation in the Delay Domain

Estimating Ricean K-factor from CIR requires noise thresholding. In order to show the sensitivity of both K-factor and RMS delay spread to noise threshold we plotted these parameter versus noise threshold using first the theoretical formulas developed in previous section and then using the simulation of the Ricean noisy channel with details described in implementation sections.

a. Analytical Approach:

For the purpose of this section, without loss of generality, we assumed an exponential decreasing PDP with $P_1=10^{-2}$ and $a=10^{-2}$ and P_0=3.162 which corresponds to a channel with K = 5 dB according to the formulation presented in previous section. Figure 2-5 and Figure 2-6 show the effect of thresholding on relative error of the original and estimated K-factor and RMS delay spread after thresholding, respectively, in dB units. The *threshold value* here is the absolute value of noise threshold in dBW unit.

As it was expected, both K-factor and RMS delay spread are very sensitive to the selected noise threshold and the error may vary between 0% and 100%. In practice, these presented curves may change, showing more relative error since noise will affect the MPCs as well which was ignored in the analytical formulas. In the next section the channel simulation results will include the noise effect on each delay domain component as well and not just at the tails.

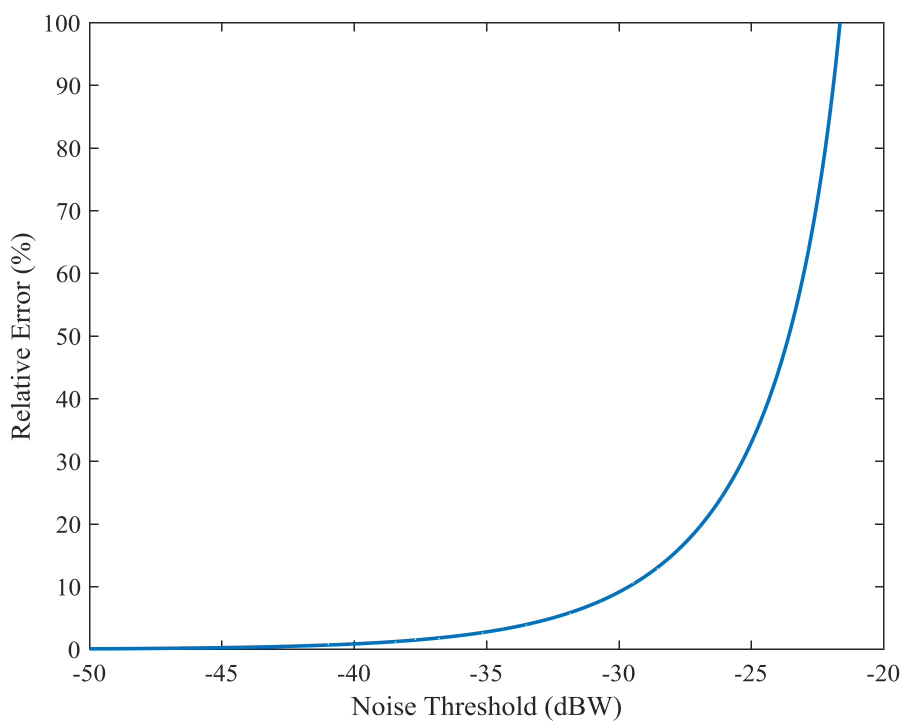

Figure 2-5: Sensitivity of delay domain K-factor to selected noise threshold (using analytical formula).

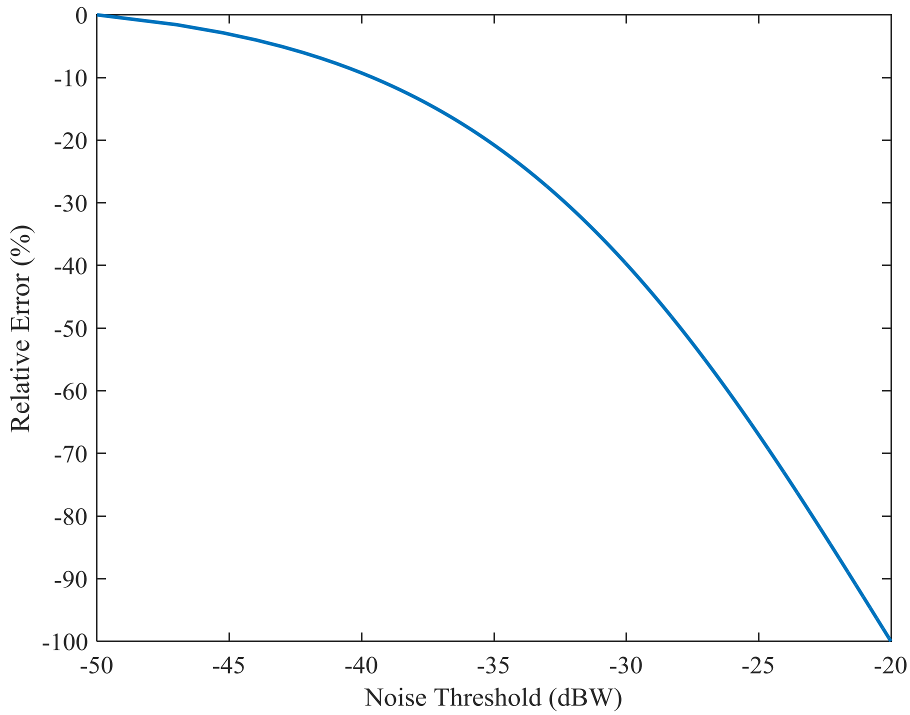

Figure 2-6: Sensitivity of RMS delay spread to selected noise threshold (using analytical formula).

b. Simulation Approach:

The Ricean channel was realized several times with the channel parameters described in previous section. Here, for an example, we used SNR=5 dB and selected three channels with very close delay domain K-factor of 5 dB to present. Figure 2-7 and Figure 2-8 show the general pattern of the relative error in calculated K and RMS delay spread versus selected noise threshold, respectively. In very low noise threshold values, because of presence of noise, the error is high. As the threshold increases, some portion of noise is masked out and in specific threshold the error becomes very small, *i.e.*, close to zero. Increasing the noise threshold above this value causes some of the MPCs to be masked out as well and error increases until all MPCs are masked out by noise threshold. Moreover, they show that the proper noise threshold in which the error is minimum, is not always a fixed value necessarily even for channels having close SNR and K-factor values. This emphasizes getting advantage of frequency domain data instead which is less susceptible to noise for calculating K-factor and, as we will see later, for selecting the proper noise threshold.

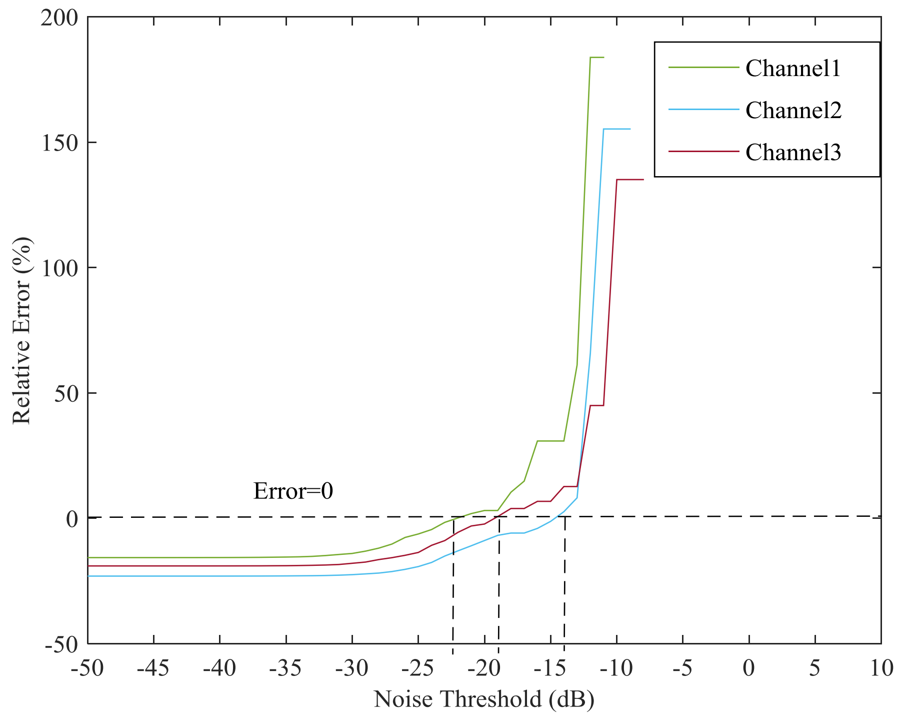

Figure 2-7: Sensitivity of delay domain K-factor to noise threshold (simulation).

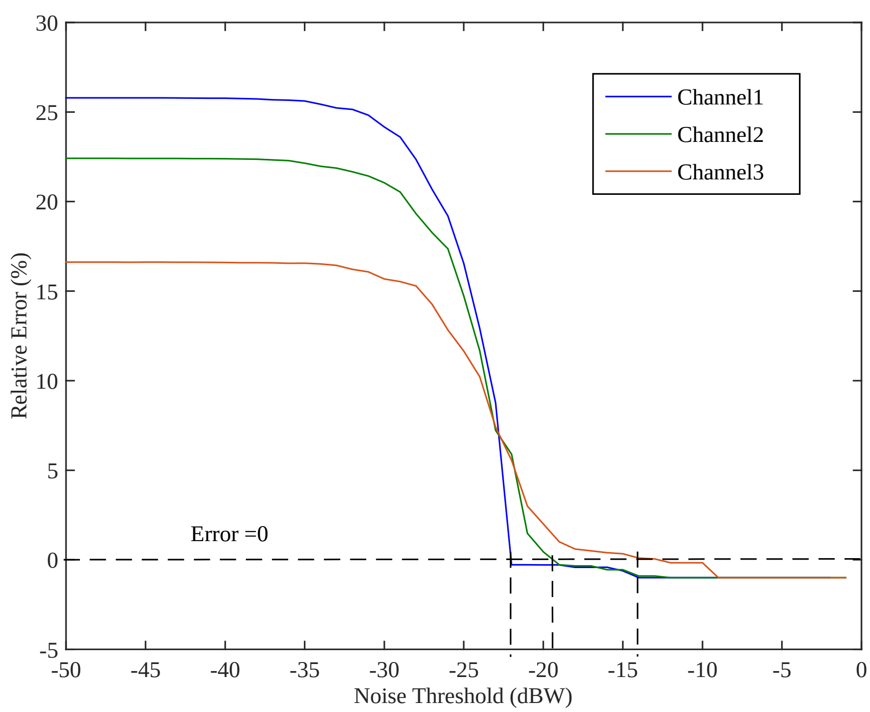

Figure 2-8: Sensitivity of RMS delay spread to noise threshold (simulation).

2.4.3 Impact of Noise on Ricean K-factor Estimation in the Frequency Domain

Unlike the delay domain calculations which accurate estimation of Ricean K-factor depends on the level of applied noise thresholding, in frequency domain due to spread of the noise spectrum over all frequency points with an even impact, calculations will suffer less when SNR decreases. Figure 2-9 shows the result of relative error between calculated K-factors from noisy and corresponding noise-free frequency amplitude responses. The simulations are repeated for SNR values from 5 dB to 30 dB (These values are the practical SNRs values exist in a typical measurement), and for channels generated with K = 5 dB to 35 dB with 2 dB step sizes. The largest and smallest error in the plot corresponds to K = 5 and K = 35 dB, respectively. Figure 2-10 summarizes these curves in a single 3D surface plot for better visualization which x, y and z-axis are SNR, K-factor and the relative error, respectively.

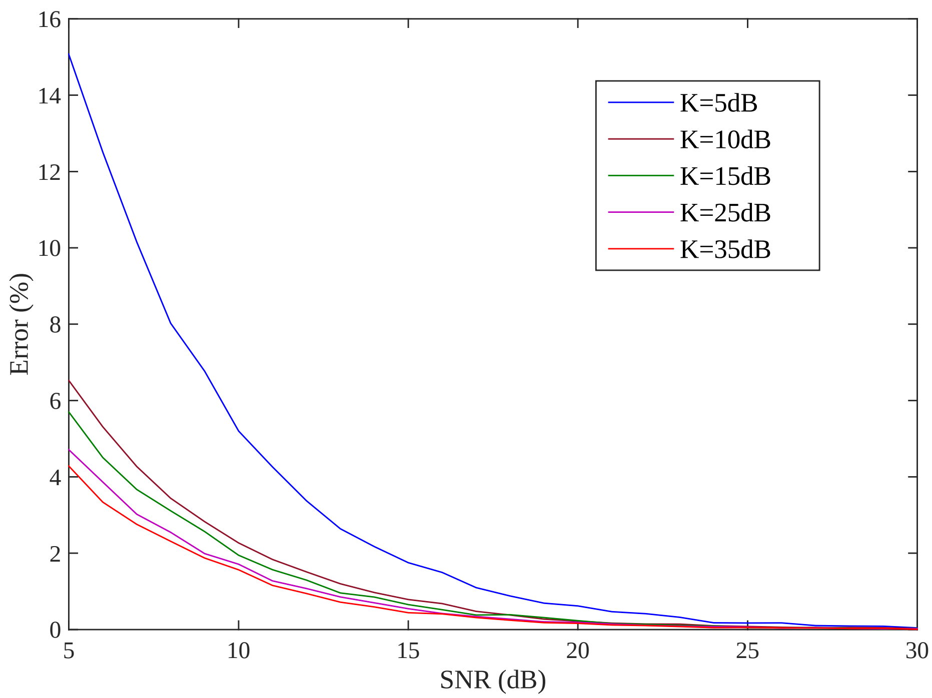

Figure 2-9: Plot of effect of noise on error of frequency domain K-factor estimation.

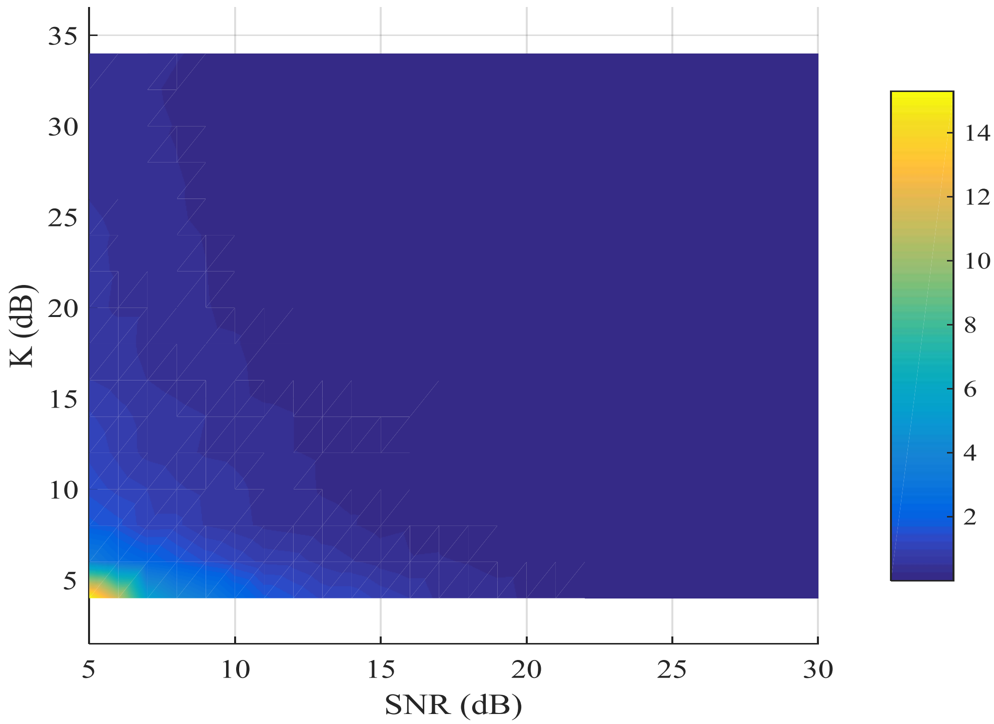

Figure 2-10: The 3D surface colour plot (top view) of the effect of noise on error of frequency domain K-factor estimation.

The results show that even for channels with SNR and K-factor as low as 5 dB the error of Ricean K factor calculated from frequency domain records is small and less than 15%. This shows the merits of calculating K-factor in frequency domain instead of delay domain which we already showed how sensitive it is to the noise threshold. This is the basis for our proposed noise threshold detection algorithm which results are presented in next section.

2.4.4 Performance of a Bisection Algorithm for Estimating the Noise Threshold

In this section, we compare channel K-factor, mean and RMS delay spreads, obtained by our proposed noise threshold selection algorithm with the values obtained by noise threshold suggested in the literatures. Often the noise floor of the measured data has been used and well accepted in past work as noise threshold value [20], [42], [47]. Because of this wide-acceptance, we will use it to compare our method with and show that the error of channel parameter estimation using the proposed algorithm is lower and more consistent. The simulation methodology described in previous section was used here again. Monte Carlo simulations were carried out for 3600 channel realizations with SNR of 5 dB to 35 dB and K-factor of 5 dB to

30 dB. As explained in previous section, K-factor in delay domain from noisy CIR was obtained by varying noise threshold in 1 dB steps. The noise threshold associated with the K-factor which corresponded to less than 10% relative error between that K-factor and the K-factor obtained from scalar frequency response was selected. Noise floor of the noisy CIR was also obtained by averaging the noise at the tail of the CIR.

Figure 2-11 shows an example of using both of the thresholding methods in filtering out the noise on a representative CIR. The yellow strips are the taps of the noise-free CIR realized with K = 10 dB and black dashed lines are after adding noise with SNR=10 dB. The green taps are the ones recovered after using noise floor as noise threshold whereas the red taps are the recovered signal after using the proposed method. It is seen that the proposed method yields better results since the original taps are recovered fully and there is less effect of noise at the recovered signal whereas the noise floor thresholding method yielded more noise unfiltered after thresholding. The simulation was repeated for channels realized with different SNRs and K-factors. The relative error of the mean and RMS delay spread after applying threshold were calculated and averaged within different K-factor bin sizes using both methods and the result is presented in the following.

Figure 2-12 shows the relative errors of K-factors obtained from noisy frequency amplitude response and thresholded noisy CIR for different channel SNR. The smaller the error implies better threshold selection. As expected, the K-factor error always remains below 10% using the proposed method since our algorithm is set to choose the noise threshold when the error is within X% (where X was chosen 10% here). However, the noise floor method reveals larger relative error (specially in low SNRs) for K-factor metrics and similarly for mean and RMS delay spreads as presented in Figure 2-13 and Figure 2-14, respectively. In Figure 2-13 it is seen that the error of mean delay spread with noise floor method is around 4 and 2 times larger in low and high SNR regions, respectively, compared to proposed thresholding method. In Figure 2-14, the error between RMS delay spread using noise floor thresholding is almost 3 times larger than proposed method in low SNR region whereas the difference gets smaller in high SNRs. The results are consistent with [43], [45] in which it was shown different noise thresholding can lead to remarkable differences in RMS delay spread values.

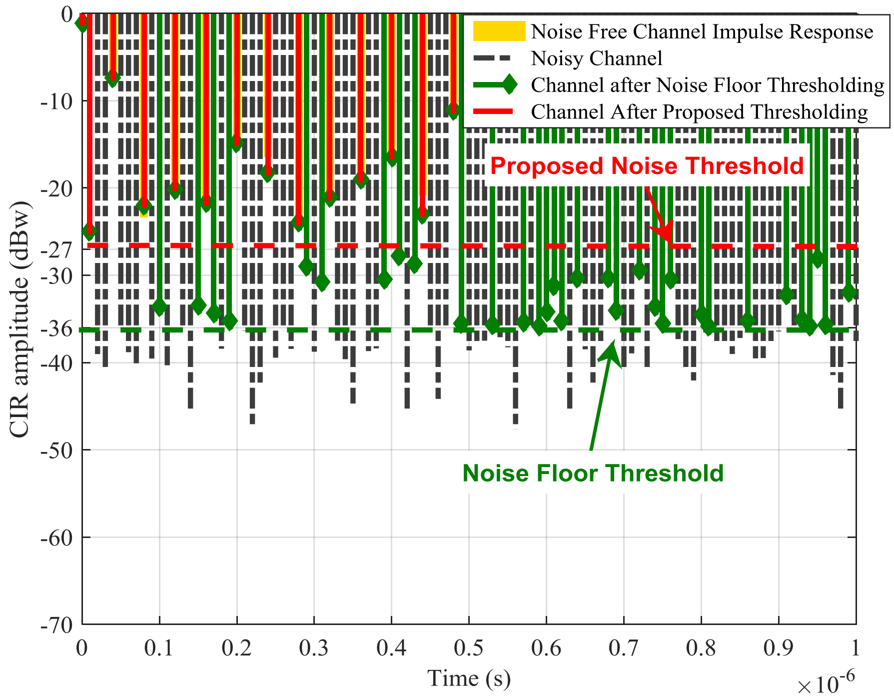

Figure 2-11: An example of noisy CIR: Comparing the effectiveness of the proposed noise thresholding algorithm with the noise floor methods

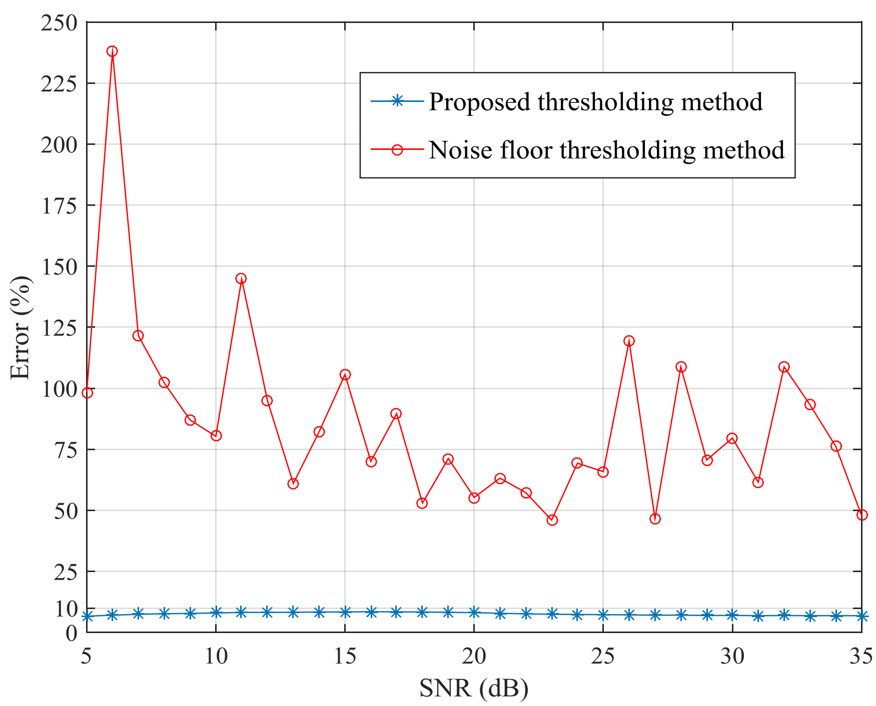

Figure 2-12: Error in estimating K-factor: proposed noise thresholding vs noise floor method.

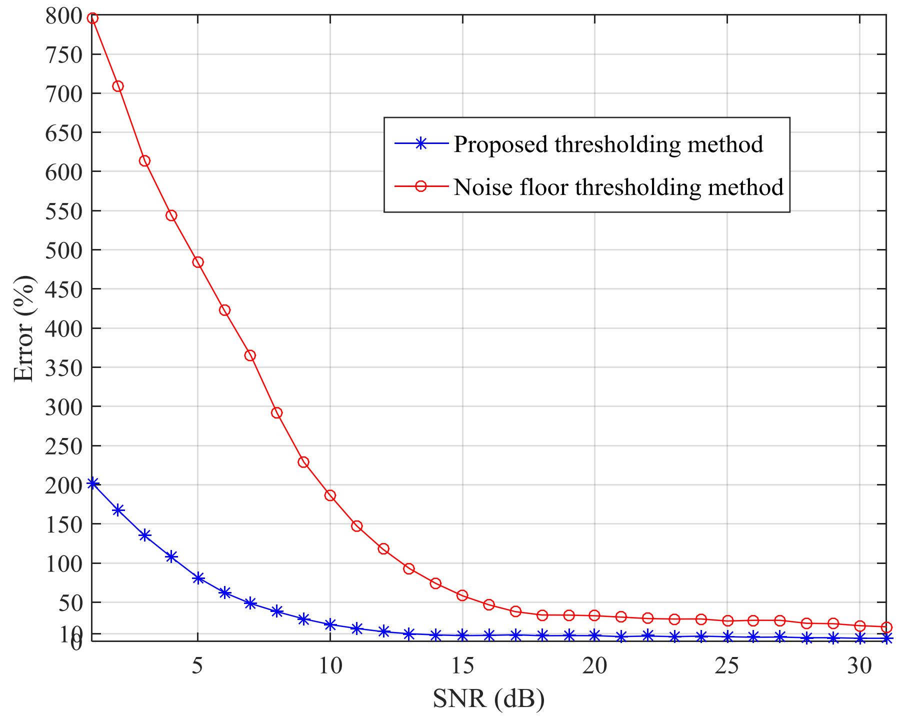

Figure 2-13: Error in estimating mean delay spread: proposed noise thresholding vs noise floor method.

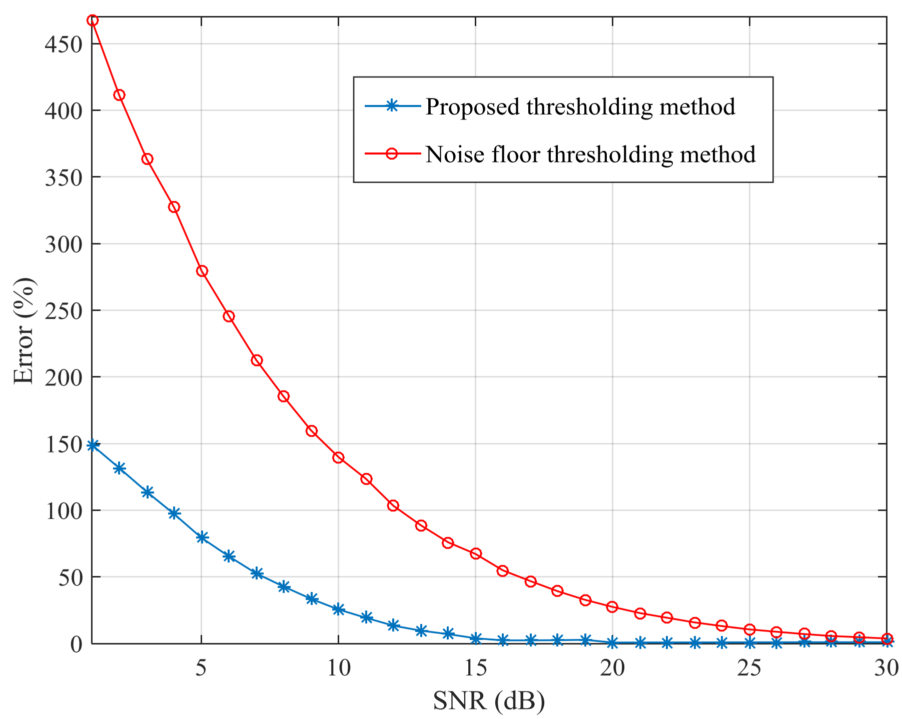

Figure 2-14: Error in estimating RMS delay spread: proposed noise thresholding vs noise floor method.

2.5 Discussion

Previous work has given only limited consideration to the relationship between the Ricean fading distributions observed by sampling in the temporal, space, frequency and delay domains and the effect of noise and sampling on Ricean K-factor estimation in these domains. Moreover, the problem of finding proper noise threshold to separate multipath components and noise from estimated time domain impulse response has been gone under several studies. However, most of the proposed algorithms are based on assumptions that may not be true in the environment which measurement is being done. In order to solve these problems, we:

1. Clarified the relationship between the different Ricean distributions fading observed in different sampling domains. We showed when rapid changes in the relative phase of direct and scattered components occur with shifts in frequency, position of the receiver, or the position of the scatterers over time, regardless of the type of shift, the relative energy in the direct and scattered components is identical so the Ricean K-factor that describes the fading distribution is also identical. This results in the same first-order distribution in the frequency, space and delay domains. So, the Ricean distributions observed in these domains are also equivalent.
2. Revealed the relative impact of noise on K-factor estimation based upon data sampled in these domains. We concluded that estimates of K-factor based upon measurement of the scalar channel frequency responses can be collected more easily and are less susceptible to noise (less than 15% error in the worst channel scenarios which we considered) than those based upon measurements collected in the other domains since noise affects each time domain component individually whereas its spectrum is spread all over the frequency band therefore has less effect. Beside, we showed that choosing a proper noise threshold value will change both K-factor and RMS delay spread significantly and this emphasizes again using frequency domain data to estimate channel parameter such as K-factor.
3. Proposed a bisection algorithm for estimating the noise threshold associated with the estimated channel impulse responses, based upon the equivalence of the Ricean distribution observed in the frequency and delay domains. Having an accurate noise threshold value, other time domain channel parameters such as mean and RMS delay spread can be calculated more accurately. For the simulations we did in this work, using the bisection algorithm, the mean and RMS delay spreads of the thresholded noisy CIR was estimated 3 and 4 times

better, respectively, for channels with low SNRs (*e.g.*, 5 dB) compared to using conventional noise threshold estimation techniques such as using noise floor as the threshold. The performance of the noise floor thresholding technique was getting better in channels with large SNR values (*e.g.*, 35 dB) such that error of calculating the mean delay spread using both methods were small and almost same whereas RMS delay spread using noise floor method had 2 times more error compared to our proposed method.

The results presented in this chapter allow us performing channel measurements to determine the best practice for collecting data within the proper domain. The problem of calculating K-factor by isolating LOS and MPCs from noisy records and uncertainty about existence of LOS component in the data or hyper Rayleigh channel is resolved by obtaining K from scalar frequency response. The results also indicate a better noise threshold detection algorithm. This reliable technique, besides improving the accuracy of the estimated channel parameters such as K-factor and RMS delay spread, can be used for many applications such as on-site channel parameter estimation. The calculations in this chapter were mainly based on realizing the Ricean channel. Further studies are required for comparing the accuracy of the K-factor obtained from other types of channel realization such as hyper Rayleigh fading channel in delay and frequency domains. Moreover, the estimator we used to calculate frequency domain K-factor loses accuracy in channels with small K factor. Development of better estimator with higher accuracy in low K-factors is recommended.

Chapter 3:
Estimation of Channel Impulse Response from Scalar Frequency Response Data using the Hilbert Transform

3.1 Introduction

Knowledge of the Channel Impulse Response (CIR) is an important factor in proper design and implementation of communication networks. CIR can be measured directly, estimated by correlating Pseudorandom Binary Sequences (PRBSs), or obtained by IFFT of Complex Frequency Response (CFR). *E.g.*, IFFT of CFR has been widely exploited due to excellent dynamic range performance. It is generally easier and more cost effective to measure the scalar frequency response rather than the complex response since phase is difficult to measure without a reference and requires VNA-based measurements with highly skilled personnel. In the absence of phase information, the IFFT of CFR will not retain an accurate rendition of the CIR. There has been a large body of studies proposing methods to retrieve the phase out of scalar responses. Use of measurement with intent of reconstructing the original signal with phase retrieval process has been historically used in X-ray crystallography [63] and today it has found an important applications including but not limited to astronomy [64], diffraction imaging [65], optics [66].

Several direct and iterative algorithms have been proposed for the reconstruction of the phase of transfer function from its magnitude [67]. Existing methods for phase retrieval rely on all kinds of a priori information about the signal, such as positivity, atomicity, support constraints, real-valuedness, and so on [67]. Other methods which are proposed to overcome these limitations such as direct methods [68], Oversampling in the Fourier domain [69] (to mitigate the non-uniqueness of the recovered phases), Alternating projection algorithms [70] and Phaselift algorithms [71] are limited in their applicability to small-scale problems due to their large computational complexity and often require careful exploitation of signal constraints and delicate parameter selection to increase the likelihood of convergence to a correct solution.

The Hilbert transform, also known as the Cepstrum technique, is an alternative method for estimating the CIR from the scalar frequency response. The set of conditions under which a sequence is uniquely specified by Hilbert transform from magnitude was developed in [72]. Since then it has gained a large attention mainly because of its simplicity. The idea of estimating the multipath complex frequency response of propagation channel from its amplitude was first proposed in [15] where spectrum analyzers and Hilbert transform was used for UHF 1–2.5 GHz channel characterization and a good agreement was observed between the estimated impulse responses and the VNA measurement data. Since then, this technique has been used for radio channel characterization in different scenarios [73], [74]. The idea was also extended to UWB channel measurements in [75]. Moreover, it has been used for intermittent spike identification for power quality control [76] and powerlines characterization [77]. *E.g.*, in [77] the group delay obtained using Hilbert transform was shown to correspond to the deviation of group delay from a constant on high voltage lines. Although Hilbert transformation removes linear phase component and therefore the absolute delay from CIR, work in [77] showed that nonlinearities in the phase characteristic due to reflection can be determined with Hilbert transform of the amplitude characteristic. Hilbert has also been popular in light-wave technologies for characterizing of experimental fibre Bragg grating from measured reflectivity or for obtaining channel parameters of photonic crystals [78], [79].

Despite a large body of past work on Hilbert transformation, most of them has emphasized the algorithm rather than the domain of the effectiveness of the algorithm. Some past works have shown that under certain circumstances Hilbert transform can be used to estimate a close approximation to the actual phase response and allow a close replica of the CIR to be recovered if the channel is minimum phase, *i.e.*, stable and causal which requires all the poles and zeros of the transfer function to be inside the unit circle [15], [72]. Moreover, it is well known that the performance of the Hilbert transform approach degrades significantly as the strength of dominant or fixed component in the CIR degrades or equivalently as the Ricean K-factor decreases. However, no rigorous mean for determining whether the given frequency scalar response is suitable for processing using Hilbert transform has been previously disclosed.

In few studies such as [80], [81] authors have developed minimum phase criteria based on power delay profile, *i.e.*, tap's amplitude and power. However, as we will explain in next section, these conditions require knowledge of the delay domain CIR that is unknown prior to measurement. In summary, despite the frequent use of Hilbert technique, many of the steps required to fully exploit this technique have not been previously revealed and previous studies are lacking to provide a physically meaningful guidance in determining applicability criteria of this technique for phase recovery of propagation channels. So, in this chapter, we will develop a *test*, based on Ricean K-factor obtained from frequency scalar response to quantify the estimation error of Hilbert transform on different metrics of the channel.

In the rest of this chapter, we will describe the theory of minimum phase channels and the criteria previously mentioned to satisfy this condition. We will show the relationship between the K-factor and Hilbert estimation error can provide a benchmark for determining whether a given frequency scalar response is suitable for Hilbert transform processing. Then we will explain our methodology for the MATLAB simulations and the way we developed the test. We will represent the quantified error of Hilbert estimation results for the selected metrics for channels with different K-factors and obtain the K-factor threshold corresponding to an acceptable error percentage. Then we will show the amount of increase of this error under different channel SNR values. We will conclude this chapter in the last section along with recommended future works.

3.2 Concept

In general for a propagation channel measurements, the meaning of minimum phase is unclear [74], [82]. Depending on the environment type, frequency band, and relative position of the antennas the channel can behave as minimum phase unpredictably, *i.e.*, no condition of the radio channel is known a priori to allows one to state if the measurements will or will not be of minimum phase [75]. A linear, time-invariant system is said to be minimum-phase if the system and its inverse are causal and stable which requires all the poles and zeros of transfer function to be inside unit circle, A mathematical representation of general channel function in complex frequency domain, *z*-domain, can be written as [82]

$$h(z) = Az^{n_0} \frac{\prod_{k=1}^{M_i}(1-a_k z^{-1}) \prod_{k=1}^{M_o}(1-b_k z^{-1})}{\prod_{k=1}^{P_i}(1-c_k z^{-1}) \prod_{k=1}^{P_o}(1-d_k z^{-1})} \ , \tag{3.1}$$

where A is the scale factor and z^{n0} is the linear phase factor. M_i and P_i are the number of zeros and poles inside the unit circle, respectively and M_o and P_o are zeros and poles outside of this circle. It has been proven that for $h(z)$ to satisfy the minimum phase channel condition, there should be no linear phase component (n_0=0) and $h(z)$ should be causal which forces $h(z)$ to be in the form of

$$h(z) = A \frac{\prod_{k=1}^{M_i} (1 - a_k z^{-1})}{\prod_{k=1}^{P_i} (1 - c_k z^{-1})} \ . \qquad (3.2)$$

This highlights the limitation of using Hilbert in retrieving the linear phase component which is traditionally has been used to obtain the propagation absolute delay. This is mainly because this information is not captured by the magnitude measurement. Therefore, the minimum phase channel will always have the minimum group delay [83] and it can be found by differentiating the phase [82]. Moreover, it has been shown that for a minimum phase function with N distinct zeros, there will be $2^N\text{-}1$ other distinct transfer function with identical magnitudes, all with same energy because of Parseval's theorem. The effect of replacing a zero inside the unit circle with an outside one is in fact replacing *e.g.*, z_0 with $1/z_0$ and is shown to increase the phase delay of the estimated channel and spreads the CIR energy over the delay domain without altering the amplitude response [15]. Although these effects are very well explained using mathematical formulations, it is not physically meaningful for an operator who captures the frequency amplitude response in real-world measurements. As a result, instead of relating the minimum phase condition to the location of zeros and poles of complex transfer function, people have mentioned the criteria based on CIR properties, *e.g.*, in [80], [81] as explained in the following.

The Hilbert transform is a linear operation which generates the phase information using [15]

$$\arg(H(j\omega)) = \psi[\log|H(j\omega)|] \ , \qquad (3.3)$$

where ψ is Hilbert operation and *arg(.)* refers to the phase component of the complex frequency response, $H(j\omega)$, and ω is the angular frequency. In previous work, people have selected different error metrics for comparing the Hilbert estimated signal and the original one. Error between CIRs (after and before Hilbert) or PDPs [72], [84], correlation between imaginary parts of the CFRs [15], Null hypothesis tests, *e.g.*, student’s t-test for similarity of the energies of the signals in time domain [15] and RMS delay spreads [14], [75] are among those metrics. Although depends on the sensitivity of the application for which Hilbert is used to estimate the response, different error metrics can be considered to develop the test delay spread has been used more frequently than other metrics and is considered as an important decision making criteria for design of many networks. Since the mean and RMS delay spreads are the first and second moments of delay spread, respectively, and therefore natural statistics to consider, in our work we will use them as the error metric beside the K-factor parameter.

Cassioli in [80] gave a sufficient condition that, if met, insures that a channel impulse response is of minimum phase and Hilbert can be applied. This condition sets a lower bound to the power of the first path that should be larger than the power spectral density of the sum of all the subsequent paths, *i.e.*,

$$|a_0|^2 > \left|\sum_{i=1}^{N_p} a_i e^{j\omega\tau_i}\right|^2 \quad , \tag{3.4}$$

where a_0 is the amplitude of the LOS component and a_i is the amplitude of i's multipath component and N_P is the total number of multipath components with arrival times of τ_i. This result is more general than the results obtained by Morgan in [81] since the condition in (3.4) may identify minimum-phase systems that [81] cannot recognize where it was stated that a channel is minimum phase if

$$|a_0| > \sum_{i=1}^{N_p} |a_i| \, . \tag{3.5}$$

In both of the criteria mentioned above the Hilbert applicability is based on the delay domain channel parameters that are unknown to the operator who is doing the frequency domain scalar measurement. Beside, in none of these papers, quantified study of estimation error versus channel parameters is carried on. Therefore, there is a need for developing a physically meaningful and easy to use criterion in order to test if Hilbert can be applied on a scalar frequency response of a channel.

In order to create a benchmark to devise the test that we are after, we start with channel properties which affect the Hilbert error directly. It is well understood that in the channels with large K-factor, phase distribution of frequency response decreases such that for LOS channel, phase plot versus frequency is flat. Figure 3-1 shows this relationship graphically.

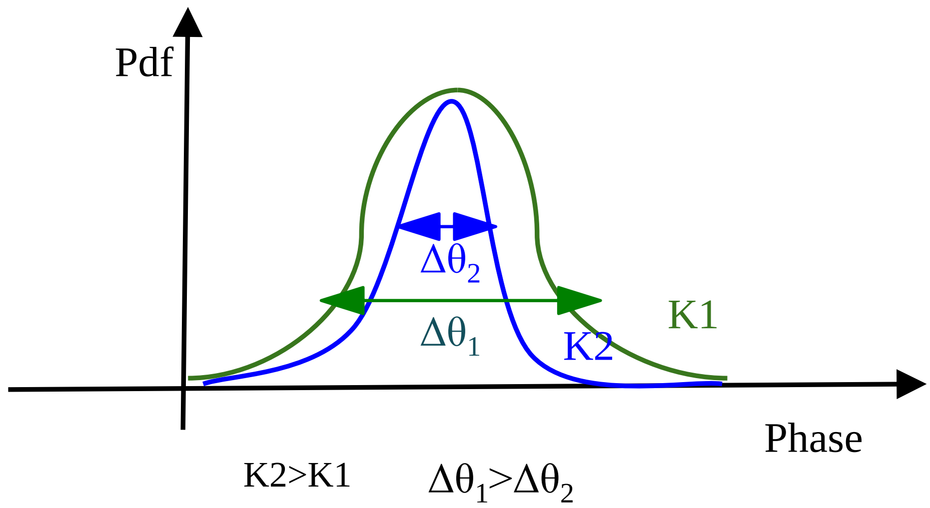

Figure 3-1: Comparison between phase distribution of channels with different K factors.

As explained before, Hilbert will estimate a unique channel correspond to minimum phase version of the channel which measurement is collected in and depends on how wide the phase dispersion is, applying Hilbert transform to estimate phase will result in different amount of error which is proportion to the channel phase distribution, *i.e.*,

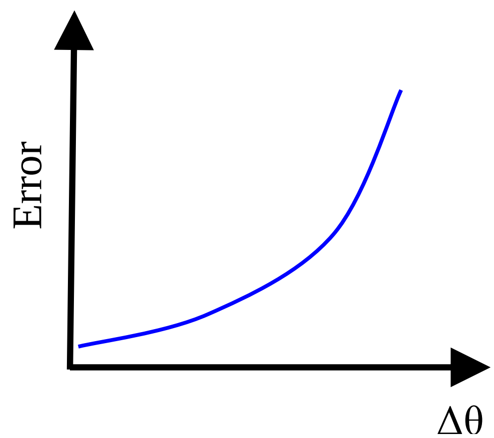

Figure 3-2: Approximate relation between Hilbert estimation error and channel phase dispersion.

However, there is usually no information on channel phase dispersion unless performing the complex response measurement. So it cannot serve as a good benchmark for the application we are after. However, it is well known that the complex fading channel gain can be modeled as a Gaussian random variable according to the central limit theorem. When there is a line-of-sight (LOS) component in the channel, the joint probability density function (PDF) of the fading envelope and the fading phase is given by [10]

$$f_{R,\Theta}(r,\theta)=\frac{r}{2\pi\sigma^2}\exp\{-\frac{r^2+A^2-2rA\cos(\theta-\theta_0)}{2\sigma}\}\ , \tag{3.6}$$

where r and θ are fading envelope and phase, respectively. A^2 is mean power of LOS component and $2\boldsymbol{\sigma}^2$is the mean power of scattering components. By integrating it over the envelope, the fading phase PDF is obtained as [10]

$$f_{\Theta}(\theta)=\frac{e^{-K}}{2\pi}+\frac{\sqrt{K}\cos(\theta-\theta_0)}{2\sqrt{\pi}}e^{-K\sin(\theta-\theta_0)}\cdot erfc(-\sqrt{K}\cos(\theta-\theta_0))\ . \tag{3.7}$$

Although this shows that phase dispersion and Ricean K-factor are related and K-factor can be related to the error of Hilbert estimation, there is no information on delay domain K-factor when doing the scalar frequency measurement and therefore K-factor obtained from delay domain data cannot be a good benchmark. However, as we explained in previous chapter, Ricean K-factor obtained from delay domain CIR and frequency domain response are equivalent. So, frequency domain Ricean K-factor can be a good representation of channel phase dispersion, therefore a good benchmark and criteria to set condition (rule) of applicability for Hilbert transform based on acceptable amount of error of estimation. In the following section we will explain the simulation methodology in order to develop the guidelines of applying Hilbert to retrieve phase with specific error values.

3.3 Implementation

In this chapter, the Ricean channel, same as the method described in previous chapter, is realized using *ricianchan* function in MATLAB. The input parameter of the function is set similar to the previous chapter. This includes the average power of the MPCs which is considered 12 MPCs, exponentially decaying with fixed time of arrival, channel BW of 25MH is assumed and K-factor and channel SNR ranges of [-10 dB, 40 dB] and [5 dB, 40 dB] are considered, respectively.

Upon generation of the channels, the channel parameter such as K-factor, mean and RMS delay spreads are calculated in delay domain. Fourier technique is used to obtain complex frequency responses. Phase information is then dropped and the magnitude data is used to estimate the phase of channel using Hilbert function of MATLAB. Estimated CIR is then calculated using inverse Fourier and its delay domain parameters are obtained using the estimated response. The Monte-Carlo simulation is repeated for 3600 channel realizations. By comparing the estimated and original parameters, the relative error is obtained and plotted versus channel K-factor for each of the selected error metrics. As explained before, we are using the estimation error of delay spreads based on frequency domain K-factor as the benchmark. Figure 3-3 summarizes these steps. In addition, we will study the effects of noise on the developed benchmark. For this purpose the *awgn* function of MATLAB is used to add white Gaussian noise with specified SNR values to the delay responses. Then the comparison between original and estimated channel parameters is made on parameters of CIR of noisy channel before and after Hilbert transform for the channels with K-factor close to the benchmarked K-factor. The same methods described in Chapter 2 are used to calculate RMS delay spread and K factors in delay and frequency domains.

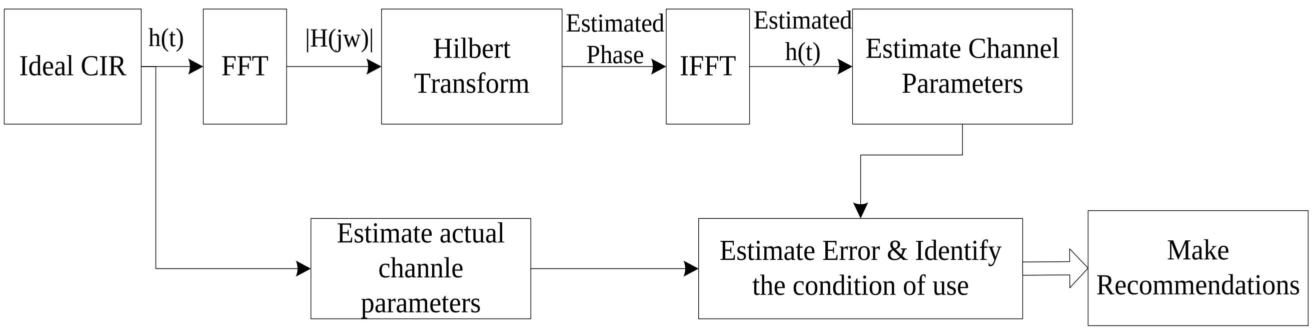

Figure 3-3: Flowchart of simulation steps for developing Hilbert transform applicability criteria.

3.4 Results

3.4.1 Effect of the Hilbert Transform on Ricean K-factor Estimation

Here we plot the scatter plot of K-factor obtained directly using original CIR and the one estimated after applying Hilbert transformation. It is observed that Hilbert is not changing the channel K-factor when it is applied for a channel with strong LOS component, *i.e.*, large K factor. However, Hilbert overestimates it for the channels with small K-factors (K<5 dB). This is mainly because of altering the LOS and MPC's amplitudes and locations on the delay axis in the estimated CIR compared to original CIR. This causes other parameter of channel such as RMS delay spread also be altered in some channels which are not minimum phase, *i.e.*, in channels with small K-factor. So in the following section we will obtain the plots for error due to Hilbert transform on channel parameter estimation and will specify the threshold which the error is acceptable. This paves the way to develop the *test* for examining whether or not Hilbert is applicable for a channel with known scalar frequency response.

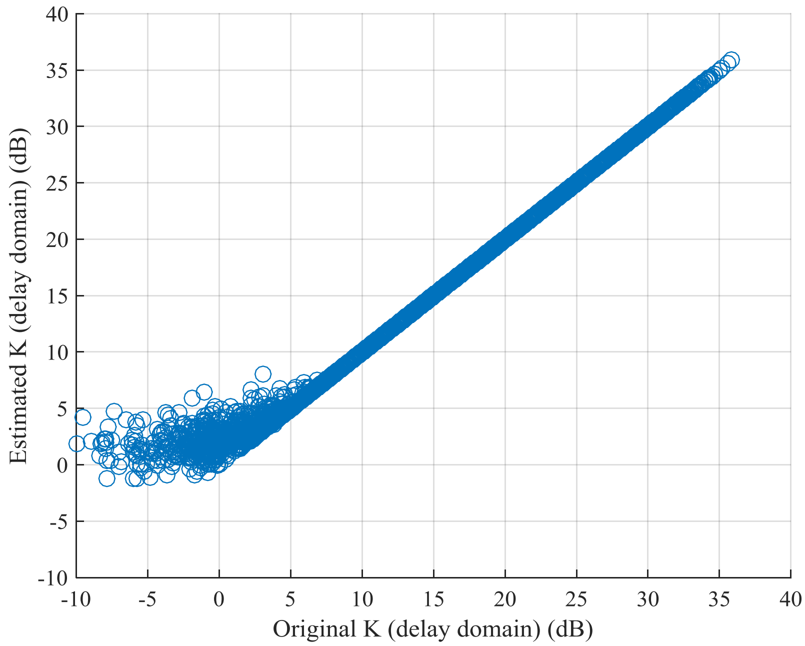

Figure 3-4: Effect of Hilbert transform on delay domain K-factor estimation.

3.4.2 Effect of the Hilbert Transform on Selected Error Metrics

In this section, we present the quantified results for the estimation error of selected metrics due to use of Hilbert transform to estimate phase of channels realized with different K-factors. The error metrics as discussed previously, are chosen as *Ricean K-factor*, *Mean of delay spread* and *RMS delay spread*. The 10% error for each of these metrics is assumed as an acceptable error and frequency domain K-factor is considered as the benchmark to develop our test based on. All the realizations are considered noise-free and the only error is caused just by the Hilbert transform.

The results are presented in Figure 3-5- Figure 3-10 and show that all of the selected error metrics are showing error of less than 10% when Ricean K-factor is above 8 dB. This value of K-factor guarantees that for a channel with higher K-factor, the error value for estimating any of the selected metrics using Hilbert will be below 10%. The figures include also the histogram and boxplot of the errors around the obtained threshold K-factor (with 2 dB bin size, *i.e.*, for 7 dB < K < 9 dB) presented after each error metrics plot. The box plots specify the mean and standard deviation of the errors for the channels with K-factor around 8 dB. Since this section concerned noise-free analysis, in next section we will study the effect of channel SNR on the mean of the error values for each error metrics specified in the box plots. This will give insights on the amount of expected increase of mean errors generated by Hilbert for a channel with specific SNR compared to the noise-free scenario. Note that in the following plots, by "Error" we mean the relative error that is the difference of the calculated metric after and before applying Hilbert over the metric's value before applying Hilbert, i.e., $error = (x_{before} - x_{after}) / x_{before}$ where x is the parameter of the interest.

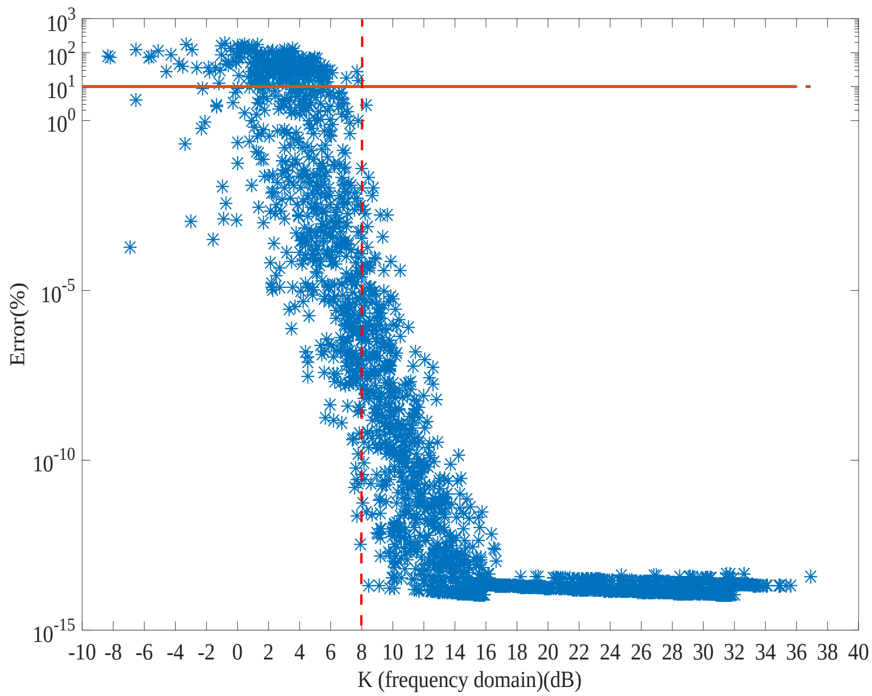

Figure 3-5: Error of delay domain K-factor estimation due to Hilbert transform for a selected threshold of 10%.

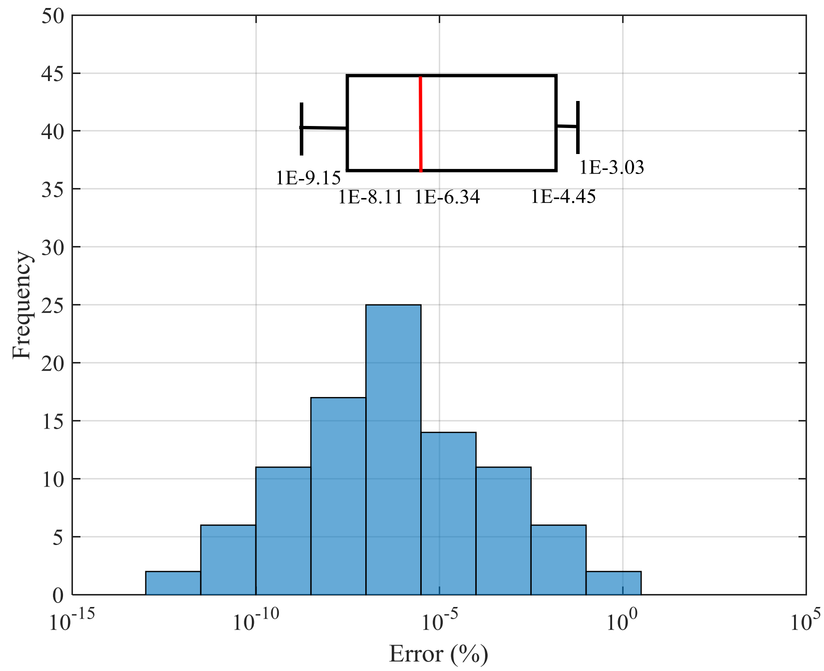

Figure 3-6: Distribution of the Hilbert estimation error of K-factor within the bin of K = 7-9 dB.

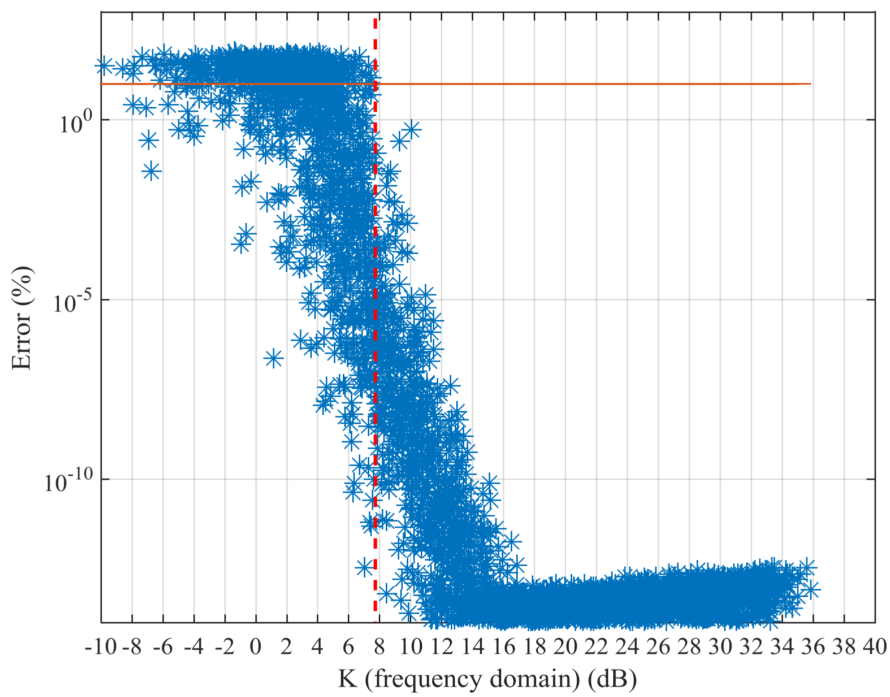

Figure 3-7: Error of mean delay spread estimation due to Hilbert transform and selected threshold of 10%.

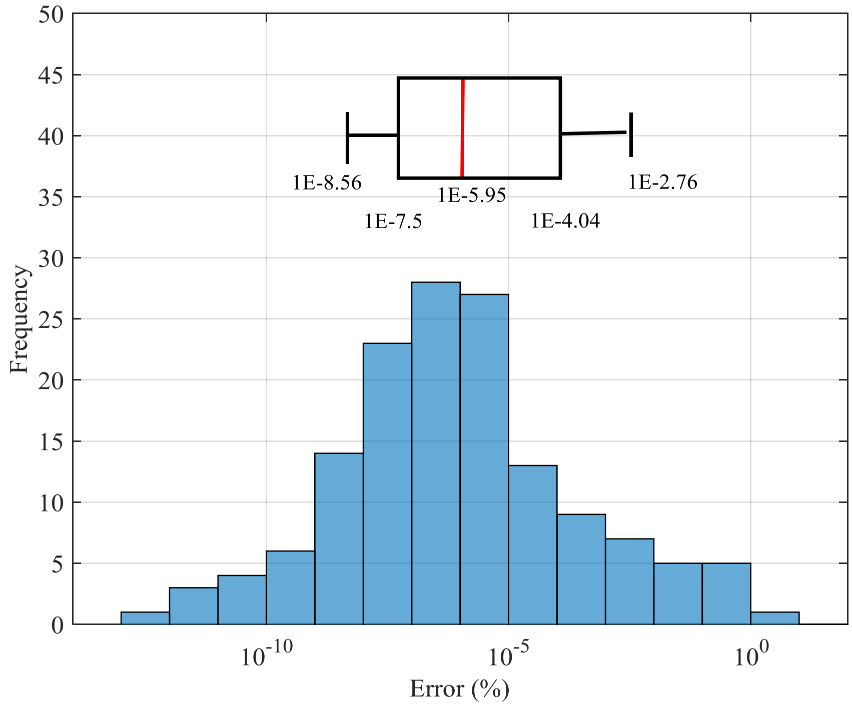

Figure 3-8: Distribution of the Hilbert estimation error of mean delay spread within the bin of K = 7-9 dB.

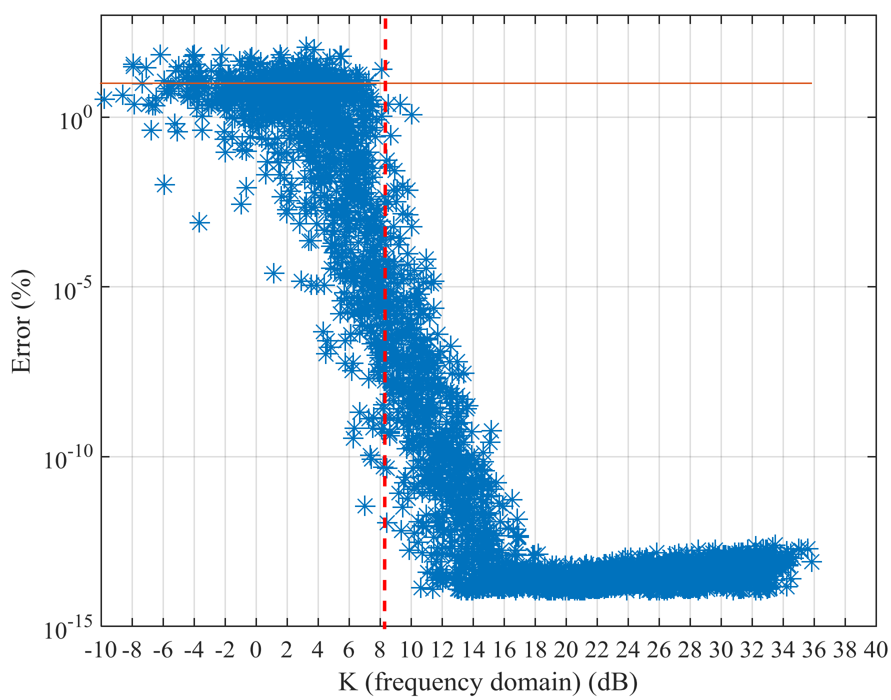

Figure 3-9: Error of RMS delay spread estimation due to Hilbert transform and selected threshold of 10%.

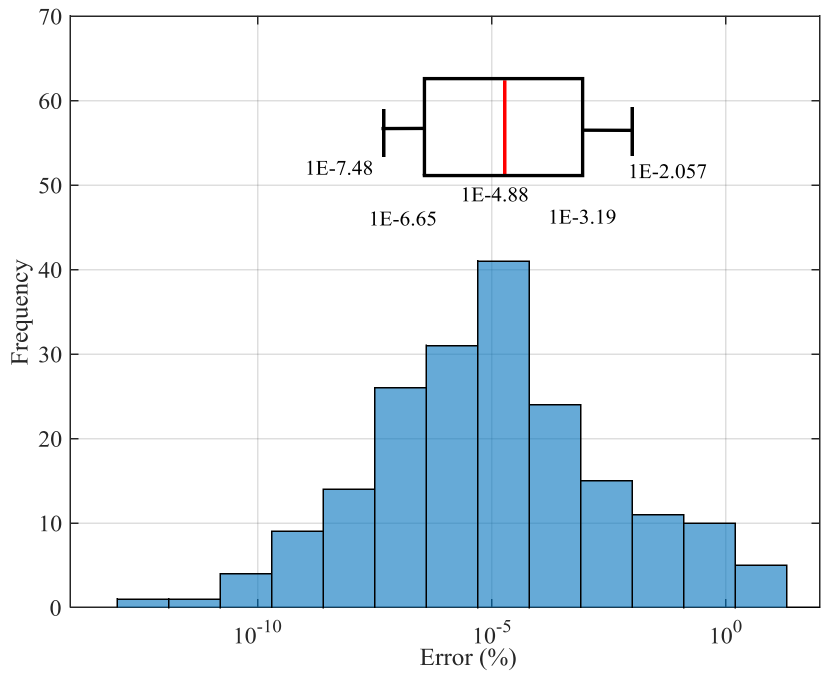

Figure 3-10: Distribution of the Hilbert estimation error of RMS delay spread within the bin of K = 7-9 dB.

3.4.3 Effect of Noise on the Proposed Applicability Threshold

Random noise on the magnitude data will translate into noise in the phase data calculated by the Hilbert transform. In this section, we realized Ricean channels including AWGN noise with specific SNR values at each round. Then, we calculated the amount of increase in error due to the presence of noise at the threshold K-factor value which we obtained in previous section for noise-free scenario. We chose SNR=5 dB, 10 dB, 15 dB, 25 dB, 30 dB and 40 dB in our study to cover both low and high SNR ranges and the noise was added to the channel impulse responses. Then, Hilbert transform errors on the selected metrics were calculated using noisy original CIR and noisy estimated one. The noise thresholding method introduced in Chapter 2 was implemented and used to calculate delay domain channel parameters. We selected a 2 dB bin size (7 dB$<K<$9 dB) to produce the box plots. Figure 3-11 - Figure 3-13 show the amount of error one should expect in channels with K = 8 dB (noise-free benchmarked K-factor) in different SNRs. They moreover, imply that the mean of estimation errors under that specific channel SNR will always be smaller than the values showed with the red lines in each box plot if K-factor becomes larger than 8 dB. As it is seen, the maximum of the errors for each of the metrics approaches to 10% (*i.e.*, benchmarked error threshold we obtained under noise-free analysis) in very large SNR values.

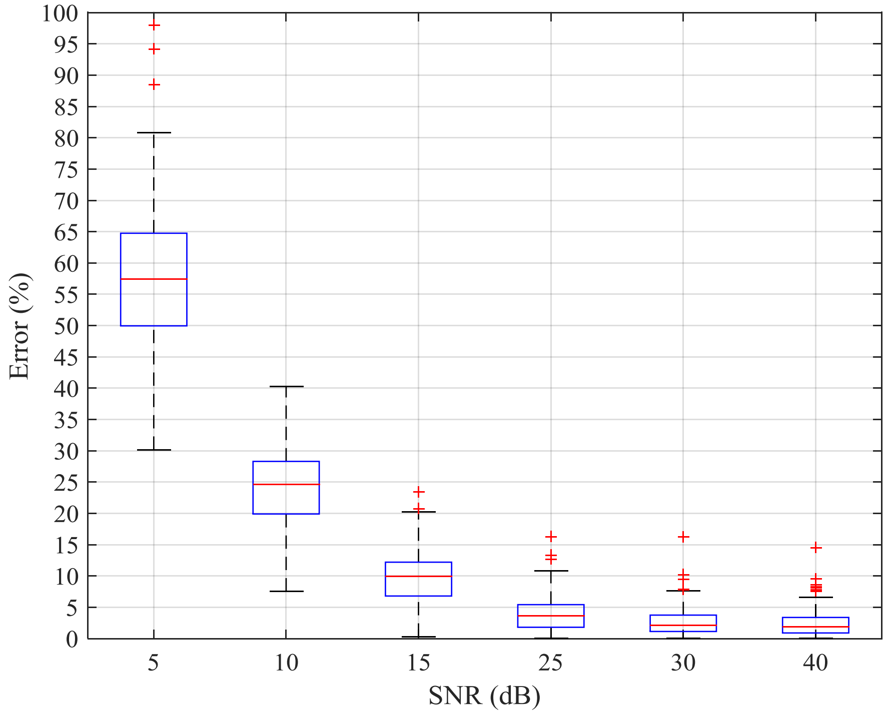

Figure 3-11: Relative error of K-factor versus SNR, calculated before and after Hilbert for channels realized with K-factor between 7 dB<K<9 dB.

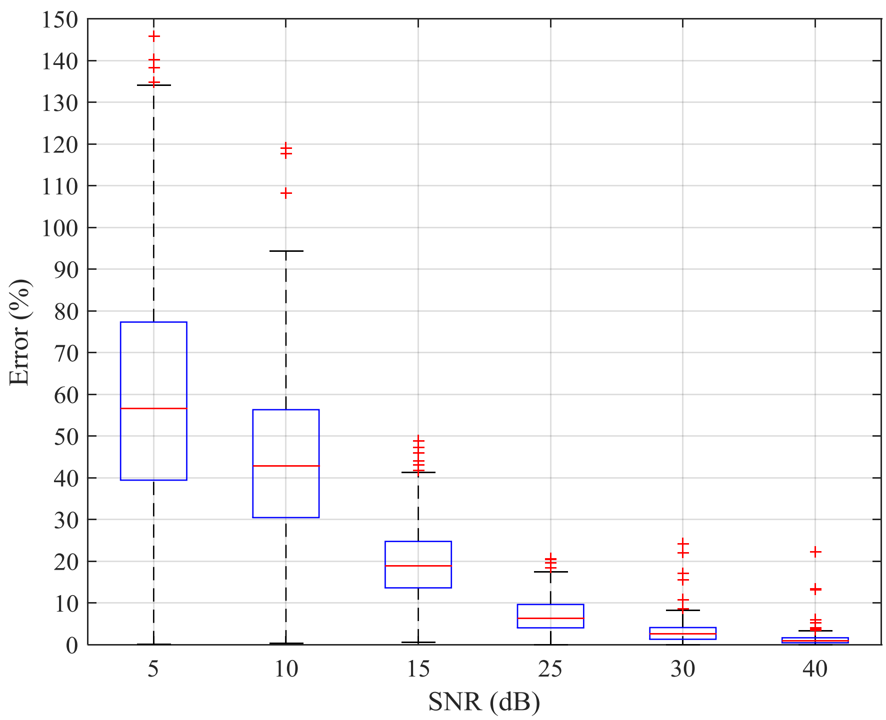

Figure 3-12: Relative error of Mean delay spread versus SNR, calculated before and after Hilbert for channels realized with K-factor between 7 dB<K<9 dB.

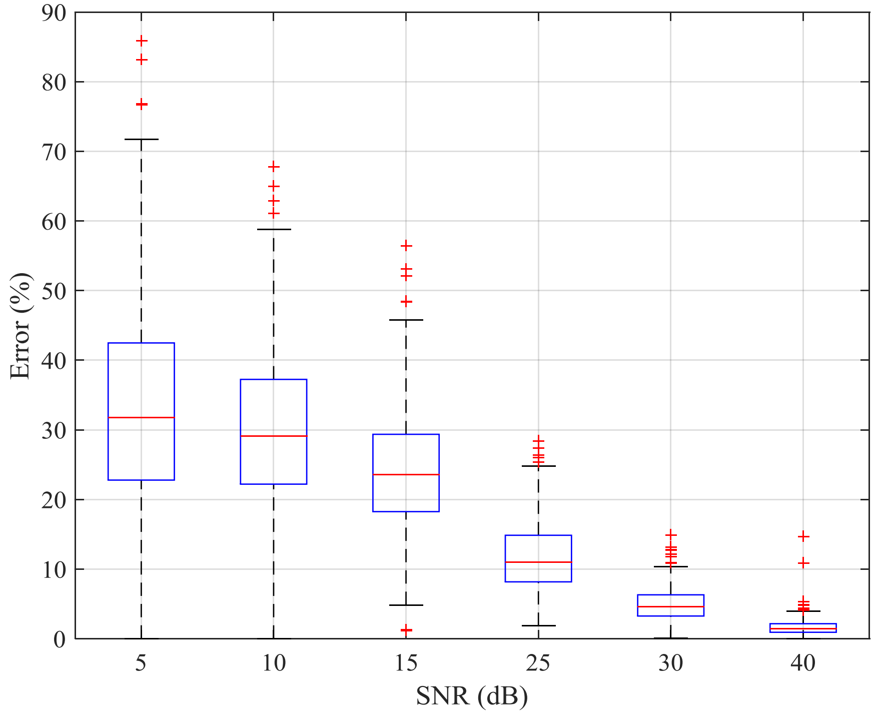

Figure 3-13: Relative error of RMS delay spread versus SNR calculated before and after Hilbert for channels realized with K-factor between 7 dB<K<9 dB.

3.5 Discussion

Using Hilbert transform to estimate the phase is not a new concept but not as well understood as one might expect. Although it is well known that one can estimate the channel impulse response from scalar frequency response data with sufficiently high Ricean K-factor using the Hilbert transform, many of the steps required to fully exploit this technique have not been previously revealed. Previous studies have mentioned "causality" as minimum phase criteria and the condition of applicability for using Hilbert. However, this is not physically meaningful and might not be easily applicable to the real world measurements in where the only available information is frequency scalar data.

To solve these problems, we used the relationship between the Ricean K-factor associated with the scalar frequency response and the error in the estimated channel impulse response as a useful benchmark to develop a test for determining whether a given scalar frequency response is suitable for processing with Hilbert transform. According to the results, Hilbert technique will result in an acceptable error, *e.g.*, less than 10%, in estimating the mean and RMS delay spread when channel Ricean K-factor is larger than 8 dB. It was shown that under noisy channel, the benchmarked K-factor for having maximum 10% error will be larger than the noise-free scenario such that more than 10% error should be expected at channels with K = 8 dB. The relative error behavior of Hilbert estimation under several practical channel SNR values was obtained for any of the selected error metrics. The results are useful when performing scalar frequency response measurements in a channel with known SNR in order to adjust the expectations on estimated error of the extracted channel parameters if Hilbert is going to be used for estimating the phase.

In this chapter, we obtained the amount of increase in relative error of Hilbert on estimating channel K-factor, mean and RMS delay spreads under different channel SNRs. However, this increase was studied just under noise-free benchmarked K-factor, *i.e.*, around K = 8 dB. This evaluation can be extended to the channels with other K-factors to generate a comprehensive estimation error behavior of Hilbert in K-SNR plane. Moreover, other error metrics such as error of CIR amplitudes or phases correlation can also be studies similar to what we did in this chapter. The Ricean channel with fixed time of arrival and exponentially decaying PDP shape was considered in this study. However, further studies are recommended considering LTV channels or when Hyper Rayleigh condition exists to develop a proper Hilbert applicability criteria which generates the acceptable error.

Chapter 4:
Performance of Loosely Synchronous Codes in the Presence of Thermal and Quantization Noise Within Low-SNR Channels

4.1 Introduction

Pseudorandom sequences are the heart of stepping correlator channel sounders. In NLOS environment, the minimum multipath peak that these channel sounders can capture is an important characteristic of them and is referred as dynamic range. It mainly depends on the type of sounding sequences and sampling speed of the equipment used. It is questionable what dynamic range is required when measuring channel's statistical parameters. The multipath components that have very small amplitude may barely have effect on telecommunication systems. However, having larger dynamic range will be advantageous for developing deterministic models for the propagation channel. Beside, high-resolution algorithms that are being used to improve delay resolution of impulse response presume high SNR. This emphasizes the importance of developing an insight on effects of noise on dynamic range of the sequences being used for channel sounding. So, in this section, we will briefly review frequently used sequences in different types of stepping correlator MIMO channel sounders, focusing on orthogonal sequences specifically Loosely Synchronized (LS) sequences. Then we will review previous works in which LS codes were used for channel sounding application and we will highlight the existing gaps in the literature which we try to address in our work.

4.1.1 Traditional Sequences

Parallel measurement of MIMO polarization channel responses using Stepping correlator channel sounders achieve orthogonal transmission between transmitted signals with time shifted (TDM) [85], frequency shifted sequences (FDM) [86] for each polarization antenna, or code division multiplexing (CDM) [87] in which orthogonal or semi-orthogonal sequences are transmitted simultaneously. There are several previous works studying on properties of sequences applicable for TDM and FDM channel sounding. A comprehensive review of existing sequences for this purpose can be found in [88]. The most well-accepted sequences used for channel sounding applications are Pseudo-noise (PN) sequence family which are considered as periodic sequences with random-like behavior and generated deterministically with properties similar to AWGN [89]. M-sequence [90], Kasami [91], [92] and Gold [93] are among the most studied ones. These sequences have been applied in practical channel sounders for many years and are well studied in the literature including their design equations, correlation performance and effects of thermal noise on their dynamic range [94]. In practice, these sequences are mainly designed to generate the largest family sizes, *e.g.*, when used for CDMA networks, and the main performance metrics has been their Auto-Correlation (AC) gain [95]. Any of these binary sequences can be generalized to the multilevel alphabets [96], [97] for better AC performance. However, these non-uniform sequences are more difficult to be implemented in practical channel sounders because of the requirement of highly linear power amplifiers.

4.1.2 Loosely Synchronous Codes

In CDM MIMO channel sounding however, the sequences that are sent simultaneously should be orthogonal not to interfere with each other. The ideal sequence should have Kronecker delta for AC and the cross correlation (CC) equal to zero for any time shift τ. Unfortunately, such ideal sequences do not exist due to bounds on the correlation values of these sequences [23], [98]–[100]. So, when inter-symbol interference is mitigated using a sequence with good AC, the multiple access interference will increase due to increase in CC. In recent years, the interest for partially ideal sequences has boosted. These sequences are the special class of sequences designed to have ideal correlation performance not in all the time shifts but in the vicinity of time shift $\tau=0$ called Interference Free Window (IFW). These sequences are called Zero Correlation Zone (ZCZ) and includes a large number of algorithms generate families of binary and ternary (also known as T-ZCZ) [101]–[105] and found several applications in CDMA networks.

Loosely synchronized (LS) sequences are a family of ZCZ sequences which have been successfully used in quasi-synchronous CDMA application to reduce multiple-access and inter-symbol interferences [106]. Recently LS sequences have been successfully used in MIMO channel sounding applications as well [16], [24], [87], [107], [108]. In [108], a BPSK transmitter was designed and tested for MIMO channel sounding using LS sequences and its performance was evaluated and confirmed in MATLAB. Authors in [24] examined three candidate sequences for MIMO channel sounding including LS, Kasami and chaotic sequences. They concluded that LS sequence is more preferred than Kasami and Chaotic since the channel parameters were measured more accurately using LS in a 2x4 MIMO channel sounder. In [107] a performance comparison study was done between a MIMO 2×2 channel sounder in time domain measurement using LS sequences and VNA based frequency domain measurement. It was concluded that the time domain measurement using LS sequence was faster in recording channel data but had longer post processing. Similar works has proven the advantages of using LS codes for channel sounding.

4.1.3 Noise Effects

There are few works if any on studying effects of thermal noise (channel SNR) on performance degradation of LS sequences since most of previous studies assumed noise free environment. The importance of this issue was previously raised by some authors [109]. Previous works on LS sequence has been mostly focused on design optimization to generate larger family sizes without compromising IFW length, called generalized loosely synchronized sequences [110], or performance evaluation when used in CDMA networks in where the network BER is considered as main performance metrics [111]. Effects of propagation channel and instrument imperfections, *i.e.*, finite SNR and receiver's quantizer resolution on noise level of the correlator channel sounder has been observed in few previous measurements with no support by simulation [112]–[115]. For example in [112], a bench top measurement setup was used to compare measured noise level increase of the channel sounder once when a PN and once when a ZCZ sequence was used. It was concluded that PN noise level increase is much larger than ZCZ therefore ZCZ sequences provided a larger dynamic range in the noisy channel. Because of previous work shortcoming in predicting correlation dynamic range when LS sequences are applied in a practical channel sounder used to sound a channel with finite SNR value, in this chapter we will study the effect of channel thermal noise on dynamic range degradation of these sequences. Not only the thermal noise but also the quantization noise can degrade the dynamic range of these codes as described in following.

In some previous work, the maximum theoretical dynamic range of estimated power delay profile was not achieved which resulted in poor dynamic range. Although use of the equalization after matched filtering could help to decrease the self-noise, it was shown to only be optimal for back-to-back connection of transmitter and receiver which equalization response can be calculated. For example in [115] by use of equalization they achieved a measured dynamic range of 42 dB (47 dB theoretical). The authors concluded that the cause of the self-noise was mostly due to the system linear distortions and accuracy of the receiver Analog-to-Digital-Convertor

(ADC). In [114] also authors noticed of -40 dB quantization noise due to using of a 8-bit ADC. But in studies like [116], even after using a high resolution ADC (14-bit), the dynamic range was significantly reduced in real multipath environment. So, in this chapter, we will show despite the fact that receiver ADC bit resolution puts theoretical limiting SNR specifications to the measurement, it may not be the limiting factor in correlation DR but the self-noise due to correlation type can. This can help prevent from significant misinterpretation of the ADC data sheet specifications and expected DR. Awareness of the self-noise and cause for it is necessary if one is to suppress it.

In summary, in the rest of this chapter, rather than designing or modifying the LS family sequences, we will focus our efforts on a quantified simulation and measurement-based study of the impact of thermal (channel SNR) and quantization noise (ADC bit resolution) on the performance of existing LS sequences used in the proposed channel sounder of Chapter 5. This includes simulating the effects of channel SNR, Receiver ADC resolution and types of correlation used. As a practical application, the minimum transmit power level required to characterize the channel can be predicted using the presented results.

4.2 Concepts

4.2.1 Construction of LS Codes

LS sequences were proposed as a candidate for the 3G wireless communications standard in 2000 [117]. They are generated using Golay pairs which are binary sequences proposed by Golay in 1961 and their sum of aperiodic auto-correlation function is a Kronecker delta while sum of aperiodic cross-correlation function is zero for all time shifts. Golay sequences are useful if they exist. He proposed a non-recursive algorithm to generate binary pairs with lengths of $2L_1$ and $2L_1L_2$ from sequence with L_1 and L_2 lengths using interleaving and concatenating, respectively [118]. He also showed that operations of equivalence between sequence pairs and some particular pairs cannot be generated from the proposed algorithms, so called Golay kernels proven to be with lengths of 10, and 26 [119], [120]. Later, by combining the Golay kernels, algorithms were suggested to generate Golay pairs with lengths of $L_{Gol}=2^N.10^M.26^P$ where N,M and P are non-negative integers [121]. There are still unknown Golay binary pairs of different from L_{Gol}.

Assuming *S* and *C* as subsequences of Golay complementary pair whose components are ± 1, LS sequences can be obtained with zeros inserted between these pairs and if (C_1,S_1) and (C_2,S_2) are both Golay pairs of LS sequences, then two LS sequences are called mates. The basic idea of the LS sequences is the insertion of zeros to avoid that the sequences C_1 and C_2 overlap with the sequences S_1 and S_2 to result in the desired aperiodic IFW zone. In our work, we use Golay sequences generated by the systematic algorithm proposed in [109] in where given the initial Golay pairs of (C_1,S_1), (C_2,S_2), Laurent polynomials were used iteratively to obtain desired length of Golay sets.

$$\begin{bmatrix} C_1 & S_1 \\ C_2 & S_2 \end{bmatrix}(set1)_1 \rightarrow \begin{cases} \begin{bmatrix} C_1C_2 & S_1S_2 \\ C_1-C_2 & S_1-S_2 \end{bmatrix}(set1)_2, \rightarrow \begin{cases} \begin{bmatrix} C_1C_2C_1\text{-}C_2 & S_1S_2S_1-S_2 \\ C_1C_2-C_1C_2 & S_1S_2-S_1S_2 \end{bmatrix}(set1)_3, \\ \begin{bmatrix} C_1-C_2C_1C_2 & S_1\text{-}S_1S_2S_1 \\ C_1-C_2-C_1\text{-}C_2 & S_1-S_2-S_1\text{-}S_2 \end{bmatrix}(set2)_3, \end{cases} \\ \begin{bmatrix} C_2C_1 & S_2S_1 \\ C_2-C_1 & S_2-S_1 \end{bmatrix}(set2)_2, \rightarrow \begin{cases} \begin{bmatrix} C_2C_1C_2\text{-}C_1 & S_2S_1S_2-S_1 \\ C_2C_1-C_2C_1 & S_2S_1-S_2S_1 \end{bmatrix}(set3)_3, \\ \begin{bmatrix} C_2-C_1C_2C_1 & S_2\text{-}S_2S_1S_2 \\ C_2-C_1-C_2\text{-}C_1 & S_2-S_1-S_2\text{-}S_1 \end{bmatrix}(set4)_3, \end{cases} \end{cases} \cdots \tag{4.1}$$

The LS mates obtained by this algorithm and use of (4.1) sets will generate IFW zone of length W_0, within the interval of *[-d,...,d] as*

$$W_0 = L_{Gol} - 1, \tag{4.2}$$

where L_{Gol} is the length of Golay subsequences. However, IFW length will reduce to $W_0/2$ or $W_0/4$, *etc.* if mates from different sets are used. The IFW zone length can be calculated as time duration as

$$T_{IFW} = 2\tau_{IFW} + 1, \tag{4.3}$$

where T_{IFW} is the length of interference free window in delay axis and τ_{IFW} is defined as distance between auto-correlation peak location and end of the IFW zone and is proportion to the chip rate of the transmitter, T_C.

4.2.2 Design Tradeoffs

Zero insertion creates IFW zone but reduces the energy efficiency of the LS sequences in practice. The energy efficiency of each of the LS mates (LS_i) can be calculated as [109]

$$\eta = \frac{\sum_{n=0}^{2L_{Gol}+W_0-1} |LS_i(n)|^2}{2L_{Gol}+W_0} = \frac{1}{1+\frac{d}{L_{Gol}}} \le 1 , \tag{4.4}$$

where equality happens when $W_0=d=0$. So in practice the W_0 is selected as small as possible but cannot be smaller than maximum excess delay (τ_{max}) of the environment in which these sequences are being used. In practice it is reasonable choice to select $\tau_{IFW}>\tau_{max}$. One other remedy for low-energy efficiency of LS sequences is to use very long sequences, but this will be more appropriate in static environment where channel can be assumed stationary while recording the data.

The correlation properties of LS sequences within IFW zone is given as [16]

$$R_{ij}(\tau) = \sum_{i=1}^{N-1} LS_{j,i} LS_{k,(n+\tau)\bmod N} = \begin{cases} N, & \text{for } \tau = 0, j = k \\ 0, & \text{for } \tau = 0, j \neq k \\ 0, & \text{for } 0<|\tau|<\tau_{IFW} \end{cases} . \tag{4.5}$$

Moreover, according to previous studies, there is a bound on the length of IFW with respect to the family size and the length of the sequence [122]

$$W_0 \le \frac{N}{M} - 1 . \tag{4.6}$$

It can be seen from (4.6), that the family size of LS sequences can never exceed the length of the sequence. This may be a limiting factor when LS sequences are used in CDMA network in where larger sequence family size is desired. However in the channel sounder application of Chapter 5 we will just need two LS mates.

4.2.3 Effect of Channel Imperfections on Dynamic Range

In a practical channel sounder, the dynamic range can be restricted by several factors such as system noise, power amplifier nonlinearities, the TX-RX chip rate differences, low resolution ADC, and self-noise due to correlation operation. For an example considering a PN sequence length of L, the ideal (noise free) correlation dynamic range is given by $10log_{10}(L^2)$ and in a noisy channel, it is given by [123]

$$\mathrm{DR}_{AWGN} = 10\log_{10}(\frac{L^2}{N_0 B}) \ , \tag{4.7}$$

where N_0 is noise power spectral density and B is the bandwidth of the PN sequence. However, there is no closed form formula exist for LS sequences, *i.e.,* not thermal noise effect nor quantization noise due to ADC have been quantifiably studied for LS. In practice, LS sequences are used in a propagation channel with a finite SNR. assuming a linear time-invariant channel, *h(t)*, the output of the correlator at the receiver will be [113]

$$\begin{aligned} R(\tau) &= \int_{t=t_0}^{t_0+T} LS(t+\tau)[LS(\mathrm{t}) * \mathrm{h(t)} + \mathrm{n(t)}]\,\mathrm{dt} \\ &= h(\tau) * R_{LS}(\tau) + N_r(\tau) \ , \end{aligned} \tag{4.8}$$

where * is correlation operation, $R_{LS}(.)$ is autocorrelation of the LS sequence and $N_r(.)$ is the random noise component given by

$$N_r(\tau) = \int_{t=t_0}^{t_0+T} LS(t+\tau) n(t) dt \ . \tag{4.9}$$

Because of the ideal correlation properties of LS sequences within the IFW, in a noise-free channel, the correlator output in (4.8) will be equal to channel impulse response, *i.e.,* $R(\boldsymbol{\tau})=h(\boldsymbol{\tau})$. However, when the channel has finite SNR and receiver ADC is not ideal, (4.8) will be

$$R(\tau) = h(\tau) + N_s(\tau) + N_r(\tau) \ , \tag{4.10}$$

where N_s is the spurious noise which can be generated because of self-noise due to FFT or quantization noise due to non-ideal ADC bit resolution at the correlator output. This spurious noise due to FFT together with N_r which is due to channel finite SNR, can limit the dynamic range of the system and are the parameters that we will study in next sections.

4.3 Simulation and Measurement Methodology

In our work, we used the algorithm explained in the previous section to generate LS mates with different lengths for our study. Within this section we will describe the precise details of the derivations, simulations and measurements that we have performed in order to yield the results that we will present in next section. The main simulation/measurement goals are:

1. To study the effects of typical propagation channel noise (additive white Gaussian noise) on the dynamic range of the channel sounders working with LS sequences and compare with dynamic range of the PN sequence of the same length.
2. To prove that the dynamic range of any spreading sequence is less affected by the number of bits of receiver ADC than use of inappropriate correlation method (*i.e.*, periodic vs aperiodic).

4.3.1 Simulation

A systematic way to investigate these goals is to replicate the similar chain that LS sequences are used in a channel sounding application. For this reason a simulation chain in MATLAB was considered including *LS sequence generator*, *modulator, the channel*, *demodulator* and the *correlator*. Figure 4-1 shows the main components of the simulation steps followed by a brief description for each module.

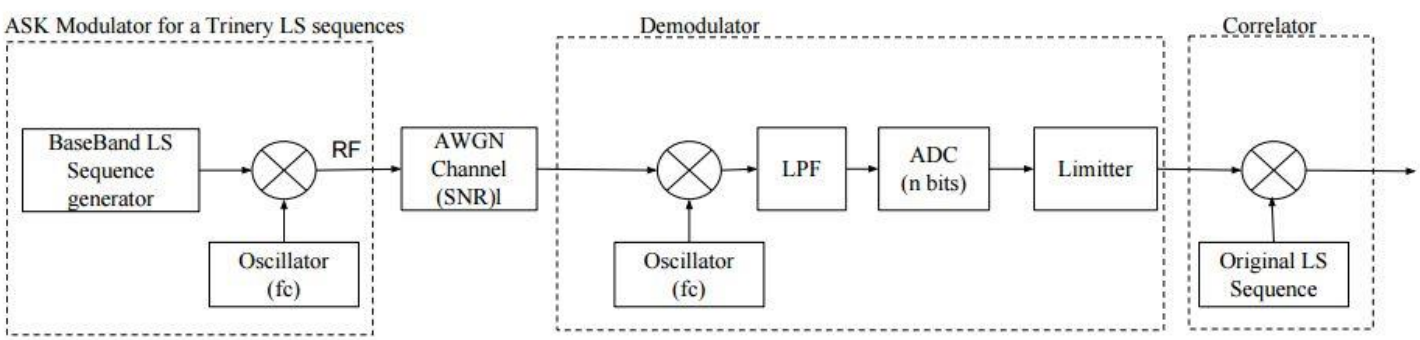

Figure 4-1: Simulation steps implemented in MATLAB.

Sequence generator: The algorithm described in previous section is used to generate two mates of LS sequences with desired lengths. Golay complementary pairs of C_0=[1,1] and S_0= [-1,-1] are used as initial seeds in the generation algorithm.

The modulator: Since LS sequences are trinary, we used Amplitude-Shift Keying to modulate the signal. The +1 and -1 polarity are mapped into *+5* and *2.5* volts respectively whereas zero is mapped to zero, *i.e.*, no signal. The rate of the baseband LS signal was considered as 10MS/s as an example. A cosine wave with carrier frequency of 2GHz was then used for transmitting data into RF frequencies. In practical implementation, we will make transmitter ‘off’ to transmit zeros as will be described later.

Additive White Gaussian Noise (AWGN) channel: AWGN is a basic noise model used in information theory to mimic the effect of many random processes that occur in a channel and adds white Gaussian noise to the vector of the signal. The SNR of the channel is one of the parameters we alter between the simulations repeat to study thermal noise effect on correlation dynamic range. *awgn* function of the MATLAB was used for this purpose.

Low Pass Filter (LPF): In order to implement a LPF, there are several functions in MATLAB such as the Filter Design and Analysis Tool (FDA Tool) which enables quick design of filters by setting filter performance specifications, and importing filters from MATLAB workspace, or by directly specifying filter coefficients. However, we used averaging function in order to separate the demodulated baseband LS bits from high frequency signals resulted from multiplier.

Analog-to-Digital convertor (ADC): Depend on the number of bits resolution, ADC will return the input baseband signal digitized in specific levels and intervals. The bit resolution of the ADC has effect on DR because of introducing quantization noise and is studied as a parameter of simulation in this chapter.

Limiter: A multi-level detector is used as a limiter in order to improve the performance of the system and is consist of two levels of thresholding at half of the amplitude of the modulated LS sequences.

Correlator: This module is considered as post processing stage and depends on the type of the sounding signal, different type of correlation can be selected. As we will show in the following section, when PN sequences are sent, periodic correlation reveals less self-noise compared to aperiodic correlation whereas both periodic and aperiodic correlation reveals almost similar correlation DR for LS sequences. In the rest of this chapter, by “correlation dynamic range” we mean the minimum of the cross and autocorrelation dynamic ranges. The correlation function was implemented using the *xcorr* function of MATLAB.

4.3.2 Measurement

For the measurement study, we used R&S SMW200A dual port vector signal generator [124] to modulate and transmit two orthogonal sequences with different lengths each time in order to study the DR of these sequences when they are used in non-ideal condition (*i.e.*, finite channel SNR). We used Keysight (formerly Agilent Technologies) PXA N9030A to record the raw I&Q data. PXA has a large ADC resolution (16-bit) and according to our previous simulation results, this has negligible effect on DR. So in this section the measurement reduces to the DR degradation mostly due to channel thermal noise. Figure 4-2 represents the main internal modules of the SMW200A unit along with the wired connections to the PXA and post processing correlation module. SMW has two separate outputs that are synced and each has its own fading and AWGN module. These modules will be used in next chapter when we apply different types of fading on signal to characterize our proposed channel sounder. In this section the LS sequences of different lengths were loaded into the SMW memory after replacing the '-1's with zeros and using R&S CDM toolbox to produce baseband sequence with BPSK modulation. In order to account for zeros of the original LS sequence and transmit them, transmitter had to be switched off when zeros were sent. We created a control power ramp signal in the CDM toolbox and loaded into SMW to attenuate the transmitter output with a large value when a '0' was sent [124]. This replicated the transmitter 'off' status. The response time of the control signal was fast enough not to miss any baseband LS bit.

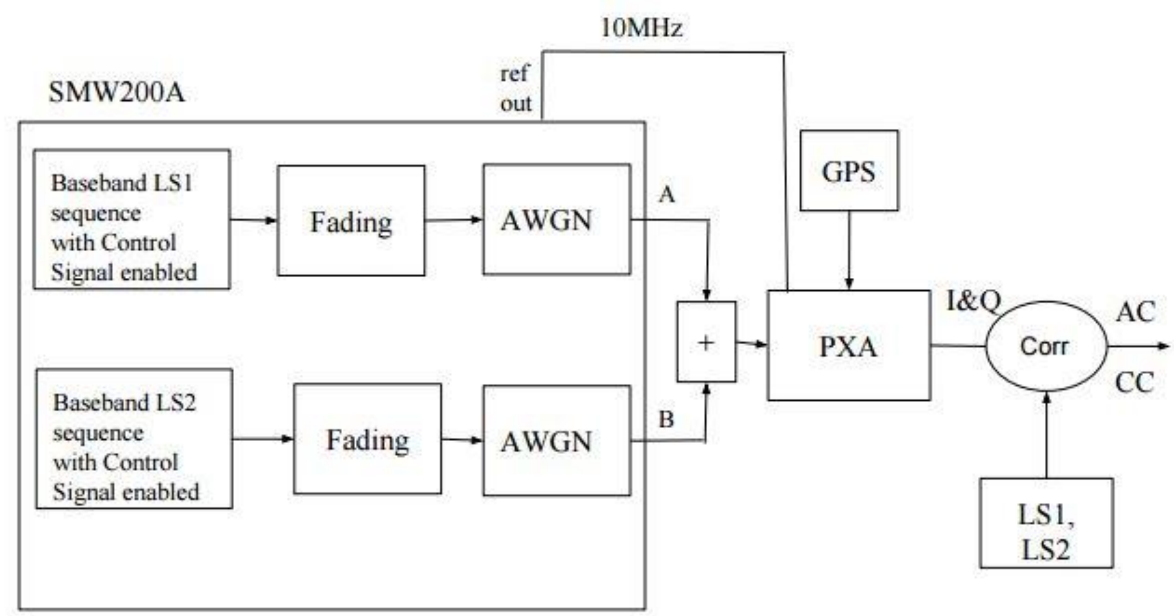

Figure 4-2: Bench top measurement setup.

4.4 Results

This section summarizes the results obtained in simulation and measurement using the approach explained in previous section.

4.4.1 Effect of Channel SNR on Correlation Dynamic Range of LS Sequences

Using the simulation chain of Figure 4-1, LS sequences of 256, 512, 1024, 2048 and 4096-bit lengths were used to simulate and study the effect of thermal noise (channel SNR) on their correlation dynamic range. These lengths were chosen since they are commonly used and are applicable to channel sounders in practice. SNR of the channel was varied and DR of the received signal at demodulator was obtained using aperiodic correlation. Figure 4-3 shows the result of SNR on correlation DR of the above-mentioned LS lengths.

Conclusions:

1. The performance of LS sequences under low SNR is not ideal anymore and is limited due to effect of noise. The figure quantifiably shows how badly LS sequences' DR can degraded due to low SNR. It is seen that their ideal DR is degraded and is finite value for the channel SNRs of around 0-5 dB. Above this range, the DR is ideal and infinite. We call this SNR range the transition SNR.
2. For channel SNR below the transition SNR, longer LS sequences show higher DR. However, longer sequences are less suitable for use in real time channel sounders in which Doppler range is an important factor. We will discuss more about this in the next chapter when we discuss the limitations of the proposed channel sounder.

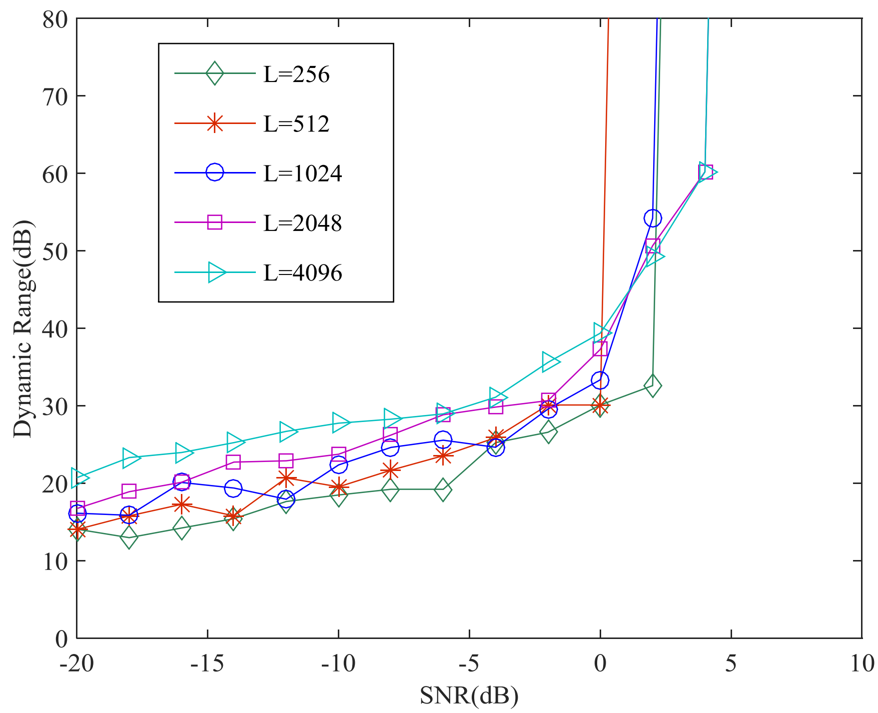

Figure 4-3: LS Correlation dynamic range versus channel SNR (with limiter).

3. It should be noted that the results above are presented when a limiter is used in post processing of the data (as seen in Figure 4-1). In order to show the importance of limiter when dealing with correlation of sequences which information exist in the zero crossing (similar to the FM demodulation), we simulate the same scenario without limiter as well. Only 1024-bit sequence length is chosen for comparison but the results show similar trend for the other lengths. Figure 4-4 compares both scenarios.

4. It is observed that if limiter is not used, the DR of the LS sequences will not be ideal after the transition SNR value as we showed in Figure 4-3, but it will increase the DR gradually. However, it is arguable that the implementation of the limiter with multi-level threshold in practice is challenging when the amplitude of the received signal is unknown at the receiver.

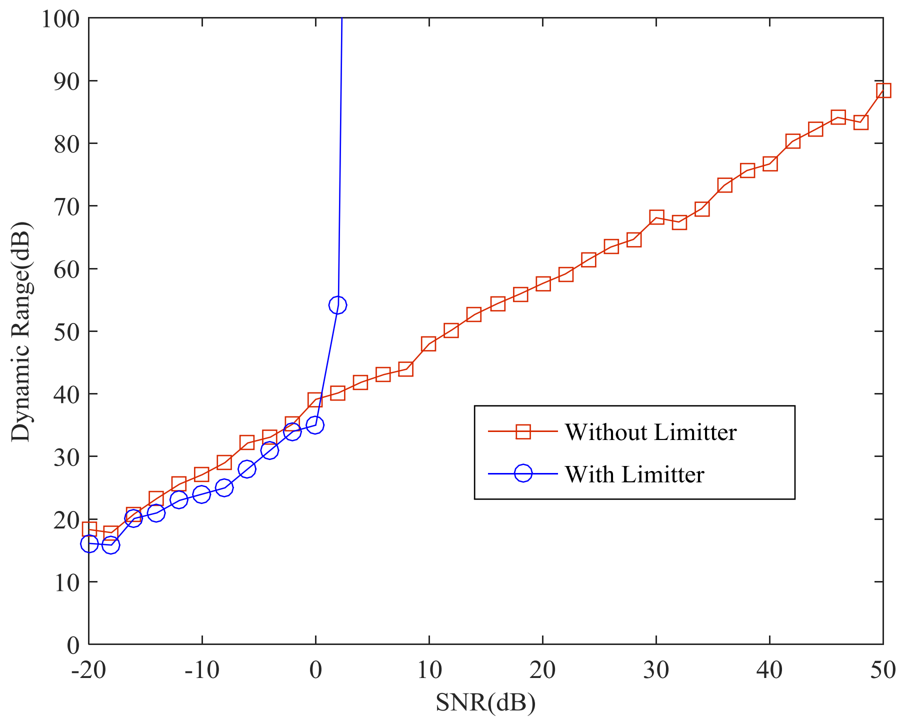

Figure 4-4: Effect of limiter to improve thermal noise effect on dynamic range of 1024-bit LS sequences.

Using the bench-top test setup of Figure 4-2 gives us a controlled environment to study effect of channel SNR on correlation DR of these sequences. LS_1 and LS_2 sequences were sent from channel A and B, respectively with 50MS/s rate and were captured in PXA with 100MS/s sampling rate. we measured DR of the different LS sequences lengths of 511, 2048 and 8196-bit when the TX output power of each channel was varied between the measurements to create different channel SNRs. For each measurement, the SNR value was obtained by subtracting the output TX power and the noise floor of the received signal averaged over the 100 indexes. The aperiodic correlation was performed offline after IQ data was recorded by PXA. Figure 4-5 shows a normalized sample of measured DR using LS length of 2046-bit with SNR=20 dB. The AC and CC DR were found to be same. Figure 4-6 shows the comparison between measured and simulated DR under different SNR values for different lengths of LS sequences. Note that we haven't applied any limiter function described previously, in the post processing of the measured data.

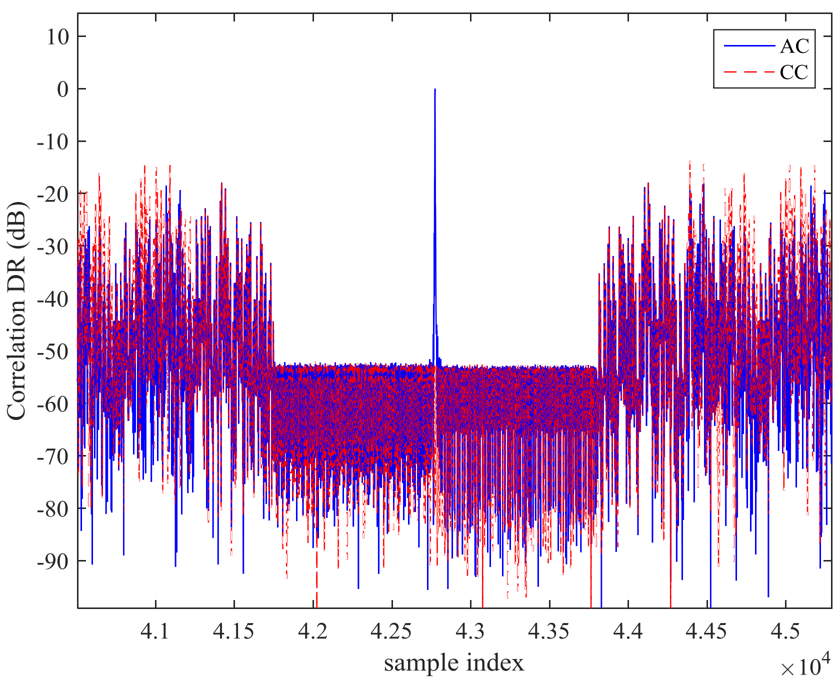

Figure 4-5: The IFW zone and measured AC and CC dynamic range with LS sequence length of 2046, SNR=20 dB.

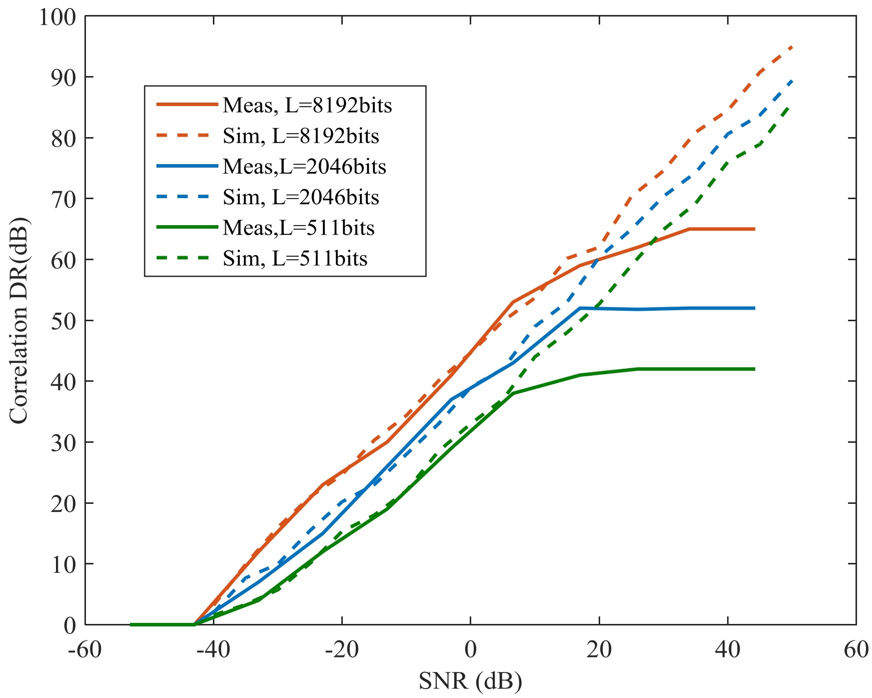

Figure 4-6: Measured/ simulated dynamic range versus channel SNR for different lengths of LS sequences.

Conclusions:

1. Under a fixed SNR value, increasing the length of the LS sequence increases correlation DR as plotted in the Figure 4-6.
2. By increasing channel SNR, DR of LS sequences increases in measurement and is matching the simulated results we got in previous section. Similar to the simulation results, in low SNR their performance is degraded and is not ideal anymore. In large SNR, the generator saturates and because of that the DR values are almost fixed above 40 dB channel SNR.

4.4.2 Comparison of the Performance of PN and LS Sequences

A maximum length PN sequence using linear feedback shift-registers and generator polynomial is generated for performance comparison with LS [125]. The resulted PN sequence using these specified polynomials have the best (maximum) auto correlation dynamic range among all other possible PN sequences of same length. We used a typical BPSK modulation simulation chain of MATLAB communication toolbox [126], [127] and passing the PN modulated sequence through a channel with variable SNR to calculate effect of SNR on correlation DR (with presence of limiter in the simulation chain). Figure 4-7 compares the AC

DR of PN and LS sequences of the same length (1024-bit). Only AC dynamic range result is presented since there is no perfect orthogonal PN sequence for CC calculation.

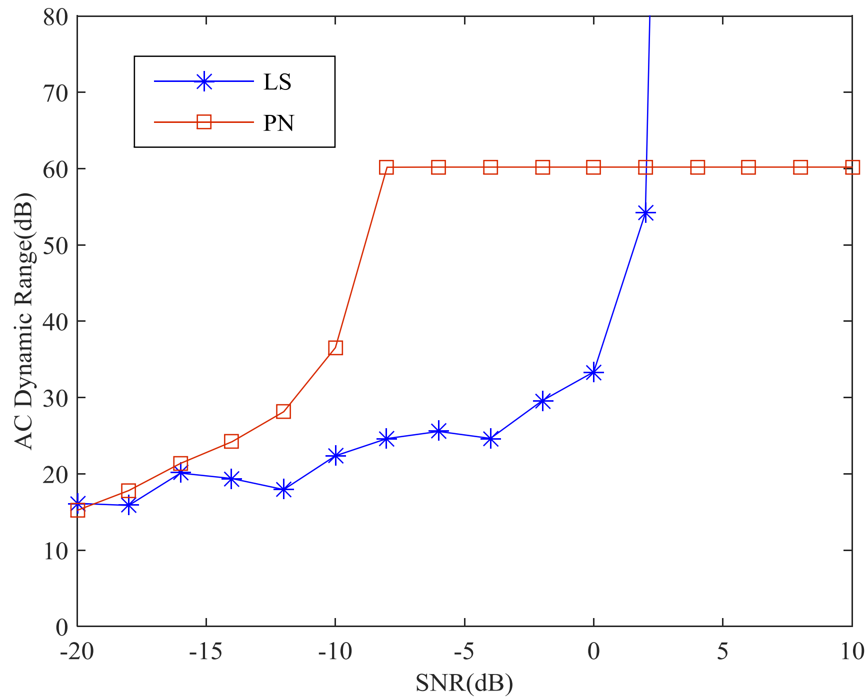

Figure 4-7: AC dynamic range comparison of 1024-bit LS and PN sequences.

Conclusions:

1. It is seen that similar to LS sequences, PN sequences DR degrades in low SNR values. The maximum DR of PN length of 1024-bit is 60.2 dB which is met for SNR values above -5 dB. This implies that transition SNR for PN is lower compared to LS and this is mainly due to the higher energy efficiency of these codes compared to LS.
2. AC DR curves of PN and LS sequences of same length intersect around LS transition SNR values. At this point these sequences may be replaced with each other if only AC DR performance is of interest.
3. Although DR of PN and LS sequences are comparable in low SNR condition but in higher SNR, LS sequences outperforms PN sequences. Moreover, LS sequence will outperform PN if cross correlation dynamic range is considered.

Using the bench top test setup with PN sequences for comparison, the CDM toolbox of R&S was used to generate BPSK modulated PN sequences and load them into the instrument. The PN pairs used here were generated similar to the method described in previous sections. As seen in Figure 4-8, measured AC DR of PN and LS sequences of same lengths (511-bit) are compared with their simulated values. It is observed that under realistic channel condition, AC DR of LS is comparable to PN sequences with same length. However, LS sequences are advantageous if CC DR is important, *e.g.*, in CDM-based MIMO channel sounding.

4.4.3 Effect of ADC Bit Resolution on Correlation Dynamic Range

In order to see the effect of number of ADC bit resolution on LS correlation DR, same simulation chain of Figure 4-1 was used with LS sequence length of 1024-bit under several channel SNR values. The limiter was not used in order to remove its improvements effects and just have effect of ADC. Figure 4-9 shows the LS DR under different channel SNRs. similar result was obtained using the PN sequences.

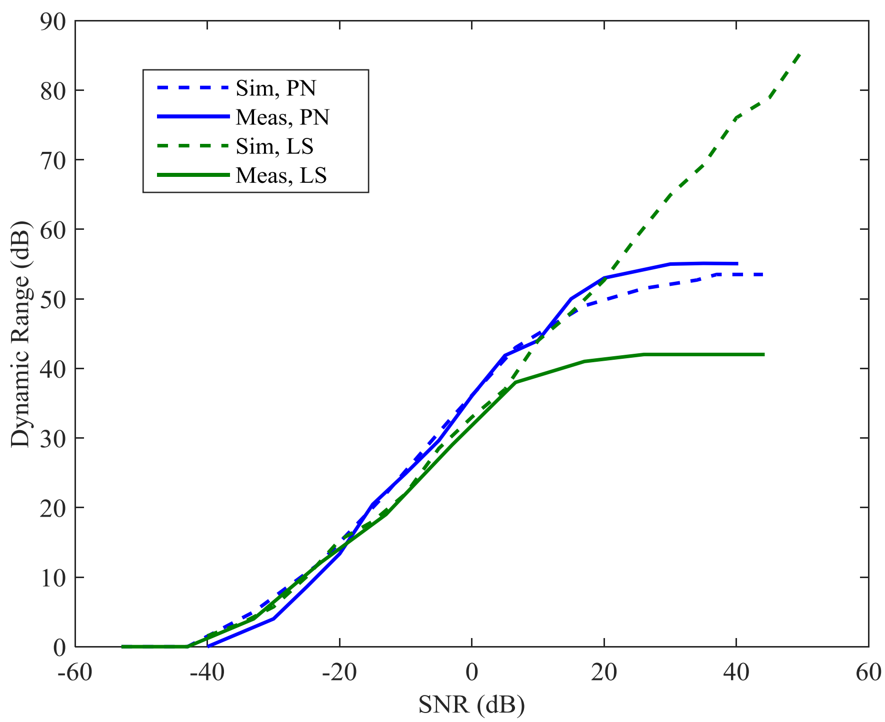

Figure 4-8: AC Dynamic range comparison of PN and LS sequence of 511-bit in different channel SNR.

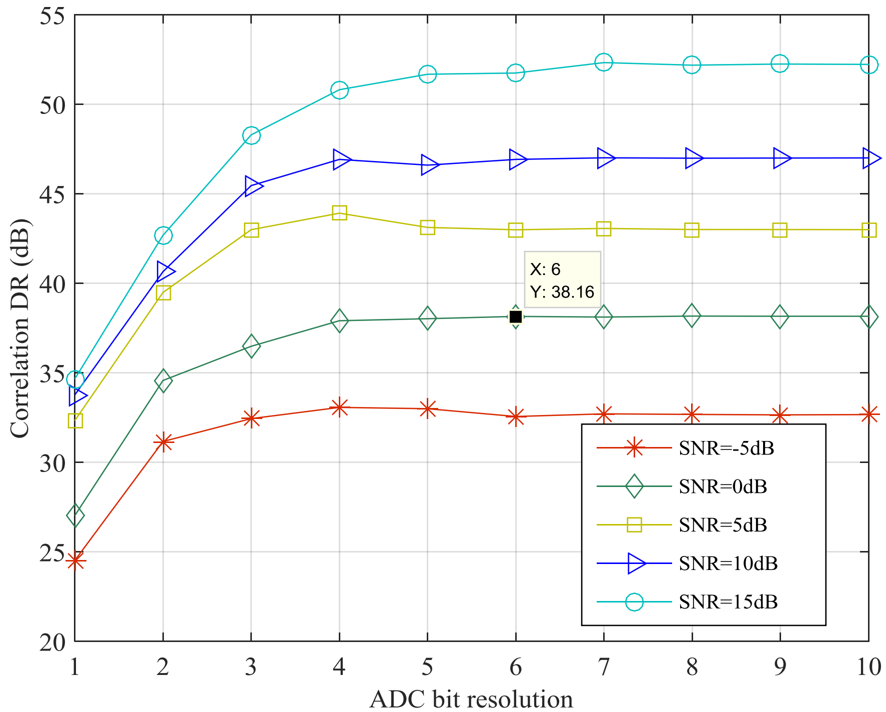

Figure 4-9: Effect of ADC bit resolution on correlation DR.

Conclusions:

1. Increasing the number of ADC bit resolution will increase correlation DR of the LS sequences. The DR improvement is significant (7 dB in low SNR values up to 20 dB for larger SNR condition) when ADC bit resolution is increased from 1 to 5 bits but above 5 bits, DR remains almost unchanged.
2. The result implies that using a receiver with typical ADC resolution (*e.g.*, 8-12 bits which is common in practice), will be adequate enough not to be limited by quantization noise when doing channel sounding. On the other hand it is recommended to improve other channel sounder equipment and post processing imperfections that can improve the maximum achievable DR significantly. As an example and also as a practical consideration, type of correlation (*i.e.*, periodic or aperiodic) can be an effective on the amount of self-noise therefore on the system DR as described in more details at following.

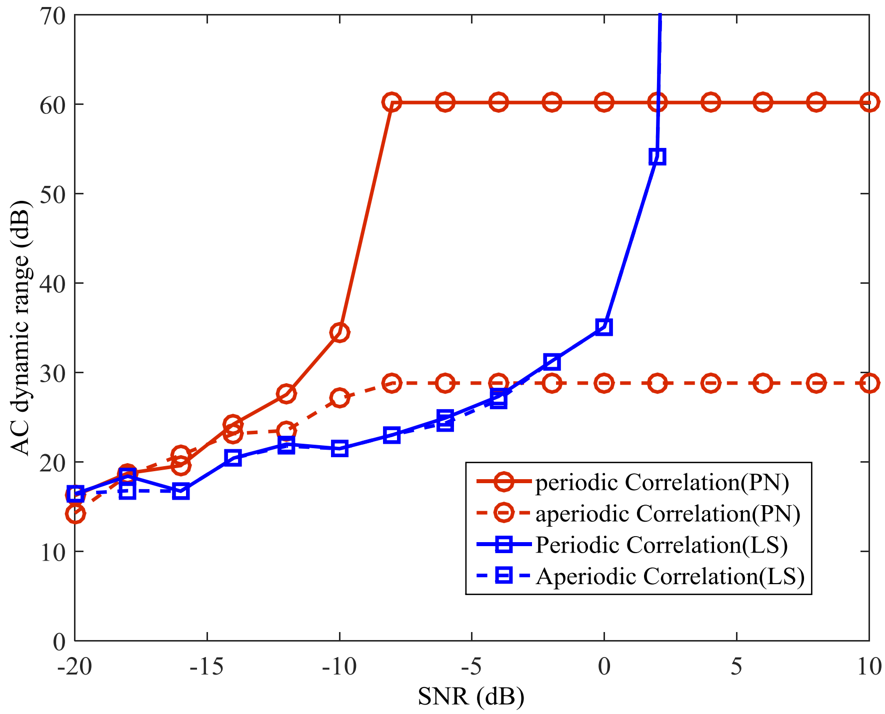

Figure 4-10: Effect of Self noise due to different correlation types on LS and PN dynamic range.

4.4.4 Effect of SNR on Auto and Cross Correlation Dynamic Range

In order to show the amount of DR improvement when using proper type of correlation, we used PN and LS sequences length of 1024 as an example in our simulation chain. The DR was obtained each time using circular (periodic) and linear (aperiodic) correlation at the post processing stage. It was observed that PN sequences self-noise introduced by aperiodic correlation was far higher than periodic one such that under circular correlation their DR matches to the theoretical values. However, both circular and linear correlations revealed almost similar DR for LS sequence that is due to existence of zeros between Golay's pair within its structure. Figure 4-10 shows the effect of correlation type on both LS and PN sequences under different channel SNRs.

4.5 Discussion

Dynamic range degradation of Loosely-synchronized sequences has already been observed in the previous studies in where people used these sequences to measure response of the channel but a quantified study of performance degradation due to *Thermal* and *Quantization* noises (*i.e.*, propagation channel with finite SNR and receiver with finite number of ADC bit resolution, respectively) is missing in the literature. In this chapter, the performance of the Loosely Synchronous sequences in the presence of mentioned channel sounder non-idealities was studied. We showed the effects of channel SNR value, receiver ADC bit resolution and types of correlation on the correlation dynamic range in our simulation and measurement-based study. More specifically we showed:

1. Under the effect of noise, LS sequences correlation dynamic range reduces to a finite value and the interference free zone is no longer holds. The amount of reduction is different based on sequence length and channel SNR such that LS sequences with longer lengths show more correlation DR and amount of DR reduction under noise is less compared to shorter sequences. Moreover, it was observed that the studied LS sequences are resilience to channel thermal noise degradation up to 0-5 dB of channel SNR, which we call this as transition or threshold SNR. Below this value, performance of these sequences degrades. The threshold SNR for PN sequences was shown to be lower mostly because of their larger energy compared to LS.
2. Although LS sequences show superior DR (both AC and CC DRs) compared to PN sequences, under certain channel SNR, their AC dynamic is comparable to PN. This gives an insight on using these sequences alternatively when doing non-CDM MIMO channel sounding in where AC function is the main performance metrics. However, LS sequences outperform PN considering CC DR.
3. Increasing ADC bit resolution from 2 to 5 bits will increase the DR values significantly (*e.g.*, 7 dB improvement when channel SNR is low and 20 dB for a channel with high SNR). For resolution of more than 5 bits it was shown that the effect of ADC bit resolution on DR is negligible. We further investigated the root for DR degradation that was observed in previously implemented channel sounders even though they used high resolution ADCs. We showed that using proper type of correlation (circular and linear), self-noise reduces and approaches to the theoretical values, and in fact it should be selected based on the properties of the sequence. For periodic PN sequences we showed periodic correlation will reveal better DR compared to aperiodic one whereas for LS both correlation types resulted in very same results mainly because of existence of zeros in their structure.

The insights presented in this chapter allow the operator of the channel sounder to adjust transmit power properly before the measurement and based on the channel SNR information in order to achieve the proper measurement DR. They also help to determine minimum quality of the receiver resolution in order to assure of enough dynamic range. Moreover, they prevent misinterpretation of the receiver ADC data sheet by emphasizing type of correlation as the origin of the correlation self-noise instead of ADC number of bit resolution which traditionally has been considered as one of the limiting factor of channel sounder dynamic range.

In this chapter, only one type of ZCZ sequences (*i.e.*, LS) was studied. Since these sequences are gaining more attraction to be used in MIMO channel sounders, further studies on the performance of these sequences are recommended using different types of ZCZ families preferably ones with more energy efficiency. It is also recommended to compare the performance metrics with other types of sequences as well (*i.e.*, other than PN which was used to compare our result with in this chapter). Moreover, other channel sounders non-idealities should be studied such as power amplifiers nonlinearity effects on LS sequence dynamic range. In this work we used only two LS sequences since our channel sounder in next chapter is MIMO 2×2. It is desired to consider larger family sizes of LS sequences for performance studies if higher order MIMO channel sounding is required.

Chapter 5: Use of Fibre-Optic Delay Lines to Conduct Multi-Antenna Channel Measurements with a Single-Channel Receiver

5.1 Introduction

Knowledge of the radio channel properties is important for design and deploying any wireless system, especially for less explored environments such as Smart Grid (SG) and advanced cellular systems, *e.g.*, 5G. Numerous efforts have been devoted to developing more reliable and cost effective channel sounders in past decades [128]. With the advent of Multiple-Input Multiple-Output (MIMO), the stepping correlator channel sounder, introduced by Cox in 1972 [129], has played an important role in measurements of such channels because of their simplicity, real-time measurement capabilities, inherent robustness to interference and large dynamic range due to use of direct sequence spread spectrum (DSSS) techniques [130]. These channel sounders uses correlation operation between original transmitted pseudo random binary signal and received signal to achieve specific correlation gain [131], [132]. In essence, there are three main methods of multiplexing by which transmitting antenna can be identified by the receiver, which includes Time (TDM), Frequency (FDM), and Code (CDM) division multiplexing methods and the choice of the multiplexing technique is constrained mainly by the adopted hardware strategy and required measurement resolution.

The Fully Switched MIMO sounding architecture has been widely accepted due to its straightforward implementation and calibration, low complexity signal processing and relatively low cost. Most commercial MIMO channel sounders use time multiplexed transceiver architecture [133]. They consist of single radio front-end at both sides of transmitter and receiver to switch between antenna elements in row [90], [134], [135]. This TDM-based SISO type channel sounding is more suitable for static or quasi-static channels in which the channel remains invariant for the length of the time required to complete all combination of Tx-Rx antenna measurements. Depends on the number of antennas, the measurement time can be exhaustive resulting in uncorrelated phase noise between different channel estimation and influence the estimated MIMO channel parameters [136]. Moreover, at every switching, the Tx and Rx should keep synchronization which has been proven to be a challenging issue [137].

Semi-switched architecture, on the other hand, alleviates this problem by using multiport/multiple receivers to simultaneously capture all channels, whereas TX can be implemented either by FDM method by offsetting the carrier frequency of different antennas [17], [138] or TDM approach using switches or multiple transmitters [139]. FDM methods enable all TX antennas to transmit concurrently by allocating orthogonal subcarriers for each antenna. The subcarrier allocation can be a combination of comb or block type [116]. However, the major drawback of FDM-based channel sounding techniques is that the data model needs to be modified, since the frequency sample points in each transmitting antenna are different [17].

Use of multiple transmitters to apply time shifts between the TX signals, on one hand is not cost effective and on the other hand it has the same problem that switches have, *i.e.*, delay between the channel measurements, therefore it is not a viable option for measuring dynamic MIMO channels with high Doppler rates. The issue with using switches for MIMO channel sounding has been raised by many authors [21], [136], [140]–[142]. Issues such as relatively slow measurements in fast variant environments and added phase noise, inaccurate parameter estimation because of switching delay and cost of acquiring high power switches at transmitter especially at high frequencies are addressed.

This leaves *Fully Parallel* MIMO channel sounding method the only viable option to realize a real-time channel sounder in dynamic environment. The conventional way of implementing fully parallel sounders is using low cross-correlated sequences transmitted simultaneously and recorded by a multiple-input receiver. Sequences such as Loosely Synchronized, Gold, Kasami have been implemented successfully [16], [87], [108]. *E.g.,* in [16] the applicability of LS codes in Urban/Suburban environments was verified by simulations and concluded that either LS codes or modified LS codes can be chosen for channel measurement. However, the hardware cost of the CDM based MIMO channel sounders due to use of expensive multiple-input or multiple receivers are generally poor.

As stated above, many options exist for measuring static and quasi-static MIMO channels, but measuring dynamic MIMO channel is more challenging. It is clear that channel sounder construction is a trade-off between cost and performance. Most of the previous works reviewed above have aimed for improving performance with sacrificing the cost or vice versa. So, there are benefits reforming the architecture of MIMO channel sounder in order to overcome limitations in measuring MIMO channel responses in fast varying environments and at the same time keep the implementation cost low. We will show that the multi-channel receiver can be replaced by a single-channel receiver equipped with a set of fibre delay lines configured as a delay-line multiplexer. We design a receiver with single input using fibre delay line in order to capture snapshot of the response of polarization antennas. This allows the responses from the array of receiving antennas to be stacked in time and observed with a much less expensive single input correlation-based receiver. It should be mentioned that there are other options to be used as delay line such as coax cable but the advantages of the fibre cables beside its lighter weight and lower cost, is consistency of its phase response when exposed to bending or mechanical pressure. This helps to have more consistent and repeatable channel sounding measurements.

Although in this work we devoted our effort on design and implementation of a dual polarized 2×2 channel sounder, *i.e.*, MIMO with polarization diversity, the technique is extendable to the co-located MIMO with space diversity as well, *e.g.*, distributed antenna systems. The idea of capturing snapshot of both polarization channels improves the accuracy of the measurements in fast varying environment because the dynamics of the channel are measured more accurately by removing switching delay and reducing measurement time between different polarizations. Considering this with simultaneous transmitting the orthogonal sequences can reduce the measurement time by a factor of $N \cdot M$ compared to a full-switching measurement for a MIMO channel sounding of N by M channels. The other advantages of the proposed architecture compared to existing time-domain MIMO channel sounders are, on one hand, the low overall price of the channel sounder in contrast, for example, with the RUSK [134] and, on the other hand, the capability to re-utilize the whole equipment for other different applications since we use devices which present in most RF research labs.

In the rest of this chapter, we will develop the main design equations. We will show that the environment maximum excess delay and maximum SNR dynamic and Doppler range are the main determining factors of the design. We will explain the design trade-offs and limitation of the proposed channel sounder. Implemented sounder then will be described in terms of calibration procedure and performance evaluation in a back-to-back connection. Effect of using fibre delay line instead of switch on improving overall system ambiguity, and degradation of measurement noise floor, phase noise and Allan variance will be studied next along with proposing a strategy of using fibre for expanding the channel sounder efficiently for higher number of collocated MIMO sounding. In the last section, we will summarize the chapter and recommend the future work.

5.2 Channel Sounder Design

In this section, we will develop design equations and plots for a 2×2 dual polarized channel sounder which utilizes fibre delay line to create artificial delay on the signal of one of the inputs. In most systems of this sort, the capture memory is generally very deep and the total delay that can be measured far exceeds the typical delay spread observed. Using fibre optic delay lines to stack the responses allows channel responses from multiple antennas to be measured simultaneously but separated in time during processing and display. Figure 5-1 shows the architecture of the sounder including the delay line system. Both TX and RX are synchronized with an external 10MHz reference and 1PPS GPS signals.

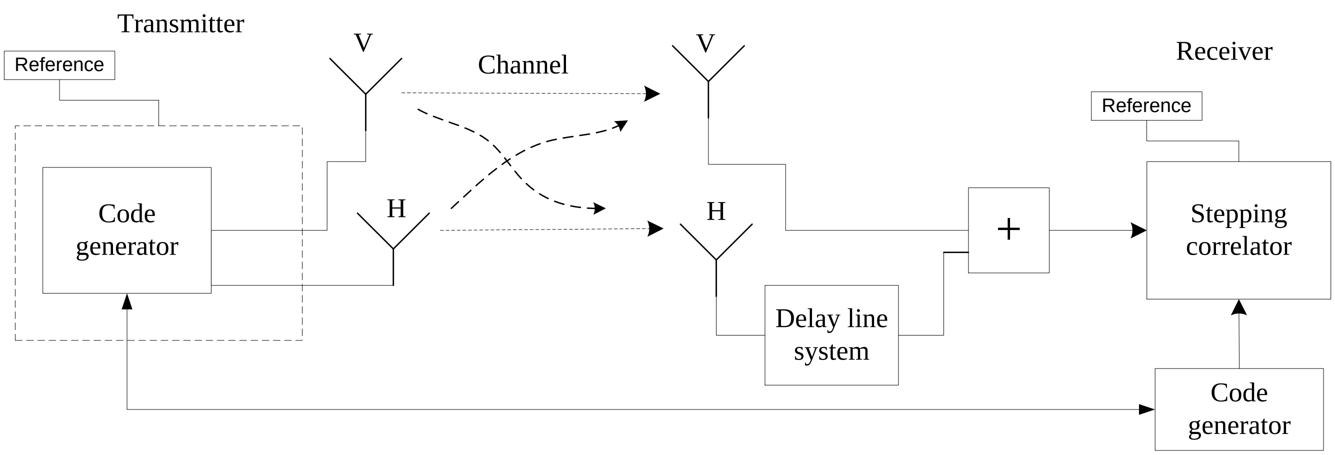

Figure 5-1: Architecture of the proposed channel sounder with LS sequence and delay line system.

Figure 5-2 shows the transmit and capture timing of the sequences at the transmitter and receiver side, respectively. The transmitter is sending continuously and each of the sequences is fed into V and H antenna inputs. At the same time receiver records both channel response from V and H antenna, such that the received signal at H antenna is passed through the delay line. This causes the H response from the receiver input to be delayed with amount of deliberately created delay value.

5.2.1 Design Equations

Considering just one of the captured snapshots, Figure 5-3 represents the relative position of V and H channel responses that they should have after the correlation. Out of the IFW zone the signals will not be detected due to self-noise of the correlation.

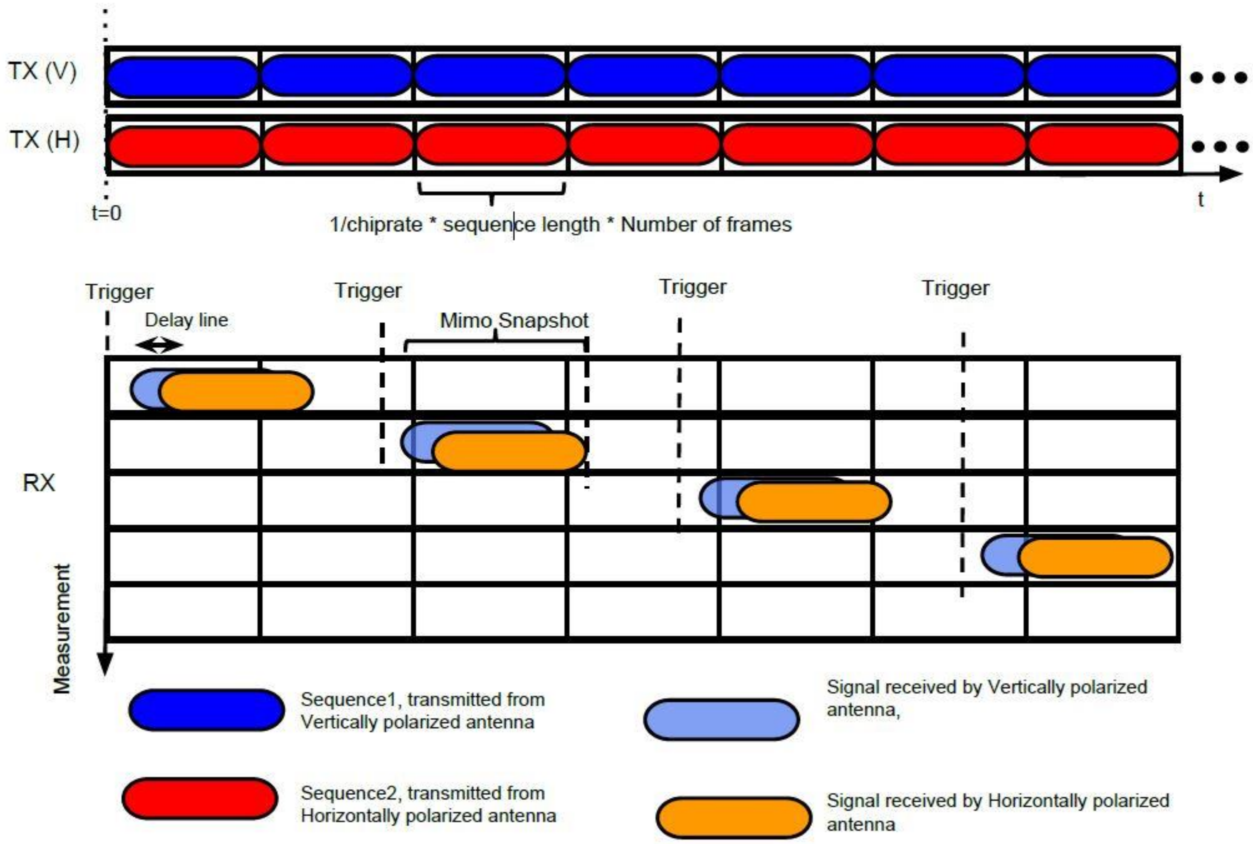

Figure 5-2: Sequences transmit and capture timing at the transmitter and receiver side.

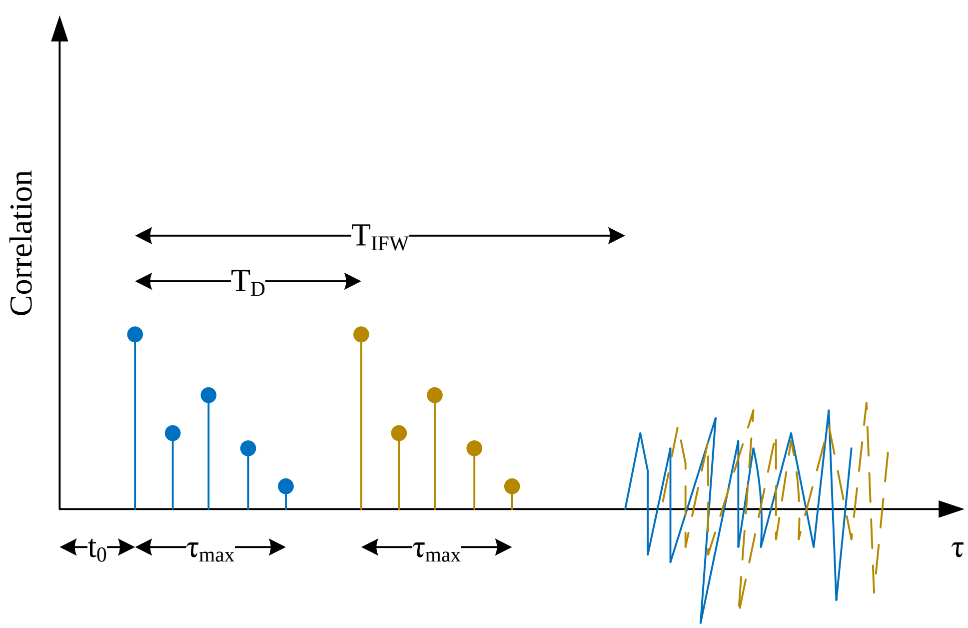

Figure 5-3: The relative position of V and H channel responses at the correlator output.

Table 5-1: Channel sounder design parameter description.

L_S	Length of the sequence in bits
T_{IFW}	Window of interference free window in bits
T_c	chip rate (bit/s)
Ts	Time resolution (s)
t_0	Absolute delay of propagation channel (sec)
T_D	Delay due to fibre delay line (second)
τ_{max}	Environment maximum excess delay (sec)
N_f	number of frames captured within each trigger
ε	Delay line dielectric permittivity

Table 5-1 summarizes the design parameters that need to be determined before implementing the channel sounder. In order to have an interference free detection of both polarization channel responses, following conditions should be satisfied.

$$\tau_{\max} \leq T_D \,, \tag{5.1}$$

$$2\tau_{\max} \leq T_{IFW} \,. \tag{5.2}$$

Equation (5.1) ensures there is no overlap between the responses at the output of correlator whereas (5.2) keeps them within the provided IFW zone. Using the relation between length of delay line and its propagation delay within its medium, *i.e.*,

$$T_D = \frac{L_D}{V_D} = \frac{L_D}{c_0 / \sqrt{\varepsilon_r}} \,, \tag{5.3}$$

then (5.1) becomes

$$\frac{c_0}{\sqrt{\varepsilon_r}} \tau_{\max} \leq L_D \,. \tag{5.4}$$

This is one of the design equations which given the maximum excess delay, the length of the delay line can be determined. Using the relation between sequence length and chip rate with IFW length,[109]

$$T_{IFW} = \frac{L-2}{4T_c} \ , \tag{5.5}$$

then (5.2) becomes

$$8\tau_{\max} T_c + 2 \le L_S \ . \tag{5.6}$$

This is the second design equation which is plotted in Figure 5-4 for different chirp rates. This implies that one can obtain the required LS sequence length with respect to the environment maximum excess delay for different measurement chip rates using the curves on the plot. Different environments depend on the selected noise thresholding value for processing the recorded CIR, can be distinguished based on their maximum excess delays such as indoor, office, suburban, urban, rural *etc*. (labels for different environments on the plot are just for an example and exact borders may vary for the specified environments). In summary, given the environment with its maximum excess delay value known, both minimum required sequence length and fibre delay line length can be estimated using the (5.4), (5.6) and Figure 5-4. Upon selecting the sequence length, the SNR dynamic range of the channel sounder can be determined from the results presented in Chapter 4.

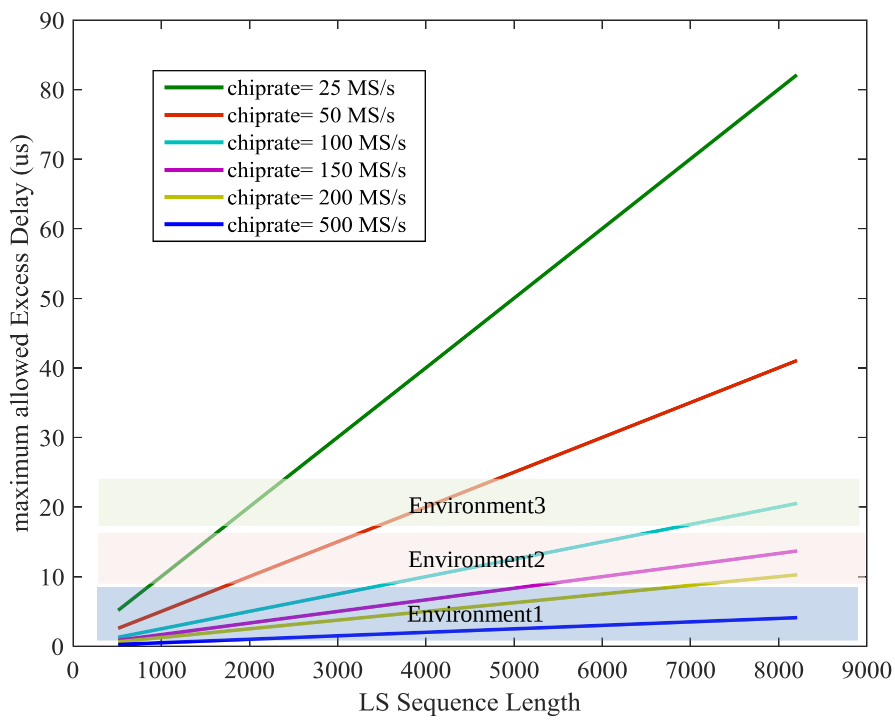

Figure 5-4: Design curves for the required sequence length based on maximum excess delay.

5.2.2 Design Tradeoffs

For static channel any sequence length can be selected as far as it satisfies required SNR DR. However, it is not the case when doing measurement in dynamic MIMO channels. Trade-offs are mainly between the following performance metrics:

a. SNR dynamic range: specifies the amount of auto-correlation and cross-correlation dynamic range of the channel sounder which specifies the minimum MPCs amplitudes detectable by channel sounder. In the previous chapter, we studied LS sequences in theory and practice and showed how correlation dynamic range is affected with channel SNR. The results can be used here to determine required sequence length based on required SNR DR.

b. Ambiguity: or Doppler coverage generally refers to the maximum range or time delay, or the maximum Doppler shift or velocity that can be detected without ambiguity [36]. This determines the waveform repetition frequency of the sounder, which has to be at least equal to $2f_{d\max}$. In our work we will consider it as the fastest length of time in which any changes in the propagation channel can be reflected meaningfully at the correlation output.

c. Time resolution: specifies the finest sampling distance between the data of the captured impulse response (IR). This is mostly dictated by the channel sounder hardware limits.

Table 5-2 shows the relation between these trade-offs.

More on Ambiguity

The proposed dual polarized MIMO channel sounder is advantageous compared to other switch-based sounders since it captures both polarization signals at the same time. So, any changes in the environment that affects response of one polarization is reflected in the other polarization response as well. Figure 5-5 compares our proposed solution advantages over conventional switch-based channel sounders in which switching delay creates additional time when H polarization response for example should be measured after capturing the V response. In this case channel is “blind” and can’t see any changes if they happen.

Table 5-2: Design trade-offs and effective parameters.

Trade-offs	Action to improve	Consequences of the action
SNR dynamic range	Increase sequence length	1. Maximum measurable excess delay increase (pros) 2. Doppler range decreases under fixed chiprate (cons)
	Average more number of captured frames	Doppler range decreases under fixed chiprate (cons)
Ambiguity	Decrease sequence length	1. SNR dynamic range decreases (cons) 2. Maximum measurable excess delay decreases (cons)
	Increase chiprate (there might be hardware limitation)	1. Time resolution increase (pros) 2. Maximum measurable excess delay decreases (cons)
Time resolution	Increase chiprate(there might be hardware limitation)	3. Time resolution increase (pros) 4. Maximum measurable excess delay decreases (cons)

In any measurement, the assumption is that the response of the channel is stationary for the duration of time that the frame of the sounding sequence is being recorded. This is mainly because in order to avoid ambiguity at correlator output and reflects the meaningful relative response of channel MPCs with respect to each other, the channel should stay unchanged within the whole period which one frame of sounding signal is being captured. Therefore, Doppler range for our channel sounder will be limited by: 1)the sequence length (inverse relation) and 2)the chip rate (proportional relation). In our proposed channel sounder, the maximum sampling rate of the transmitter and receiver is limited to 50MS/s. So the fastest window of time which channel sounder can see the effects of any changes in the channel will depend on LS sequence length and will be equal to

$$Doppler\ range = L/50e6.$$

E.g., for a 511-bit sequence, it results in 10.22us and so on.

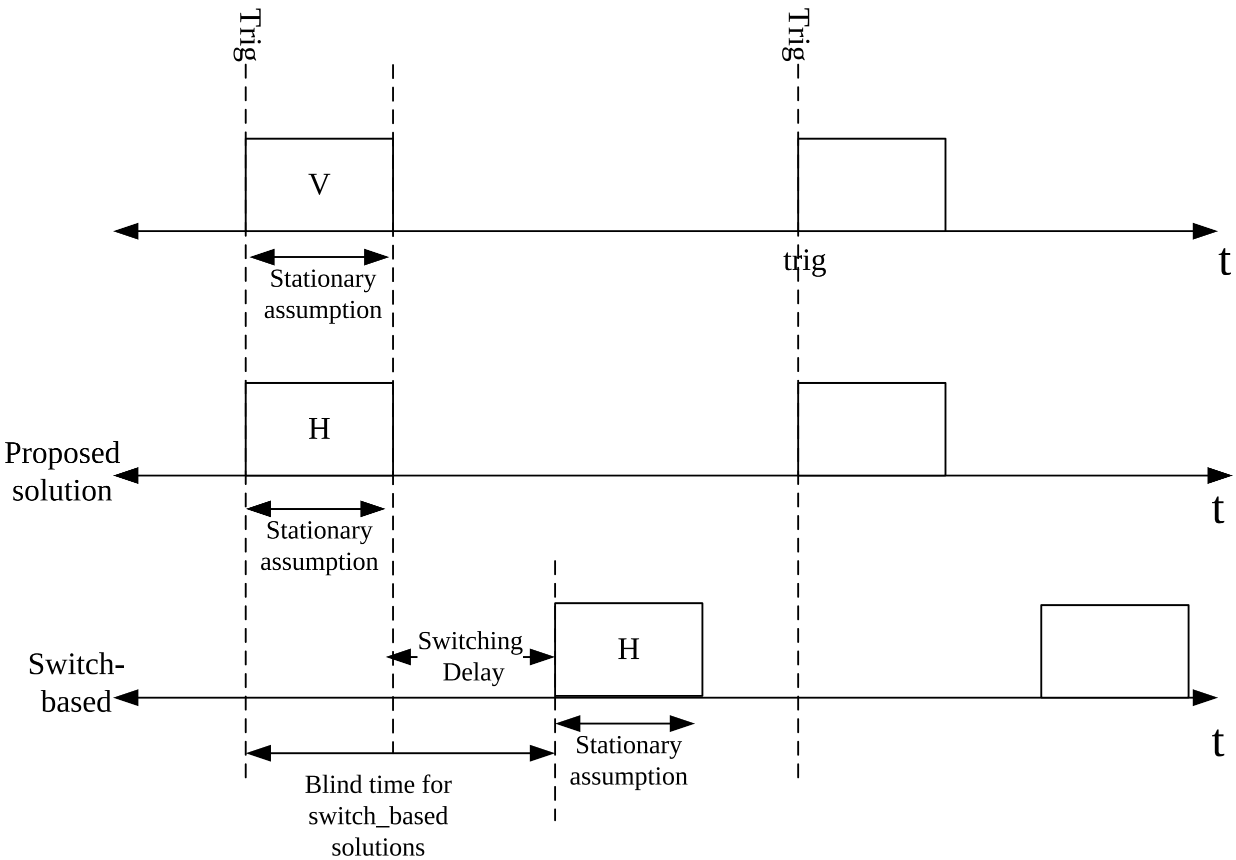

Figure 5-5: Ambiguity comparison between proposed solution and conventional switch-based channel sounders.

5.2.3 Phase Noise Analysis

The phase noise properties of some commercial switched-based MIMO channel sounders were previously analyzed [90], [143], [144]. It was shown that phase noise can lead up to 100% error in capacity estimation in the MIMO channels with high SNRs [136]. The other effects of phase noise are mainly the spreading of the signal in Doppler domain limiting the Doppler frequency resolution and dynamic range in mobile radio channel measurements [143]. Because of the importance of this metrics, in this section we analyze the responses obtained from direct and delayed paths for the added phase noise. Ideally the phase noise of the system should be zero. But in practice system imperfections such as time variation of the frequencies of the local oscillators (LO) at TX or RX, and in our case using an active element such as delay line system, can generate small variations on the phase, *i.e.*, phase noises.

The Allan variance was first introduced in [145] to characterize the frequency stability of local oscillators in time domain. Since then it has been used as a metrics for assessing phase noise of the MIMO channel sounders [141], [144], [146]. In our work we use the Allan variance as an additional criterion to assess the property of the phase noise sequence over different time scales and is obtained from the phase noise sequence of the recorded data.

The difference between phase noise variances of different channel will impact their Allan Variance values in different times of measurement within one trigger. It is defined as [147]

$$\sigma_y^2(\tau) = E[\frac{(\bar{y}_{k+1} - \bar{y}_k)^2}{2}] \, , \tag{5.7}$$

where $E[.]$ is expectation operator, and

$$\bar{y}_k = \frac{1}{\tau}\int_{t_k}^{t_{k+\tau}} y(t)dt = \frac{\varphi(t_k + \tau) - \varphi(t_k)}{2\pi f_c \tau} \, , \tag{5.8}$$

where $\varphi(t_k)$ is the phase sample at time instant t_k. Then (5.7) becomes

$$\sigma_y^2(\tau) = \frac{1}{K}\sum_{k=1}^{K} \frac{(\varphi(t_{k+2}) - 2\varphi(t_{k+1}) + \varphi(t_k))^2}{2(2\pi f_c \tau)^2} \, , \tag{5.9}$$

where K is the number of time measurements within a trigger signal spaced by $\boldsymbol{\tau}$. In the results section of this chapter we will obtain and compare the phase noise variations and Allan variances for both direct and delayed path of our channel sounder with other existing ones.

5.3 Implementation

In this section, we will describe the specific design parameter choices for both transmitter and receiver design following by our system error model and the calibration procedure for the proposed channel sounder.

5.3.1 Settings and Design Parameter Choices

On the transmitter side, the design is mainly concerned with selection of sequence type, length and sampling rate whereas at the receiver side, fibre length is the concern and as stated before, they all are forced by maximum excess delay of the environment. In this section, without loss of generality, we assume an environment with maximum excess delay of 2.27µs to carry on with the rest of design steps. According to the design equations we developed in previous section, this corresponds to minimum LS sequence length of 1022-bit giving the maximum chiprate of our receiver PXA 50MS/s. We had fibre delay line with relative permittivity of 2.9 in the lab, which from the developed design equation the minimum required fibre delay line length to create 2.27μs delay will be 400 m. The transmitter is configured to send continuously and is set to 'trig and restart mode' to synchronize the start of the transmission at every trigger signal. In order to study synchronization of the RX-TX and phase noise of the received frame in several consecutive measurements, we record 14 frames of LS sequences at each trigger. This can be helpful if one wants to improve SNR performance by averaging the 14 frames at receiving (suitable if Doppler range is not a constraint, *i.e.*, static or quasi-static channels), otherwise, each of the recorded frames will represent the channel by itself without using the averaging (suitable when dynamic of the channel is high).

Table 5-3 summarizes the designed parameters.

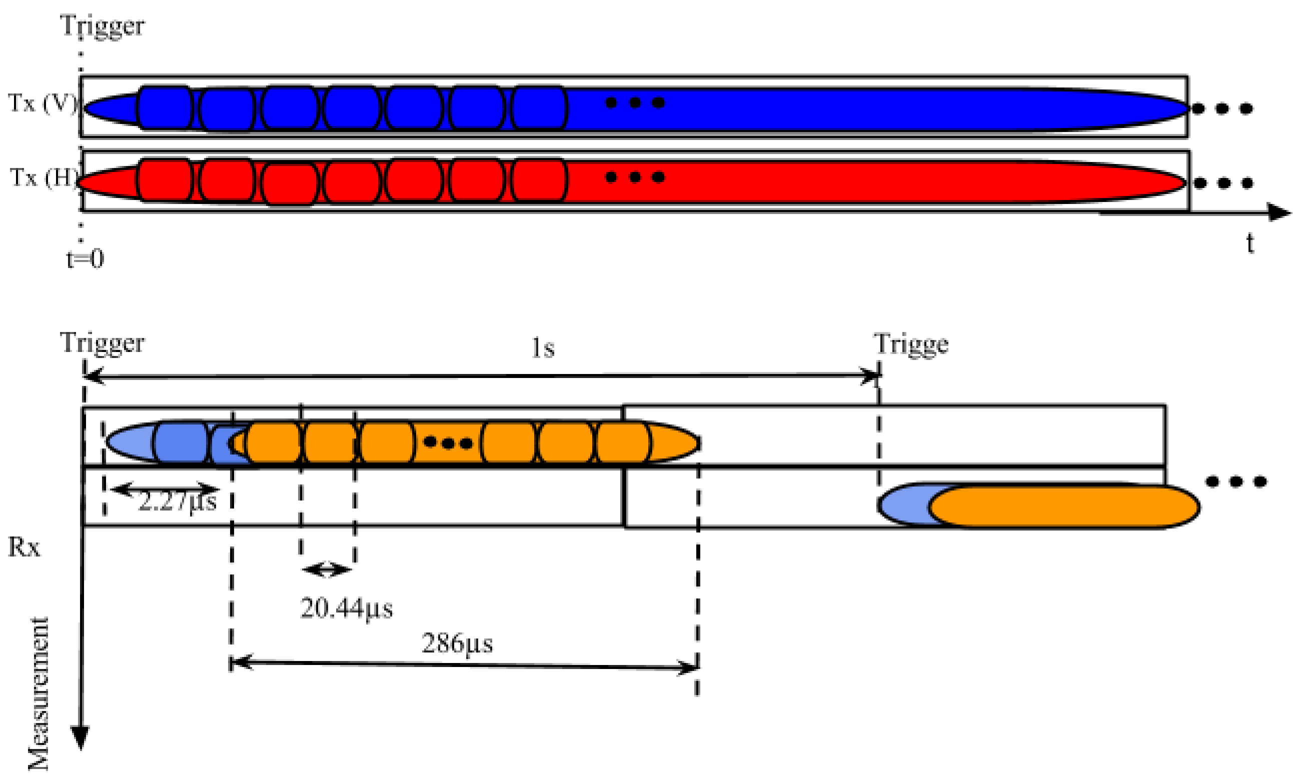

Figure 5-6: Relative timing of the transmitted and received frames.

Table 5-3: Channel sounder design parameter description.

L_S	Length of the sequence(bits)	1022
T_c	chip rate (Mbit/s)	50
T_S	Time resolution (ns)	20
T_D	Delay due to fibre delay line (µs)	2.27
τ_{max}	Environment maximum excess delay (µs)	2.27
N_f	Number of frames captured within each trigger	14
ε	Delay line dielectric relative permittivity	1.89

5.3.2 System Error Model, Calibration and Correction

The calibration of the MIMO 2×2 single-port delay-line channel sounder is simpler than switch-based sounders in which there should be several steps follow to calibrate switching synchronization at TX and RX [90]. In our channel sounder there are some sources of signal distortion due to non-ideal channel sounder hardware and needs to be identified and accounted for when recording the measurement data. The main error sources are due to lack of synchronization between the TX and RX local oscillators, unequal signal attenuation when passing through each path (direct vs. delay line path), crosstalk due to non-ideal transmitter, and antennas effect. The following describes details of calibration procedure that should be followed. Figure 5-7 shows the back-to-back connection of TX and RX for calibration purposes.

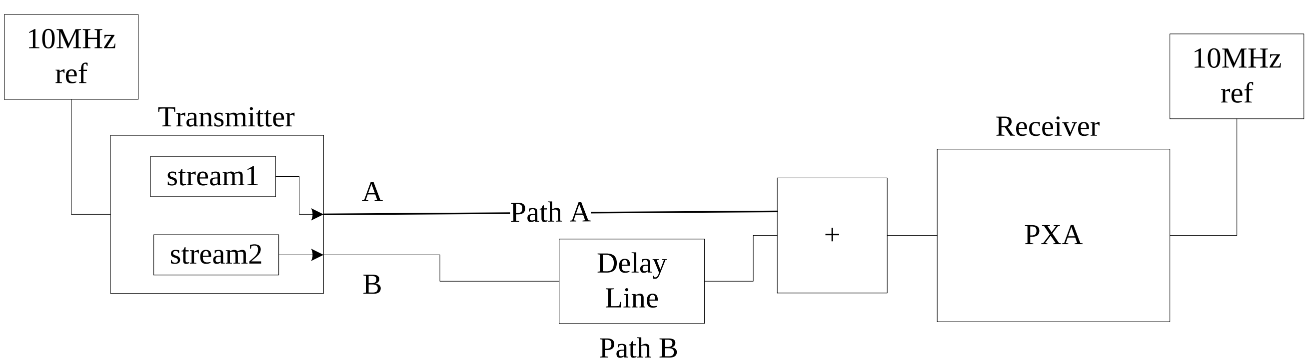

Figure 5-7: Back-to-back connection of the transmitter and receiver for calibration.

LOs synchronization: Both the transmitter and receiver should be synchronized with either a common 10-MHz reference their own LO clock signal which is synced to an external rubidium frequency. In the case of separate references, the offset between oscillators can drift the peak of the IR in the different rounds of measurements and result in inaccurate absolute delay estimation of the environment. Prior to the day of measurement, with a back to back measurement, the amount of drift between transmitted signal on path A and correlation output is obtained and is corrected in the post processing of the measurement data later. One round of such calibration is usually enough for doing the measurements in the same day unless the offset between LOs are such large that it creates noticeable drift of IR peak within short period of time or in consecutive measurements. Then this calibration should be repeated more often during the measurement campaign or proper action should take place to fix the synchronization of the LOs.

Balancing dynamic ranges of separate paths: This step is to equalize the attenuation of the V-polarized and H-polarized paths when they are connected back to back. One path may have more gain due to use of delay line system. While LS_1 and LS_2 are independently transmitted from channel A and B, respectively, a single capture should run and correlation DR using LS_1 and LS_2 sequences on each of the corresponding channels should be obtained. Then enough attenuation should be added to the channel which gives larger correlation DR so that both channels result in an equal DR. This can also be done by varying the transmitter output power if operator has control of it. In our case the output power of the SMW transmitter for each channel could be adjusted separately.

Absolute received power correction: This step is to adjust the correlation output power level so that its peak matches to the output power of the transmitter when one channel is transmitting and the other one is off (one channel is turned off to avoid cross talk effects if there are any) repeating for both channels. This step in fact accounts for path attenuation of the measurement setup excluding the antennas and environment.

Cross-talk correction between the channels: Ideally there should be no cross talk between the channel A and B when there is a back to back connection since they do not share any hardware prior to being combined at PXA input. However, due to non-ideal transmitter some signals can cross talk between the paths. This needs to be quantified and taken into account in the post processing of data. To characterize crosstalk between the paths, LS_1 and LS_2 sequences should be transmitted from channel A and B, respectively. after correlation, the amplitude of the

LS_2 presented with same delay of the LS_1 amplitude will be interpreted as the delay domain vector of cross talk from path A to B and vice versa. In post processing, these vectors should be de-convolved from the measured CIR.

Antennas calibration: This procedure is common for all the channel sounders and usually requires complex antenna beam pattern measurement in order to calibrate them out from measured data. In practice the finite cross-polarization between the antenna port can distort the signal and this can be mitigated using an antenna with better cross polarization response.

5.4 Channel Sounder Performance

In order to prove the concept, verify the above-mentioned calibration procedure in practice and evaluate the performance and limitation of the channel sounder, we conducted several back-to-back measurements where the TX and RX were connected as shown in Figure 5-8. We verified and quantified the inter-snapshot synchronization, channel sounder sensitivity, dynamic range, Doppler range and non-idealities such as phase noise. Moreover, the effects of the fibre delay line on overall noise floor of the system and phase noise degradation were investigated and compared to the case when just a direct path is used.

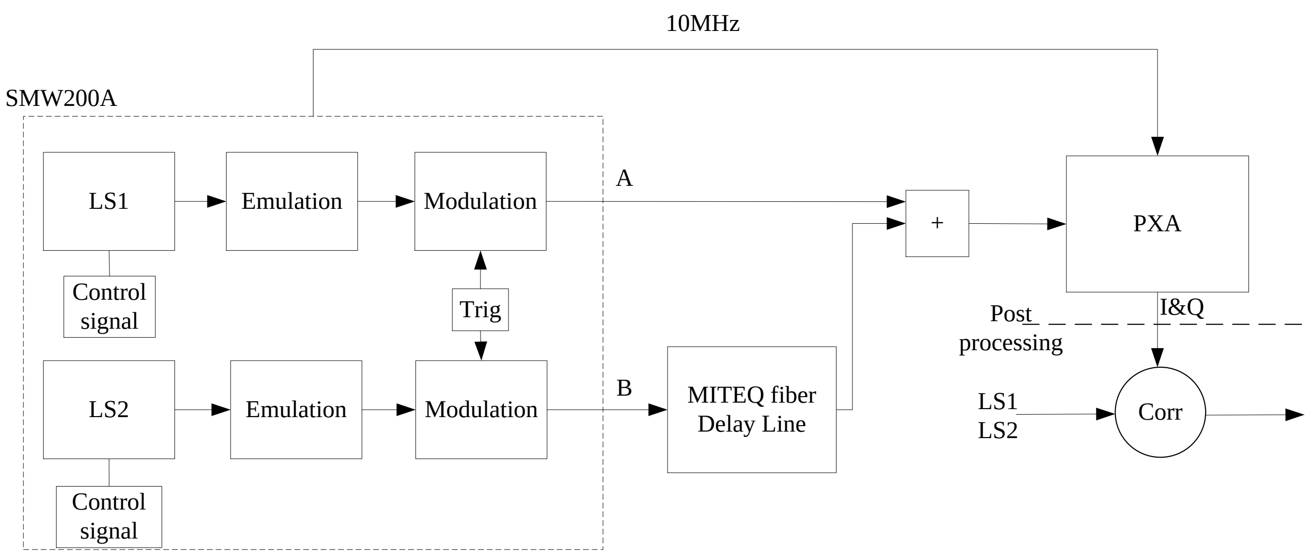

Figure 5-8: Bench top demonstration setup.

5.4.1 Proof of Concept

In this section, the goal is the proof of the proposed concept by showing the amount of fixed delay one can create using fibre delay line, possibility of recording two channel responses within a single snapshot and ability to distinguish them. Each of the channels A and B were already loaded with baseband LS_1 and LS_2 sequences length of 1022-bit using the modulation method described in the measurement section of Chapter 4. Calibration procedure was followed to balance path A and B while system was connected in back-to-back configuration. With the output power of transmitter set to -30 dBm on each port (this value is used to set the peak of the correlator output), the dynamic range of path B was measured 5 dB higher than path A which we compensated with lowering the output power of path B down to -35 dBm. Figure 5-9 shows the unbalanced responses at correlator output.

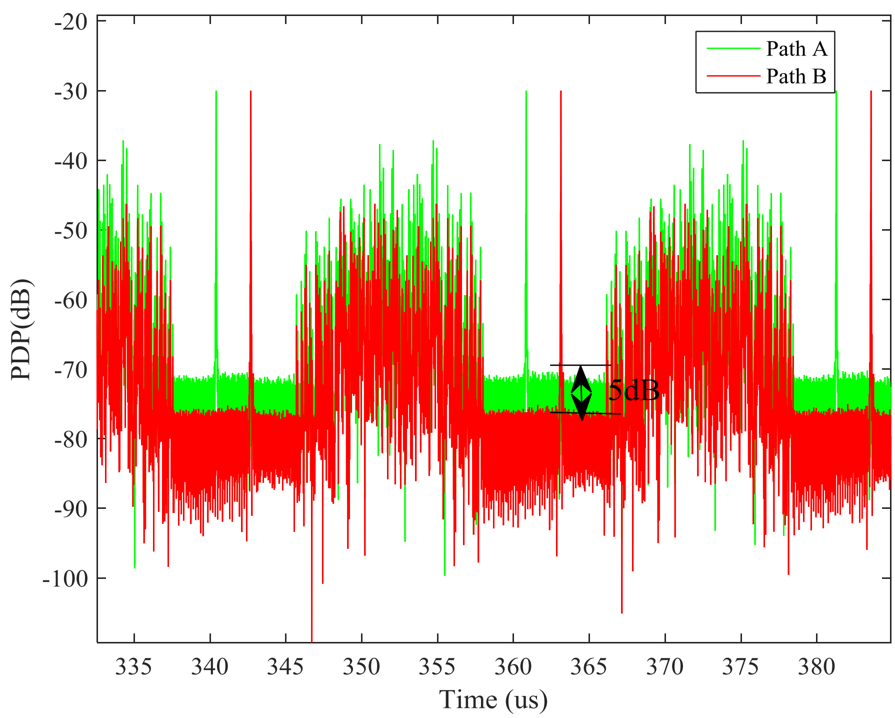

Figure 5-9: Before calibration, non-equal DR on each channel.

The 10 MHz reference signal and 1 PPS generated by the Rubidium frequency standard and GPS receiver, respectively, were connected with coaxial cables to the TX and RX and made complete synchronization of LOs such that the position of the first peak was remained fixed between the measurements and compensation after post processing wasn't required. In order to investigate the crosstalk issue due to transmitter non-idealities if existed any, we recorded the correlation output by transmitting LS_1 and LS_2 sequences of 1022 lengths. Similar figures to Figure 5-9 were produced and as it is seen, there is no cross talk between the channels. It is observed that the 2.27 μs delay because of the 400-m fibre delay line remains fixed between the measurements. Considering this time-invariant intentional delay and use of orthogonal LS sequences which provides negligible cross correlation at the output of correlator, this channel sounder makes a suitable setup to capture both polarization channel responses without interfering with each other.

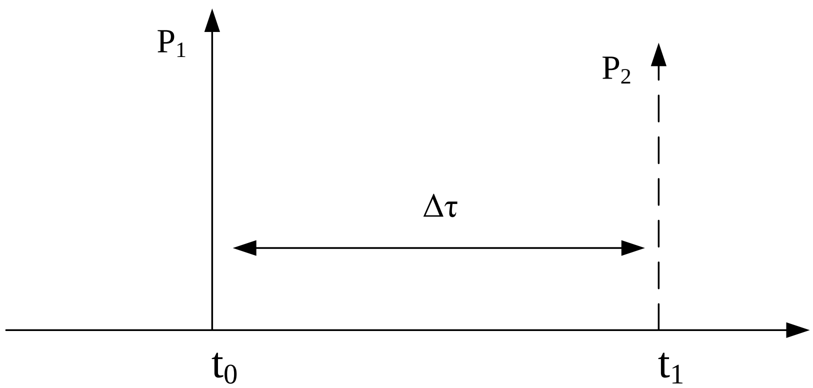

Figure 5-10: The moving propagation tap model.

5.4.2 Doppler Range Performance

Here we show the ability of the channel sounder to capture response of fast varying channels in a controlled manner using the above-mentioned setup on a bench. SMW200A has independent internal baseband fading (channel emulator) for each path. The fading simulator functionality simulates real-time fading effects on the baseband signal. Provided the instrument is equipped with the required options, up to 20 dynamic fading taps in both SISO and MIMO mode can be created simultaneously. In this section, we get advantage of this capability to create a multipath fading channel with specific number of tabs. In this section, without the loss of generality, we set channel emulator for path B as two-tap fixed standard multipath fading channel with separation between taps of 1 us and second tap 10 dB below the first tap's power. Using the R&S SMW-K71 option which comprises the 3GPP dynamic fading configurations moving propagation and birth-death propagation we set path A of the emulator to create *moving propagation* scenario. The moving propagation model exist in 3GPP TS25.104 and TS36.141 documents [148] and is chosen here to create dynamic environment scenario to test the channel sounder.

As shown in Figure 5-10 this model has two tabs: one static, tab1, and the other one moving, tab2. The time difference between the two taps is defined as

$$\Delta\tau = \mathrm{B} + \frac{A}{2}(1 + \sin(\Delta\omega \cdot \mathrm{t})) \tag{5.10}$$

where *A* in second is the maximum variation (peak-to peak) of tab2 around a point on the axis with distance of *B* seconds from tab1, and variation frequency of $\Delta\omega$. The parameters of the model were selected such that they create the fastest tap movement instrument could generate. A=1.5 µs, B=10 s was selected and second tap was set 10 dB below the first tap amplitude. 15 frames of LS sequences were recorded within each trigger. The raw IQ data then was correlated with original LS sequences. Figure 5-11 shows the normalized output of the correlator for one triggered measurement. Because of calibration, both channels dynamic ranges are the same.

The fastest variation (frequency of moving tap variation) is limited by the SMW to 0.1Hz. Although this is not fast enough to represent itself in the consecutive measurements within each trigger (As indicated in the Figure 5-11), it changes the tap location noticeably between the triggered measurements (in 1 s apart). Figure 5-12 shows a sample of CIR at correlation output. As expected, delay line created a fixed 2.27 µs between the channel responses. We observed the index of the peaks didn't have any drift due to good synchronization between the TX and RX. Both channels had 2 taps at the output which second tap of the channel B was fixed in all the measured data as a reference to assure synchronization whereas for channel A it was varying. In Figure 5-13 we plotted this tap's location in delay domain for different measurements of 1 second apart. It is observed that the tap follows the channel changes perfectly in time, sinusoidal with the same frequency and maximum variation of the 'moving propagation' channel settings we set at the beginning. As mentioned before, due to hardware limitation, we were limited to 0.1Hz tap variation. Same test is advised as future work using faster variant tap to characterize capability of the channel sounder. Theoretically, using a 1022-bit of LS sequence and sampling rate of 50MS/s, we are limited to capture a channel that varies with minimum duration of 20.44µs. This can be improved using equipment with larger sampling rates and/or shorter sequence length.

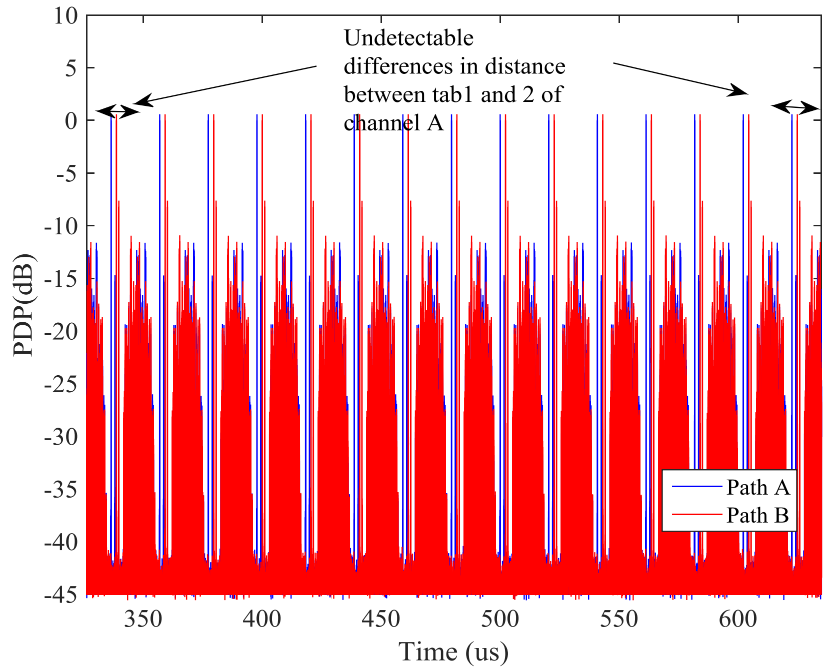

Figure 5-11: 15 frames of both channels captured within each trigger.

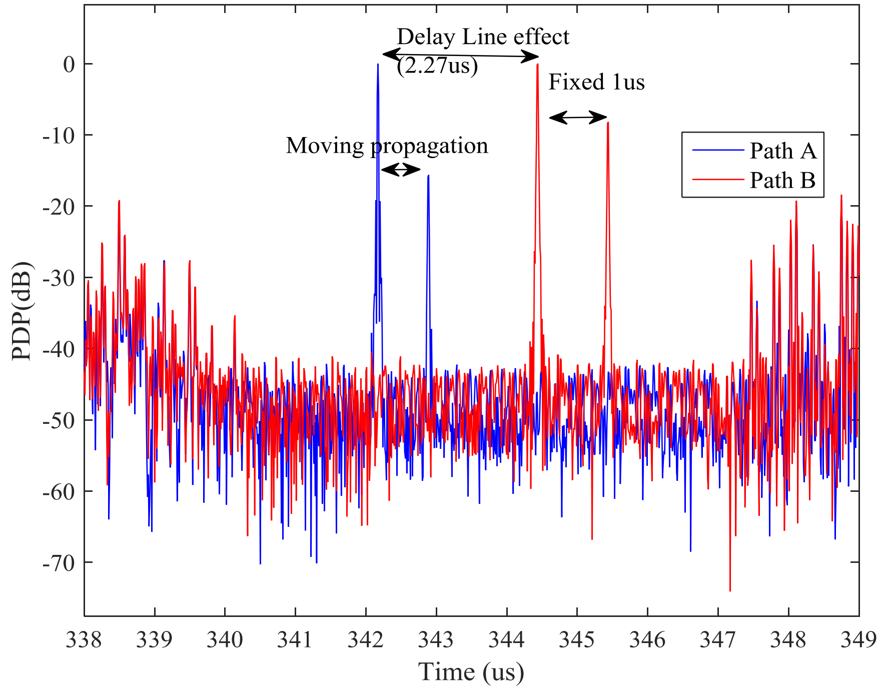

Figure 5-12: Single snapshot of fixed and moving propagation.

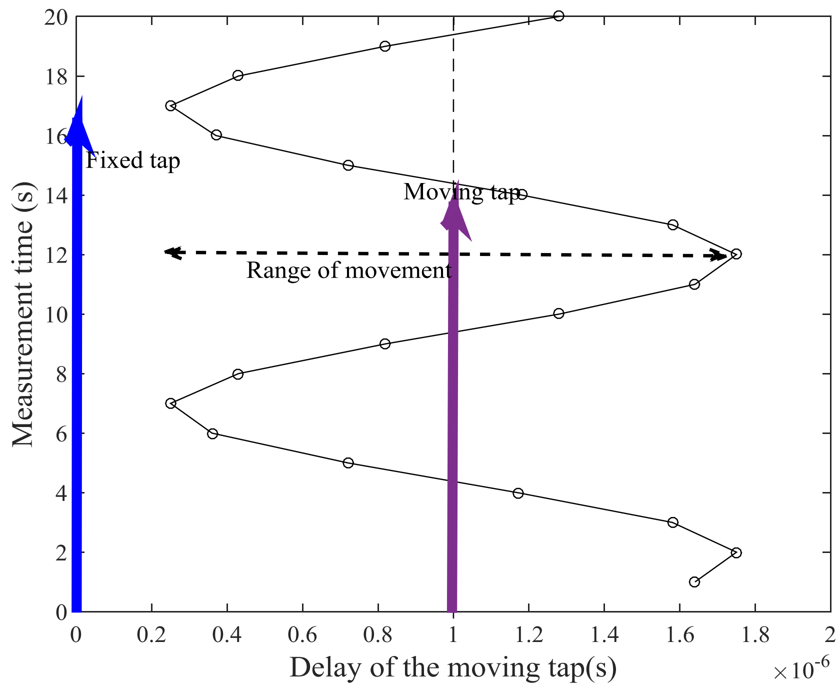

Figure 5-13: Demonstration of moving tap location in the delay domain during several measurements

5.4.3 Effect of the Delay Line on the Noise Floor

We are using 400 meters of fibre delay line with MITEQ SCM fibre optic transmitter [149]. Delay line is an active device and it will increase the noise floor of the entire system since it operates in parallel to direct path (path A in Figure 5-8). In order to measure the amount noise floor increase due to use of delay line and compare it to the case when delay line is not used, we did 4 measurements. In the first one we terminated input port of the PXA and measured the noise floor value (Figure 5-14(a)). This will be the noise floor limitation induced by the recording device (*i.e.*, PXA). The next noise floor read was taken when just path A is connected and the other end was terminated with a 50-ohm load (Figure 5-14(b)). In this case the noise floor will i increase compared to previous measurements due to the use of direct cable. Same measurement was repeated when delay line was connected (Figure 5-14(c)) to obtain noise floor just due to use of delay line. At the end, we connected both paths to the PXA using combiner and splitter and terminated the other end (Figure 5-14(d)). Table 5-4 shows the results for this measurement.

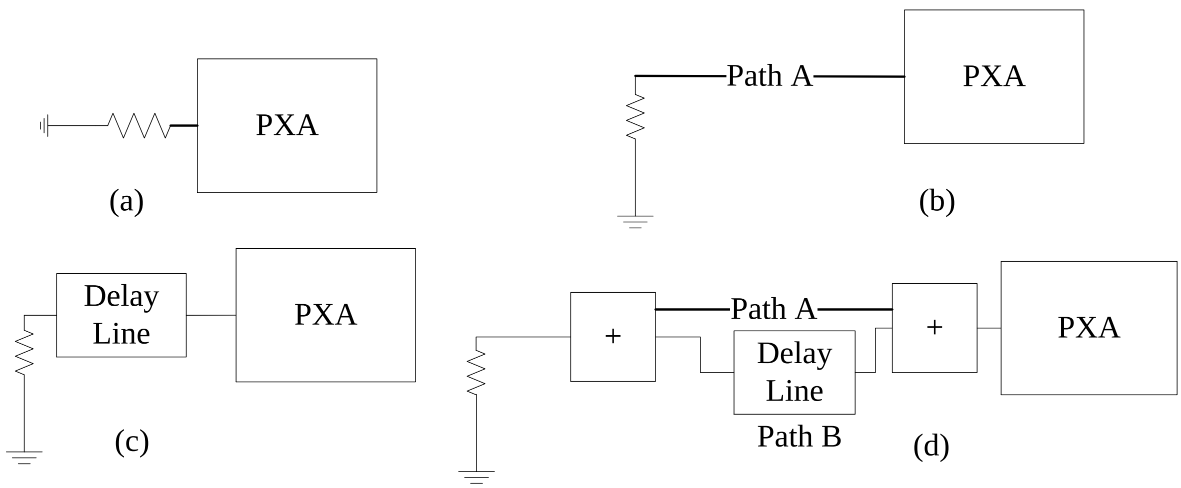

Figure 5-14: Measurement setup for noise floor measurement of different channel sounder paths.

Table 5-4: .Measured noise floor increase due to different paths.

Measurement	PXA	Path A	Path B	Path A+B
Averaged Noise floor level (dBm)	-97.6	-97.7	-91.9	-91.6

It is observed that variation of noise floor due to path A is negligible while delay line degrades it around 5.7 dB. Since the gain of the delay line system was measured 4 dB, the noise figure for delay line system will be 1.7 dB. However, the minor increase in noise floor of the system due to use of active delay line system is ignorable since the correlation self-noise as was shown is higher and will be dominant. Consequently, the SNR dynamic range of the system is determined by the DR of the LS sequences in the noisy channel that we analyzed in previous chapter.

5.4.4 Combined Effect of Phase Noise and Delay Line

Using the setup of the back-to-back connection and recording the IR of both paths (HH and VV), the phase samples were obtained from the peak values of IRs. Using the 20 kHz frequency bin sizes, we collected 1950 samples within one snapshot for each of the paths. The demeaned phases from back-to-back measurements within one snapshot for each of the channel were obtained and their distributions are plotted in the Figure 5-15 and Figure 5-16. It is seen that they fit to Gaussian distribution with zero mean and variance of 4.68 and 6 for direct and delay line path, respectively.

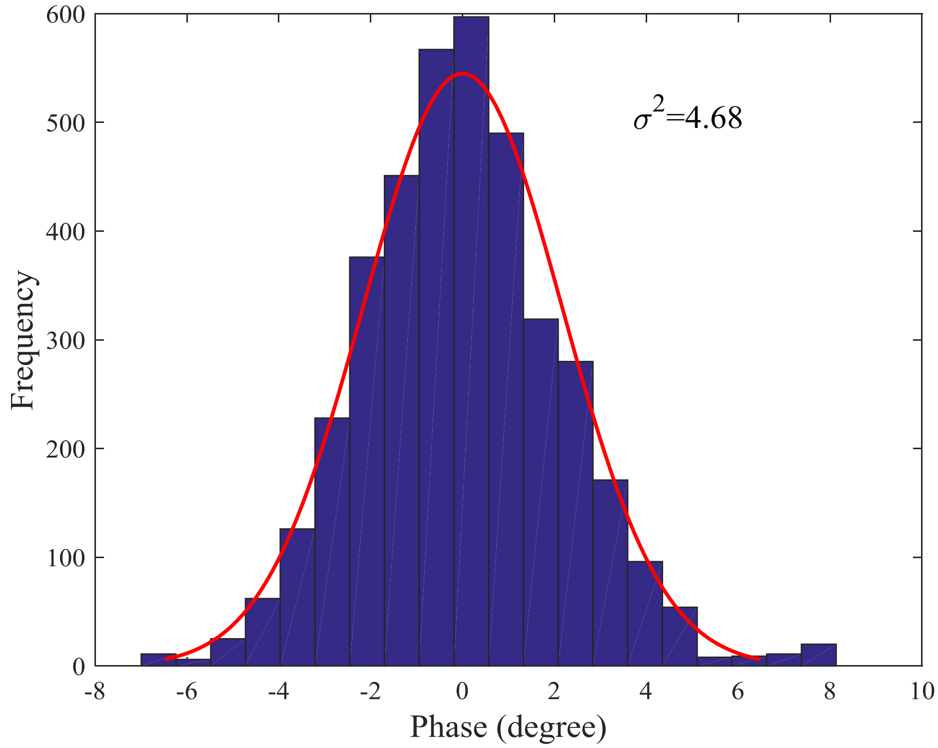

Figure 5-15: Direct path phase noise distribution

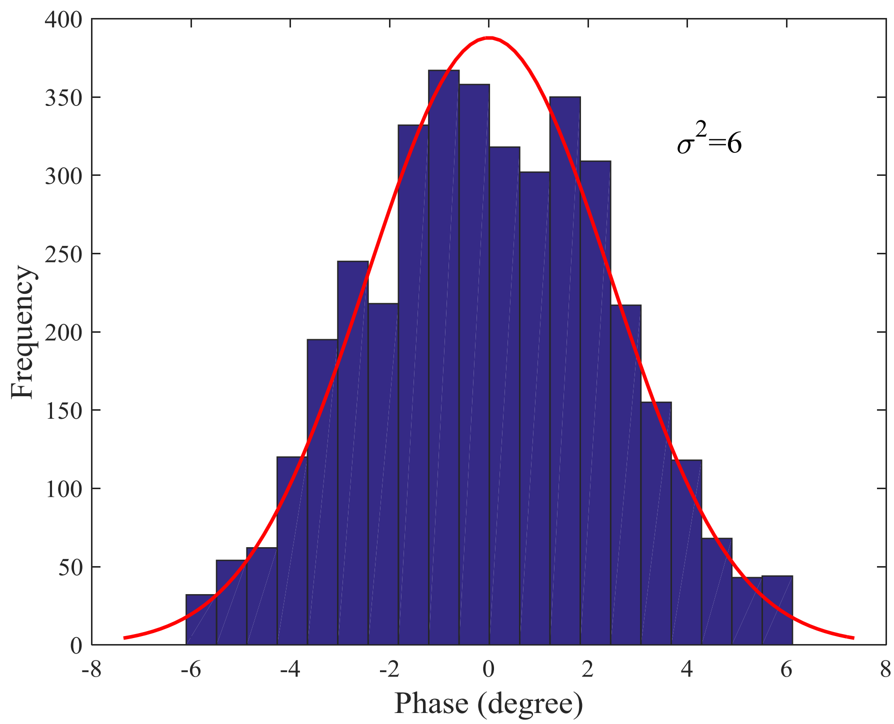

Figure 5-16: Delay line effect on phase noise distribution

Figure 5-17 compares both channels in 14 consecutive recorded frames at each trigger. The average standard deviation of phase noises for the direct channel is 1.36 degree larger than the path with delay line. Using (5.9) with K = 14 and τ=10.22 μs, the Allan variance of the recorded snapshots of direct and delay line paths are plotted in Figure 5-18. The Allan variance for both paths are sufficiently low compared to the other channel sounders in the literature [144], [146]. Beside, in [144] it was shown that phase noise will have negligible effect on channel parameters such as capacity estimation if Allan deviation at 1s is less than 10^{-10}. It was seen that using Rubidium reference clock we could easily fulfill this condition.

5.4.5 Expansion for Higher Order MIMO

Expanding the current 2×2 channel sounder to measure more number of MIMO schemes will need long length of fibre optic links to properly delay each channel. The required length of fibre can be reduced to a reasonable length by strategy of using the spools of the fibre multiple times as described in Figure 5-19.

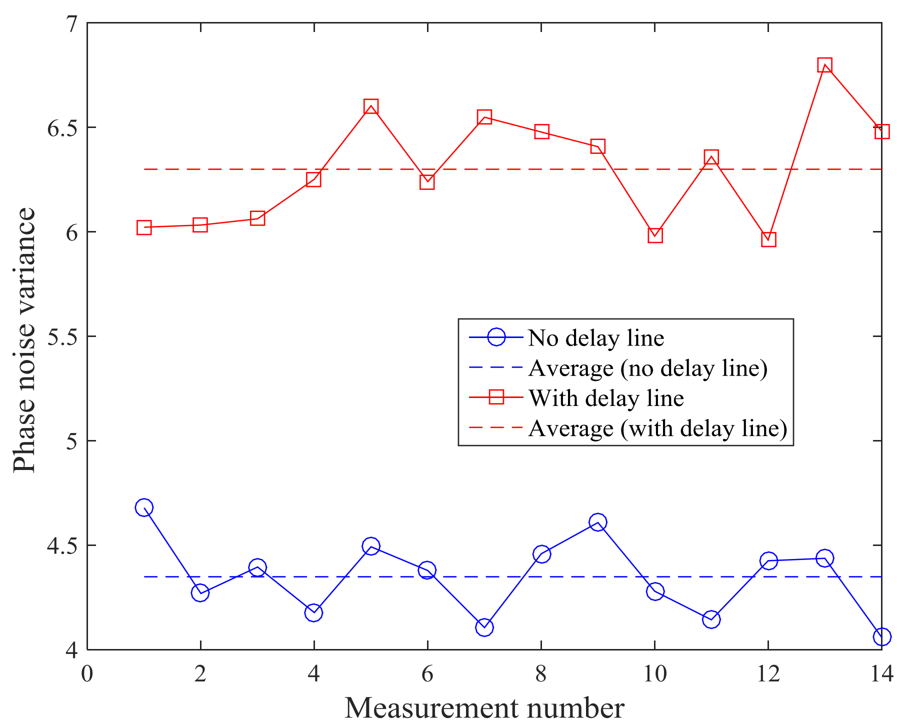

Figure 5-17: Average variance of the phase noise of consecutive records for direct channel and delayed-path.

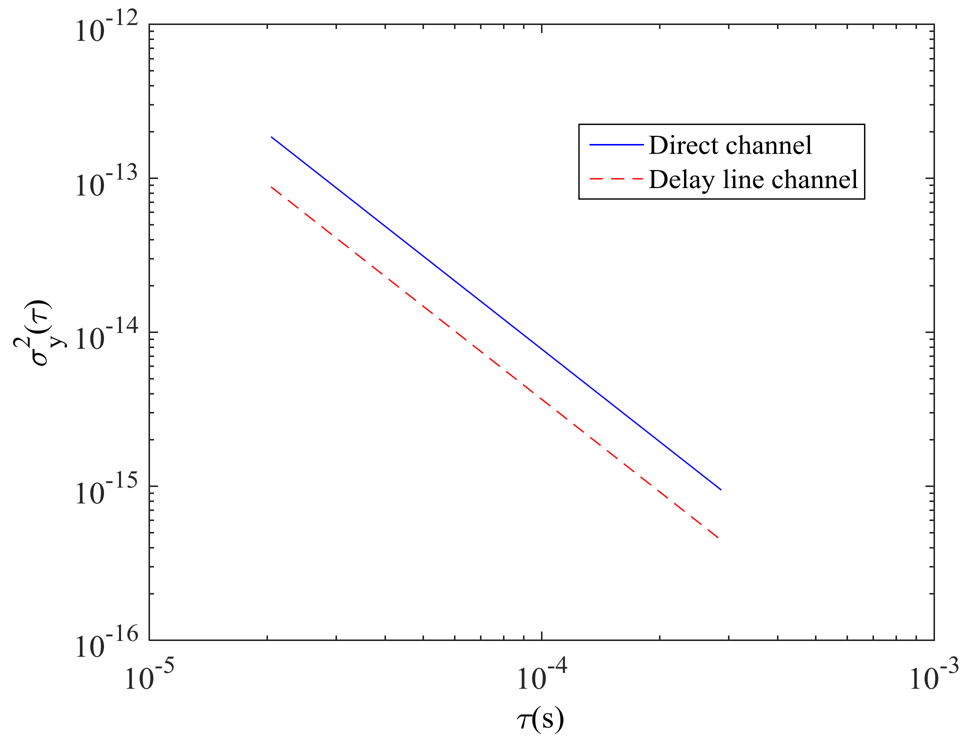

Figure 5-18: Allan variance of the direct and delay line path with in one snapshot.

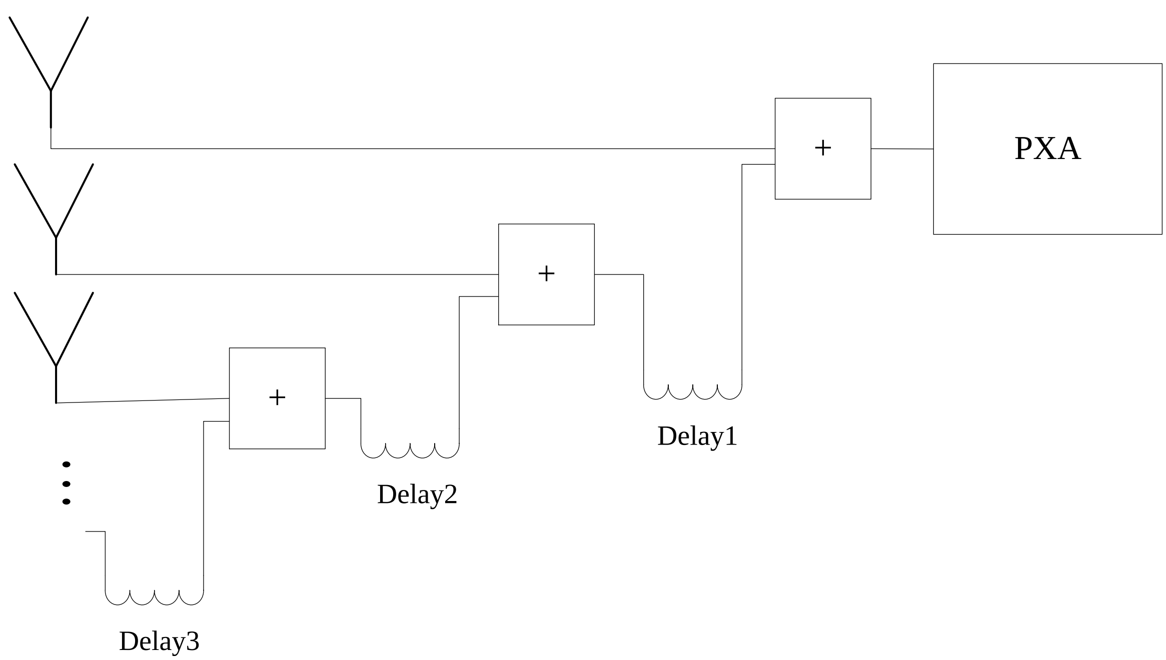

Figure 5-19: Proposed method of using fibre delay line efficiently to expand delayed-line channel sounder.

It should be noted that if the number of MIMO increases, the restriction on IFW length which LS sequences provides becomes more stringent since all the responses of the antennas should be accommodated within that zone without interfering with each other. Moreover, due to use of multi-channel fibre delay line hub system to implement this configuration, cross talk can rise between the channels and needs to be carefully studied and accounted for when doing measurement.

5.5 Discussion

Many options exist for measuring the static and semi-static MIMO channels but few exists for measuring dynamic channels. However, the conventional channel sounders that connect single channel transmitters and receivers to individual transmitting and receiving antennas in turn via switches are unable to accurately capture channel responses. On the other hand, more sophisticated MIMO channel sounders that employ spread spectrum transmitters and receivers with multiple channels that are each connected to dedicated antennas allow all possible transmit and receive antenna combinations to be characterized simultaneously and therefore obtain accurate fading correlation estimates but at considerable added expense.

In order to overcome the previous works limitation in measuring MIMO channel responses in such environments where limited by many factors such as: cost, accuracy in non-stationary channel estimates, and long duration of measurements, we propose an alternative solution in which the Loosely Synchronized coded transmissions is combined with our proposed new technique for using fibre delay lines to replace multi-channel receivers with a single channel receiver and effectively characterize multiple receiving antennas simultaneously. This allows the responses from the array of receiving antennas to be stacked in time and observed with a much less expensive single channel correlation-based receiver. Beside, use of orthogonal LS sequences makes the channel sounder more fast and more accurate because of simultaneous measurements.

In this chapter, we demonstrated the concept on a bench-top measurement setup. We also revealed the design formulas that determine the required channel sounding sequences and fibre delay line length mainly based on the environment maximum excess delay. System error model was created to develop the calibration procedure mainly included the synchronization between the TX and RX, equalizing the different paths of the receiver (direct and delay-line) in terms of link budget and crosstalk effect, and antenna effects. The design trade-offs also were discussed.

It was shown that channel sounder dynamic range mainly depends on sequence lengths such that longer sequences will result in larger dynamic range but will degrade the ambiguity of the channel sounder, *i.e.*, the Doppler range. On the other hand Doppler range of our channel sounder is limited to the sequence length and can be improved using shorter sequences or higher sampling rates. The decision that which one is more important (larger dynamic range or Doppler range) mainly depends on the type of the environment in which measurements are being taken.

Performance of the proposed channel sounder was evaluated in terms of system dynamic range, Doppler range, and effects of delay line on measurement noise floor and phase noise. We concluded that dynamic range of the channel sounder is limited to the LS sequence dynamic range in presence of noise (Chapter 4). A moving propagation channel model was implemented to study Doppler range performance. It was observed that channel sounder could capture the variation of the dynamic channel precisely. The ultimate limit for Doppler range of the channel sounder was shown to be proportional to sequence length and TX/RX chiprate. Using the active fibre delay line system can increase measurement noise floor of the system and induce phase noise to the measured channel. Our measurement results showed that there was less than 6 dB increase in the noise floor value when fibre delay line system is used compared to a channel sounder with just direct path. However, it is ignorable when considering the self-noise due to correlation of the LS sequences. Phase noise of the system was measured in a back-to-back connection and effect of delay line system on it was studied by Allan variance metrics. It was shown that Allan variance of the direct and delay line paths were both adequately low compared to commercial switch-based channel sounders, therefore estimation of MIMO channel parameter such as capacity will not be affected by that. At the end an efficient method of using fibre delay line to expand the channel sounder for higher number of MIMO schemes was also proposed.

In this chapter, the LS sequences were used which are low energy due to insertion of several zeros values in the Golay sequences in the generation procedure. More energy efficient sequences can be used in the proposed channel sounder such as frequency-orthogonal pseudo noise (FOPN) sequences to improve the dynamic range and Doppler range performances. With the existing available hardware, we could generate a moving propagation scenario to replicate a dynamic environment and examine how well channel sounder can capture the environment changes, however the speed of the changes may not be fast enough for perfect reliability test. So, further measurements are required in the very fast varying simulated channels in order to proof the accuracy of the proposed channel sounder in capturing successive polarization responses. Some channel emulator features like dynamic environment emulation (DEE) can be used to create a varying channel in a controlled manner. In our study we used a two-port R&S SMW200A signal generator to implement the channel sounder for proof of concept. However, Universal Software Radio Peripheral (USRP) along with GNU radio driver in MIMO configuration can be utilized instead in transmitter side in order to reduce the cost.

In summary, the proposed channel sounder seems to be a very suitable for 2×2 dual polarized MIMO channel sounding. It is scalable to larger number of MIMO branches at RX side but it will be increasingly expensive and further studies will be required for the limited interference free window size issue associated with larger number of snapshot captures and cross talk between the branches.

Chapter 6:
Effect of Terminal Height on Shadow Fading in Suburban Macrocell Environments

6.1 Introduction

In this section, we overview the previous works and their limitation, focusing on the studies related to effect of terminal station (TS) antenna height on communication systems parameters. Among those parameter, Shadow Fading (SF), as the topic of our study, is reviewed in more detail including previous works on factors influencing SF more specifically effects of terminal height on SF standard deviation.

6.1.1 Effect of Terminal Height on System Parameters

A whole series of new applications involve using pole-top terminal stations such as fixed wireless access for Smart Grid, intelligent transportation, advanced cellular radio system, such that studying the effect of TS height increase on system parameters has been gaining lots of attentions in recent years. The most recent works have been studying effects of terminal height on different system parameters such as mean path loss [26]–[28], [150]–[153], signal to interference and noise ratio (SINR) and network coverage [31], [154], data rate [155], delay spread [153], [156] and K-factor. [157]. In [26] the effect of terminal height on path loss component was studied by measurement up to 7 m terminal height in a region with 7.5 m mean building height. It was concluded that higher terminal antenna provide smaller path loss. Hien *et. al*. in [150] and [151] extended the work in [26] for higher TS heights for LTE relaying applications, up to 13 m and 25 m, respectively.

Based on the comparison of the measured data in urban macrocellular environment with already developed empirical models such as WINNER, they proposed a simple model to take TS height into account. Authors in [27] compared measured path loss data at different heights and showed 10-20 dB path loss reduction when receiver height is raised from 6 to 10 m. In a similar study, effect of TS height on path loss exponent was studied using measurement data in [153]. Later in [28] it was analytically studied using Geometrical Optic and Uniform Theory of Diffraction methods. Beside mean path loss, other system parameters also have been subject of studies. In [155] several deployment parameter effects in point-to-point and point-to-multi-point which were used for microwave backhauling of small-cells in a heterogeneous network, was studied including below the rooftop TS antenna height effect on data rate. In [153], [156], effect of TS antenna height on channel delay spread was studied by measurement. It was concluded that delay spread decreases with the increase in TS height.

As described, variation in path loss and other system parameters with terminal height in suburban environments is well characterized. However, there is lack of comments on behavior of shadowing with TS height. Moreover, most of the above-mentioned studies are limited to TS antenna height of below rooftop and the path loss prediction model is not supporting terminal height of above rooftop level. In most of the analytical calculations shadowing has been added as Lognormal distributed value to path loss data with a fixed standard deviation. This encourages us to review previous works on SF characterization and their limitations in the following section focusing on the effect of terminal height.

6.1.2 Effect of Terminal Height on Shadow Fading

Shadow fading has been extensively studied in past 40 years. Egli in 1950's first realized a Lognormal distribution for SF [158]. After then there has been enumerate contributions in studying different parameters affecting SF such as distance [159], [160], environment type [161], [162], Base Station (BS) antenna height [163] and frequency [164], [165]. Few, if any research has studied the effect of terminal height on SF above the rooftop. This is understandable since few use cases was involved with terminal antenna heights larger than 2 m. Most previous work, like those in wireless sensors area focused on the remote terminal heights between 1.5 and 2 metres [166]–[168]. However, they noticed of no significant change in SF variation with respect to terminal height.

In few previous channel propagation studies, people measured path loss and SF location variability for above the rooftop heights as well [28]–[30], [152]. In [152] authors compared between path loss measurement data at 9 m and 12 m and predicted the mean path loss using Random Building Height (RBH) analytical model. It was shown that since shadowing effect and foliage are neglected in their analytical model, prediction error is large and becomes larger in higher terminal heights. In [29], the temporal fading dynamic range of received signal was measured in different TS heights from 3 m to 9 m in an suburban environment with 8.5 m mean building height. They noticed that below rooftop level, due to multipath and quasi-stationary nature of channel the dynamic fading range was larger than above rooftop level and it was generally decreasing by increasing the height. However, the results are site specific and there was no analysis showing the effects of environment characteristics such as building height distribution on the results.

In [28], [30] shadow fading standard deviation was reported as one of the output data of measurement post processing results. However, the behavior of the SF with respect to terminal height was ignored and up to date there is no solid analytical model of SF with terminal height in the literatures. The importance of this topic has been emphasized recently in the work by Nasreddine *et. al.* [31] in which they concluded that a better understanding of the shadowing behavior at different terminal heights is a key requirement for the evaluation of wireless networks. This includes necessity of developing models for the standard deviation of the shadowing which they showed it can have significant impact on performance of the system they studied [31]. As a result, in the rest of this chapter we demonstrate how SF varies as a function of terminal height and building height distribution and the manner in which this affects the system link budget and coverage.

In the rest of this chapter, we will look in the SF behavior with terminal height in more details and mention the physical reasons behind it. Then, we will present the measurement data results that motivated us in the first place to look into the shadowing variation over terminal height effect with simulation approach. Then, we will explain the system and diffraction model we used for a typical suburban environment to simulate and study this effect followed by the results for depth of shadowing versus terminal height. As the distribution of the SF at mean building height is observed to less follow the lognormal distribution and better modelled with bimodal Gaussian, next we will model it with a mixture distribution and the parameters of mixture with respect to area's building height variation will be studied. The effect of SF variation on edge and area coverage will be studied next and the chapter will be concluded by highlighting the main results and recommended future work.

6.2 Concept and Problem Definition

In a propagation channel, the total attenuation of the signal amplitude can be described by the three-term multiplicative model as

$$L(x) = L_0(x)m(x)r(x) \, , \tag{6.1}$$

where x is distance parameter, $L_0(x)$ is path loss that depends mainly on the environment and the distance between the receiver and transmitter. $m(.)$ denotes the local average of the received signal level or shadowing and $r(.)$ is the small scale fading signal component. The latter has been shown to be well modelled with a Rayleigh distribution when no LOS component exists or by Ricean distribution otherwise, while for the former, in contrast, there is no widely accepted theory for its variation. Experimentally it has been proven that it can be well approximated by Lognormal distribution in wide variety of scenarios.

The conventional explanation of SF is the multiplicative model and the central limit theorem based on the assumption that cascade of random attenuating factors affecting the signal results in lognormal distribution. In a communication network, the performance of the system mainly depends on the strength of the received signal. More importantly the area and edge coverage, as we will show in the following, have direct dependency on it. In order to study the effects of terminal height on the system performance and link budget, all the above-mentioned signal components, *i.e.*, mean path loss and fading should be considered. As mentioned in previous section, variation of mean path loss, $L_0\ (.)$, with respect to terminal height is very well characterized in previous works. The summary is: As terminal height increases, mean path loss will decrease. Fast fading, $r(.)$, was studied in chapter two and three in great detail but is ignored in this chapter assuming it can be averaged out in any measured data set. Beside, its value is negligible compared to slow fading in the frequency of the interest. Therefore, only shadowing component of total propagation path loss will be considered in this chapter.

In [169], [170], the building height variation in Urban and Suburban environments was reported to be the main reason for lognormal variation in the mean path loss. Considering the possible heights, a terminal can have with respect to the ground and roof top, we categorize shadowing behavior into three main regions.

1. Non-Line-of-Sight (NLOS) Region: Includes the areas with terminal located well-below the rooftop. Since in SG fixed wireless systems BS is located above the rooftop for backhaul application, this category is considered NLOS. As discussed in previous section, most of the previous studies on effect of terminal height on SF have been focused in this region that noticed of no significant change on SF variation with respect to terminal height.

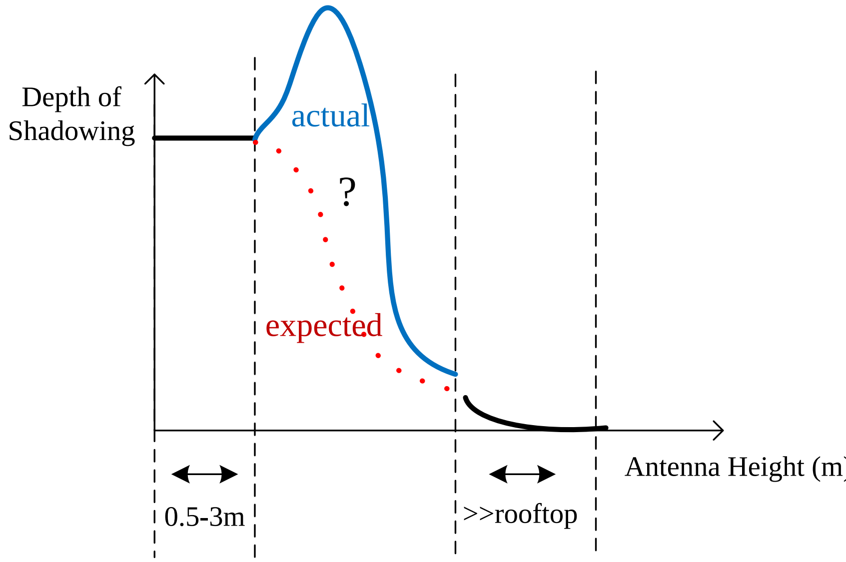

Figure 6-1: Expected vs. actual behavior of depth of Shadow Fading with respect to terminal height.

2. Line-of-Sight (LOS) Region: Includes the region with terminal located well above the rooftop. Again because the BS is also located above the roof top, this region is considered LOS. By intuition the shadowing is minimum in this region and tends to reach to zero when TX and RX are located in well above, *i.e.*, in pure LOS scenario.
3. Transition Region: Includes the heights around the rooftop. The expected behavior is that similar to mean path loss, SF will also decrease as terminal antennas height are raised. However, as we will show in the rest of this chapter, according to our measurement data in a typical suburban macrocell environment and the simulation of the similar environment, the behavior of SF within this region is different than expected. It rises as terminal height increases and has a peak in a certain height and passing that height it decreases. Figure 6-1 shows the approximate behavior of SF with respect to terminal height in different regions where both expected and actual behavior is plotted. We will show that the critical height that the shadowing peak happens at, corresponds to area's mean building height. In the rest of this section we will intuitively describe the reason for this behavior of SF with respect to terminal height

Statistically looking into transition region, a terminal can be either in LOS or NLOS situation with respect to its transmitter. As terminal height increases up to the mean building height, the mean path loss decreases since some links status change from NLOS to LOS. However, the rest of the links will still remain as NLOS. This black and white view toward the links' status justifies that shadowing will increase as terminal height increases within the transition region due to separation of LOS and NLOS points in the plane of path loss versus distance, therefore will create large differences between path loss points and the regression line (*i.e.*, larger standard deviation). Increasing the height, more of the NLOS links becomes LOS or semi-LOS causing the SF to drop. One may argue that there should be a separate analysis for LOS and NLOS links. This is valid argument if the goal was to design or analysis of few numbers of links such as those eras which legacy point to point communication links were designed in utility transmission line level communication. However, today the goal is to design and deploy a large number of communication links for a risk free performance in distribution level that requires a statistical analysis due to large number of endpoints and large geographic coverage area. This prevents links to be individually differentiated as LOS or NLOS and a general statistical analysis is required which includes both types of links.

According to our measurement campaign result which is described in detail in Appendix A, we observed the above-mentioned SF behavior in the measurement data of suburban environment. This motivated us to look into it with more rigorous simulation approach using general model of similar suburban environment as is described in the next section.

6.3 System Model for Macrocell Environment

Away from the high-rise core, the buildings in a city and its suburbs are of relatively uniform height, typically 2–4 stories. The street grids organize the buildings into rows that are nearly parallel. We are not looking for a very accurate model of buildings to model since our ultimate goal is to compare the variation of SF standard deviation in different terminal heights rather than finding ultimate accurate path loss. However, the model needs to be simple, general and capable of including the physical environment parameters of interest such as buildings random height and spacing variation. We use similar suburban graphical representation in [171] when building our simulation model since it satisfies above mentioned criteria as well as statistical parameters such as shadowing cross links correlation. The further assumptions we have made in our studied model are:

- A square area of RxR (m^2) is assumed without loss of generality and locations of the terminals are chosen randomly in a grid which building heights are following the Gaussian distribution [172].
- Considering the fact that in the Smart Grid macrocell deployments the BS is well-above the average rooftop level, the mean path loss then becomes a function of the average characteristics of the propagation link, mainly the obstacles height and separation [160], and the shadowing becomes a function of the variation in such characteristics. Therefore, we assume diffraction over the building rooftops as the main propagation mechanism and we ignore reflections and street canyon effects. This assumption is coherent with propagation mechanism in many environments [173], [174].
- Because shadowing decorrelation distance directly depends on the building separations within the simulation area [171], building separations are assumed to be a specific value, b, in our simulations in order to have control on the decorrelation distance corresponding to different suburban areas. The distance between the building blocks is assumed to be fixed because having exact screen separation is not critical when considering propagation over the rooftops [175]. More specifically it was shown previously that this parameter has no significant effect on the standard deviation of the shadow fading [28].
- Buildings are replaced with knife-edges which has been found appropriate for built-up areas [176], especially in macrocell environments. Besides, close to grazing angle the whole roof is not influencing the path loss and considering more complex scatterers such as rectangular cylinders instead of the knife-edge will unnecessarily increase the computational effort. Moreover, using a double knife-edge instead of the single one for individual building replacement as was discussed in [175], will not have considerable effect on path loss range dependence. In [177] other possible representations of the buildings were studied and was shown that at higher base station height, the difference between those representation and single knife edge is ignorable.
- We assume perfect absorber knife-edges since the frequency of operation is high enough to generate shorter wavelengths compared to dimensions of the buildings.

Figure 6-2 shows the 3D model of an RxR m^2 typical suburban region in which building heights are randomly generated and TSs are randomly selected within the grid. BS is assumed to be located in the middle of the grid. Figure 6-3 shows the equivalent 2D profile representation of each communication links between BS and each of the TS locations, representing buildings as knife edges.

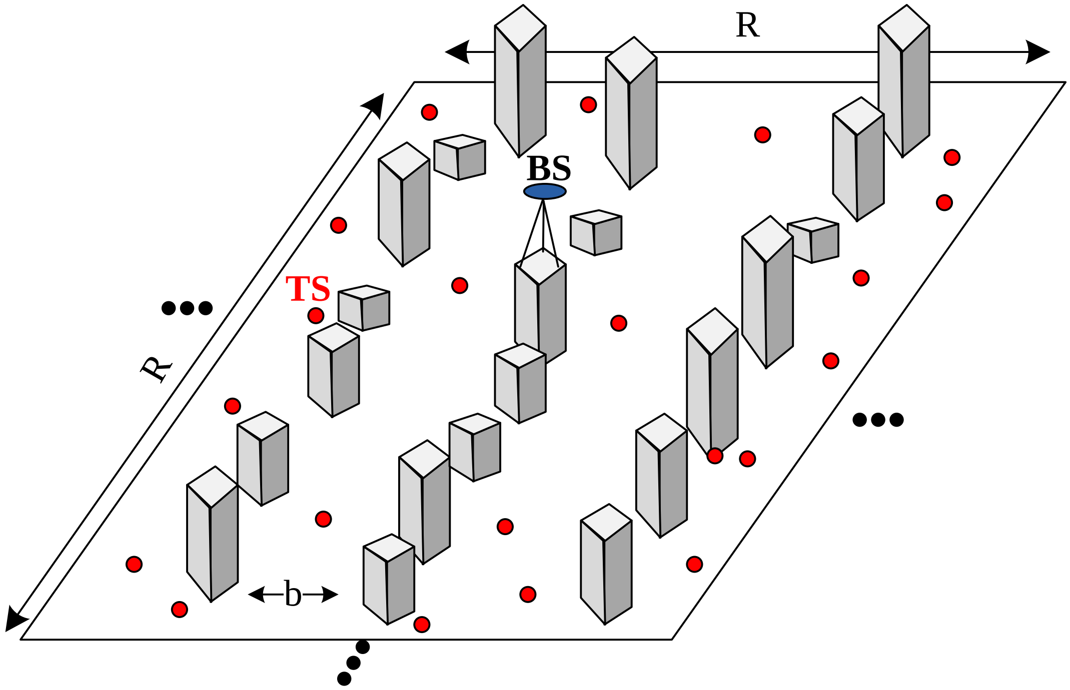

Figure 6-2: 3D model of a suburban R by R model, with variable building heights and fixed separation. BS located at the center, terminal stations distributed randomly (red dots).

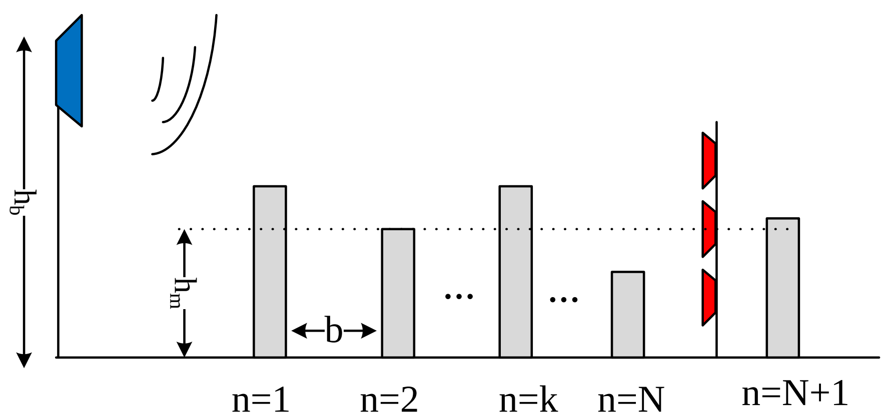

Figure 6-3: Equivalent 2D profile representation of each link from BS to each of the terminals.

6.3.1 Diffraction Model

The suitable diffraction model for our study is the one that can be used for suburban environments, takes into account building height variations and can handle multiple knife-edge diffraction. Ignoring the exact solutions such as the Voglar method [178] which are very accurate but computationally intensive and also classical models such as Giovanelli and Deygout models [179] which are mostly suitable for small number of knife-edge scenarios and are unable to calculate accurate diffraction loss for multiple edges, we choose Walfisch-Bertoni class of models. They decompose the path loss into three independent terms: Free space loss, L_0, Multiple-diffraction loss, L_{md} (due to signal propagation past the rows of building), and the diffraction loss from last building to receiver, L_{rtr}, then

$$L_{total} = L_0 + L_{md} + L_{trt} \,. \tag{6.2}$$

The following will describe methodology and corresponding formulas for each of these terms.

6.3.1.1 Free Space Loss

Propagation loss due to free space wavefront spreading can be calculated as

$$L_0 = -20\log[(\lambda / (4\pi r))], \tag{6.3}$$

where λ is the wavelength in metres, and r is the distance from the transmitter in metres.

6.3.1.2 Multiple-diffraction Loss

Multiple diffraction process unlike the last building diffraction loss is complicated by involving scattering in the transition region of diffraction, and thus cannot be treated by the simple Geometric Theory of Diffraction (GTD) and related asymptotic methods. Several models exist in the literature on the model of diffraction loss due to building losses such as Walfish-Bertoni [180], MBX [181], Xia [182], [183]. Walfisch-Bertoni model is limited for BS heights above the rooftop level. MBX model develops analytical model for BS antenna height of above, below and near average rooftop level. It improves accuracy of [180] by 0.5 dB and extends the validity of its range by accounting for BS antenna height below rooftop level as well. Xia model simplified the results of [180] and was corrected by [183]. However, due to computational limits, the expression can only be practically evaluated for up to 15 buildings.

Despite the fact that these models specifically the Walfisch Bertoni model have been widely used and verified with some other independent studies, they are limited to equal building heights and fixed spacing between them. Moreover, the assumption that TS antenna is located well below the rooftop level is not applicable for fixed wireless system analysis. The diffraction loss component of Walfisch-Bertoni model was modified in [165], [170], [176], [184] to include buildings random height variation into the prediction model either by Voglar or Fresnel-Kirchhoff integrals. The study in [170] used plane wave multiple edge technique of walfisch *et. al.* and assumed uniform building heights distributed between $\mu - \Delta / 2$ and $\mu + \Delta / 2$ where μ and Δ were average building height and maximum height deviation, respectively. The street level average signal strength was obtained by calculating diffraction loss using Fresnel-Kirchhoff integrals and adding the roof-top to receiver loss. It was shown that the average signal level in street level is reduced by -0.43Δ compared to Walfisch model and was independent of mean building height. This showed that Walfisch-Bertoni model in fact underestimate the average path loss because of equal building height assumption.

Saunders *et. al.* [176] used Monte-Carlo evaluation of the Voglar integral to calculate diffraction loss and, because of the complexity of this method, they just considered last five buildings in the model. The effect of random building height was found to increase the average path loss by 0.8 dB in 900 MHz and 1 m of building height variation, confirming the results obtained in [170]. Chung *et. al*. in [165] also used multiple edge technique of Walfisch *et. al.* with building modelled as attenuating phase or absorbing screens uniformly distributed between 6 m - 14 m. They also showed that Walfisch-Bertoni model underestimate the diffraction loss because of ignoring the building variation. A more simplified and comprehensive study of effect of building height variation on multi-diffraction loss component of total path loss can be found in [184].

In our study, we are using their Random Building Height (RBH) model in which Fresnel-Kirchhoff integrals are used to calculate diffraction loss. Their proposed technique originally was developed in [185] and later used by Piazzi in [186] assuming plane wave incident simulation technique and later was modified in [184] for cylindrical wave simulation technique in which transmitter is assumed to be a uniform magnetic line source. The technique is general enough to calculate the field amplitude and the corresponding diffraction loss value at any height. Figure 6-4 shows the geometry for the Fresnel-Kirchhoff evaluation of cylindrical wave in which buildings are modelled by absorbing half-screens, with different heights and fixed mean separation, *b*. The horizontal axis *r* is positioned at the area’s mean building height, μ_{hB}.

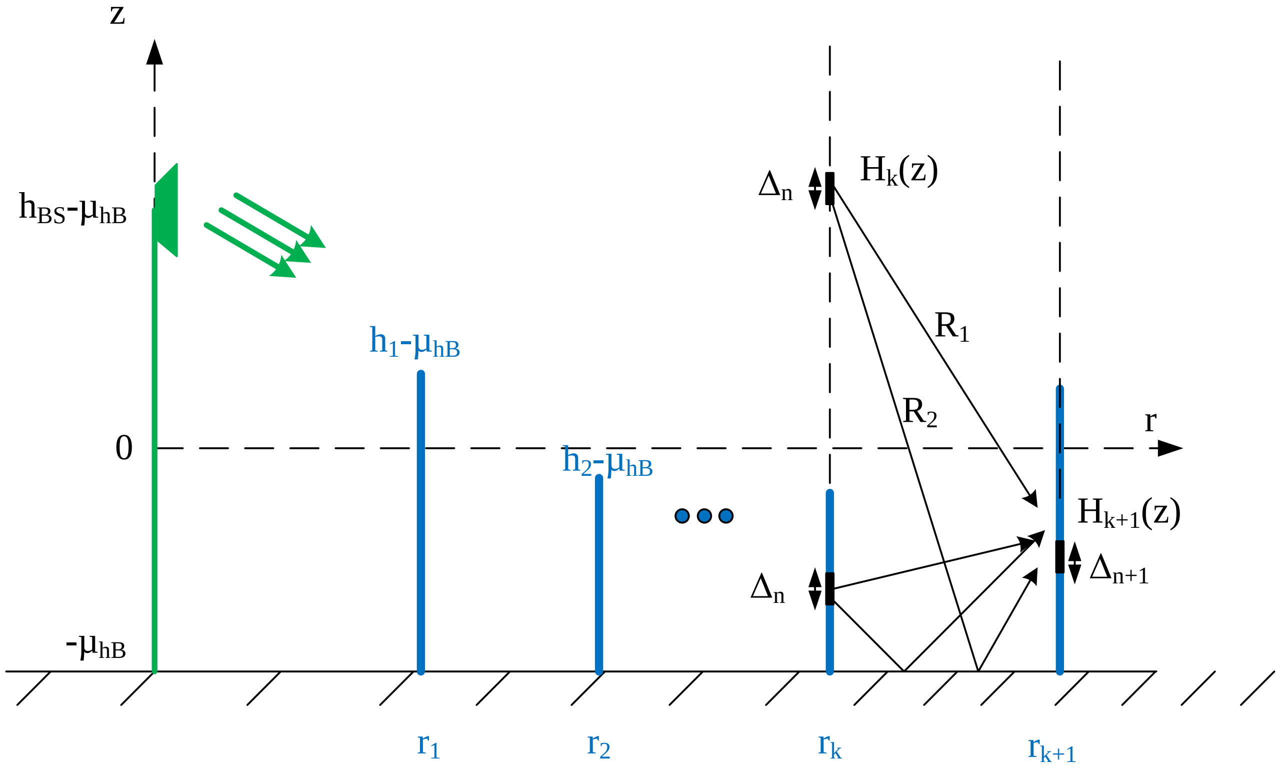

Figure 6-4: Geometry for the Fresnel-Kirchhoff evaluation of diffraction loss.

The transmitter is assumed to be uniform magnetic line source and the radiated cylindrical wave has *z* component only. In relatively far distances, the field on the first building screen can be approximated as (kr>>1)

$$H_0(z) \approx \frac{1}{\sqrt{kr}} e^{jkr} \ , \tag{6.4}$$

where

$$r = \sqrt{r_1^{\ 2} + (z - (h_{BS} - \mu_{hB}))^2} . \tag{6.5}$$

Then the field strength on (k+1)th screen is obtainable from the field on the kth screen which acts as a virtual transmitter. Using the physical optics (PO) integral and including the ground reflection we have

$$H_{k+1}(z) = \frac{e^{j\pi/4}}{\sqrt{\lambda}} \int_0^{\infty} H_k(z)[\frac{e^{-jkR_1}}{\sqrt{R_1}} + \Gamma_g \frac{e^{-jkR_2}}{\sqrt{R_2}}] \ , \tag{6.6}$$

where R_1 and R_2 are specified in Figure 6-4 and Γ_g is the ground reflection coefficient. By discretization and using linear interpolation of amplitude and phase of integrand over intervals of Δ, the resultant expression will be [184]

$$\begin{aligned} H_{k+1}(p\Delta_{n+1}) = \Delta_n e^{-j\pi/4} \cdot \sum_{m=\lfloor (h_n-\mu_{hB})/\Delta_n \rfloor}^{\infty} \{ & \frac{1}{D_{p,m}}[H_k(m\Delta_n+\Delta_n) f_{p,m+1} \\ & \cdot e^{-jkr_{p,m+1}} - H_n(m\Delta_n) f_{p,m} \cdot e^{-jkr_{p,m}}] \\ & + \frac{j}{kD_{p,m}{}^2} \cdot [H_k(m\Delta_n+\Delta_n) f_{p,m+1} \cdot e^{-jk(R_m-R_{m+1})} \\ & - H_k(m\Delta_n) f_{p,m}] \cdot [e^{-jk(R_{m+1}-R_m+r_{p,m+1})} - e^{-jkr_{p,m}}] , \end{aligned} \tag{6.7}$$

where

$$\begin{aligned} r_{p,m} &= \sqrt{(p\Delta_{n+1}-m\Delta_n)^2+b^2} \\ f_{p,m} &= \frac{nb/R_m + d/r_{p,m}}{2k\sqrt{\lambda r_{p,m}}} \\ R_m &= \sqrt{(nb)^2+(h_{BS}-\mu_{hB}-m\Delta_n)^2} \\ D_{p,m} &= R_m - R_{m+1} + r_{p,m} - r_{p,m+1} , \end{aligned} \tag{6.8}$$

and $\lfloor x \rfloor$ is the floor of *x*, Δn and $\Delta n+1$ $_{+1}$are step sizes on screen *n* and *n*+1, respectively.

Different step sizes are used on the screens to minimize round off errors which may happen in some instances. Before starting to take integral over the (*k*+1)th screen, the calculated field values on *k*th screen was re-sampled at new spacing in order to reduce the number of simulation points to an acceptable size while avoiding the condition that leads to generation of large round off errors as was described in [184]. The new sampling interval becomes

$$\Delta'_k = \frac{h_{BS}-\mu_{hB}}{(k+1)q_k} , \tag{6.9}$$

where q_k is an integer chosen appropriately to ensure new spacing is less than **λ**/4. The spacing on the (*k*+1)th screen is then calculated as

$$\Delta'_{k+1} = \frac{k+1}{k} \Delta'_k \ . \tag{6.10}$$

Another practical consideration when implementing the integration is truncation methodology. Since one of the limits of the integral in (6.6) is infinite, it needs to be truncated. We used Kaiser-Bessel windowing function which was proven to be effective to smoothly reduce the integral to zero and avoid spurious contribution that would result from abrupt termination [165], [187].

6.3.1.3 Last Rooftop to Receiver Loss

The last rooftop-to-receiver loss was first postulated by Allsebrook and Parsons in [188]. This was later compared to measurement data in Tokyo city by Ikegami *et. al* [189], [190] which concluded that this portion of path loss mainly depends on the receiver height. So, based on the location of the terminal antenna with respect to average rooftop height, we are using different path loss formulas to calculate L_{rtr} . Figure 6-5 shows the geometry for the last building to the receiver loss calculations.

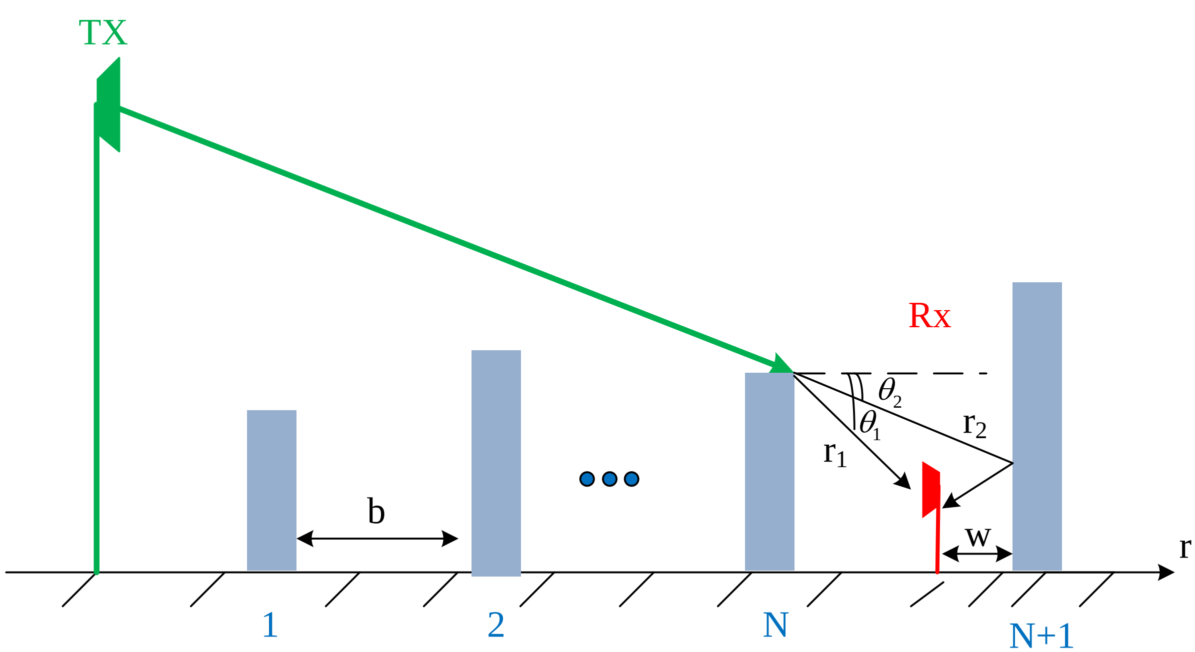

Figure 6-5: Geometry for the last building to receiver loss calculation.

a. Receiver below the average rooftop level:

Assuming the building before the terminal is absorbing screen and antenna is in the shadow region of the building next to it, the loss is calculated using GTD as [180], [191], [192]

$$Lrtr = \frac{1}{2\pi k \cos\varphi}[\frac{1}{r_1} D^2(\theta_1) + \frac{1}{r_2} \Gamma^2 D^2(\theta_2)] \,, \tag{6.11}$$

Where φ is the angle between the direction of the propagation and *r* axis And the diffraction coefficients are given by

$$D(\theta_i) = \frac{1}{\theta_i} - \frac{1}{\theta_i + 2\pi} \,, \tag{6.12}$$

where the angles mentioned in (6.12) are specified in Figure 6-5. It includes the loss due to ray propagates from edge of the last building down to receiver and also the loss from reflection of the second ray by the building on the opposite side of the street and Γ is reflection coefficient at the building face.

b. Receiver above the average rooftop level:

There exist several options with different range of applicability to calculate height gain of the terminal antennas in above average rooftop regions. Okumura-Hata, standard ITU-R, ECC-33, and SUI gain factors are among those models [165], [193], [194]. However, they either put restriction on maximum receiver height or are limited to specific range of frequencies. So in our model we are using the expression which was obtained from numerical analysis in [152]. The advantage of this formulation is that it has building heights variation effects included in the L_{rtr} This makes both L_{md} and L_{rtr} consistent in our study. According to the formulation in [152], the approximate expression for height gain factor of antenna will be

$$A(h_{TS}) = -20\log_{10}(1 + a_1 p_a + a_2 {p_a}^2) \,, \tag{6.13}$$

where,

$$\begin{aligned} a_1 &= 0.9 + 1.3e^{-0.866s} \\ a_2 &= 1.0 - 0.5e^{-1.823s} \\ p_a &= \frac{h_{TS} - m_{hB}}{(/b)^{0.45}} \,, \end{aligned} \tag{6.14}$$

and σ is the standard deviation of the building heights.

6.3.2 Shadow Fading and Its Impact on System Coverage

Shadow fading has been proven to impact system coverage. The total path loss assuming the fast fading is averaged out, is consist of mean and shadowing component as

$$pathloss = \bar{L} + S \ , \tag{6.15}$$

where L is the mean path loss and S is SF. Assuming a Lognormal distribution for S, we will have the probability distribution function as

$$p(S) = \frac{1}{\sigma_{SF}\sqrt{2\pi}} e^{-\frac{s}{2\sigma_{SF}^2}} \ , \tag{6.16}$$

where σ_{SF} is the SF standard deviation. System *edge coverage* is defined as the fraction of locations at the edge of the network (*e.g.*, $r = r_0$) wherein a terminal station would experience a received signal above the threshold (Th) [195].

Here, we define the threshold as difference between mean path loss at the edge of the system and the minimum sensitivity of the receiver plus a constant fade margin. The probability that S exceeds the threshold at the distance of r_0 from BS will be

$$\begin{aligned} P_{edge}(r = r_0) &= \Pr(s > Th) = \int_{S=Th}^{\infty} p(s)ds \\ &= \int_{S=Th}^{\infty} \frac{1}{\sigma_{SF}\sqrt{2\pi}} e^{-\frac{s}{2\sigma_{SF}^2}} ds \ . \end{aligned} \tag{6.17}$$

Simplifying (6.17) by normalizing the variable in the integral, the result will be [164]

$$\Pr(s > Th) = Q(\frac{Th}{\sigma_{SF}}) \ , \tag{6.18}$$

where

$$Q(x) = \frac{1}{\sqrt{2\pi}} \int_{x}^{\infty} \exp(-\frac{x^2}{2})dx = \frac{1}{2} erfc(\frac{x}{\sqrt{2}}) \tag{6.19}$$

is the complementary cumulative normal distribution. Area Coverage is defined as the percentage of locations within a circle of radius R in which the received signal strength exceeds a particular threshold value [195]. Accordingly, using the Edge Coverage expression of (6.18) and imagining that the area is covered by the cascades of rings with radius of r and width of dr, one can write the whole cell (area) coverage probability as [164]

$$
\begin{aligned}
p_{area} &= \frac{1}{\pi R^2}\int_{r=0}^{r=R} 2\pi r \times p_{edge}(r)dr \\
&= 0.5 + \frac{1}{R^2}\int_{r=0}^{r=R} r \cdot erf\left(\frac{Th}{\sqrt{2}\sigma_{SF}}\right) .
\end{aligned} \tag{6.20}
$$

Equation (6.20) shows that depth of shadowing has direct effect in the system edge and area coverages. In the result section of this chapter we will show the effect of observed SF behavior with terminal height on both system edge and area coverage.

6.3.3 Parameters of the Simulation

In order to simulate a typical suburban environment as closely as possible to the environment that our measurements took place, we chose following simulation parameter in Table 6-1. The results presented in next section are calculated using these parameters.

Table 6-1: Simulation parameters

Parameter	Value	Parameter	Value
Frequency (f)	2 GHz	Number of simulated links (Monte-Carlo)	5000
Base Station antenna height (h_{BS})	40 m	Grid dimension (RxR)	10 km
Terminal Station antenna height (h_{TS})	Between 1 m-14 m	Building surface reflection coefficient	0.3
Mean building heights (μ_{hB})	Between 5 m-9 m	Building width [196]	7.5 m
Mean separation between buildings (b)	30 m	Building height variation (σ_B)	Between 0 m-6 m
Receiver fade margin	5 dB	Terminal distance from the adjacent building (w)	6 m

It should be noted that although TS antenna locations were chosen randomly within the grid, in order to take the deployment realities into account, *i.e.*, location of utility poles, the location of the receiver between last building and the building at the opposite side of the road was forced to be *w* metres as shown in Figure 6-5. For each of the simulated links, the path was sampled in mean buildings separation distance and at each sample point an absorbing screen was placed as representation of a building. The heights of the screen were determined under two criteria. If the sampled point was located on a building, the height of screen was chosen equal to that building's height, otherwise, interpolation technique was used to estimate height based on the heights of surrounding buildings. Figure 6-6 shows the applied sampling methodology. This results in creating a 2D profile for each of the links as shown in Figure 6-3. The results for SF analysis are presented in the following section.

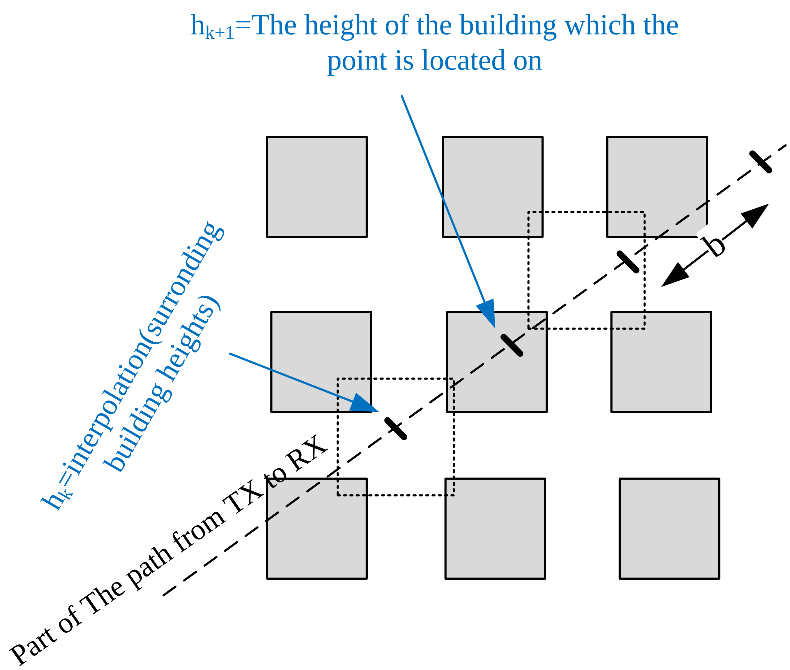

Figure 6-6: Sampling the link between Tx and TS with interval b

6.4 Results and Implications

In this section we present a series of results obtained using MATLAB simulation codes and the parameters defined in Table 6-1.

6.4.1 Effect of Terminal Height on the Depth of Shadow Fading

We ran Monte-Carlo simulation for 5000 times each time choosing a random location on the grid of buildings. We calculated path loss and shadowing using the models described in the previous section. Since the behavior of the depth of shadowing with terminal height is the parameter of interest, we repeated the above mentioned simulation for 14 different terminal heights starting from 1 m above the ground up to 14 m in 1 m steps. The area's mean building height, separation between the buildings and their variance, unless otherwise stated, were unchanged between the simulations as 8 m, 30 m and 3 m, respectively.

Figure 6-7 - Figure 6-12 show the results of calculated path losses for all the 5000 links and shadowing distribution for three representative terminal heights. We chose the results to show here for terminals at very low height (1 m or 0.125 μ_{hB}), at mean building height (8 m or 1 μ_{hB}) and very high (14 m or 1.75 μ_{hB}) .

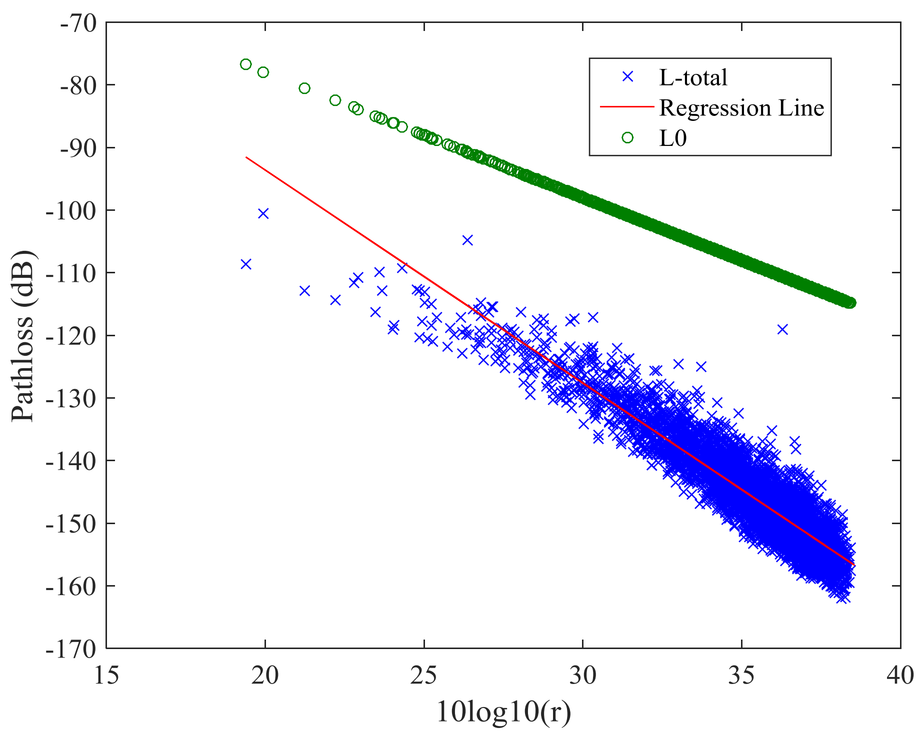

Figure 6-7: Path loss plot versus distance for terminal heights at 0.125 μ_{hB} .

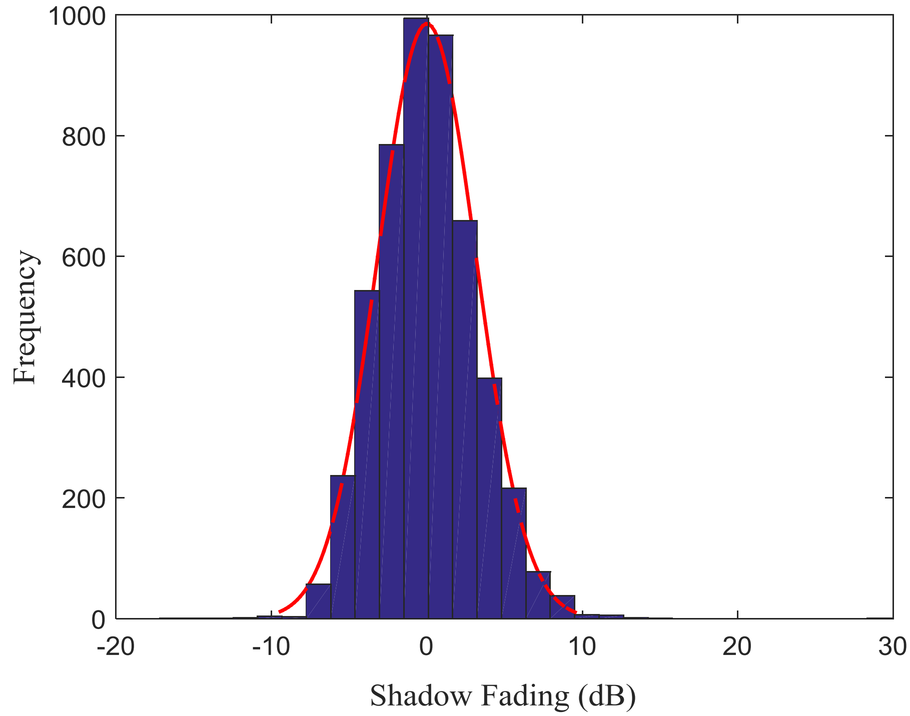

Figure 6-8: Shadowing distribution for terminal heights at 0.125 μ_{hB} .

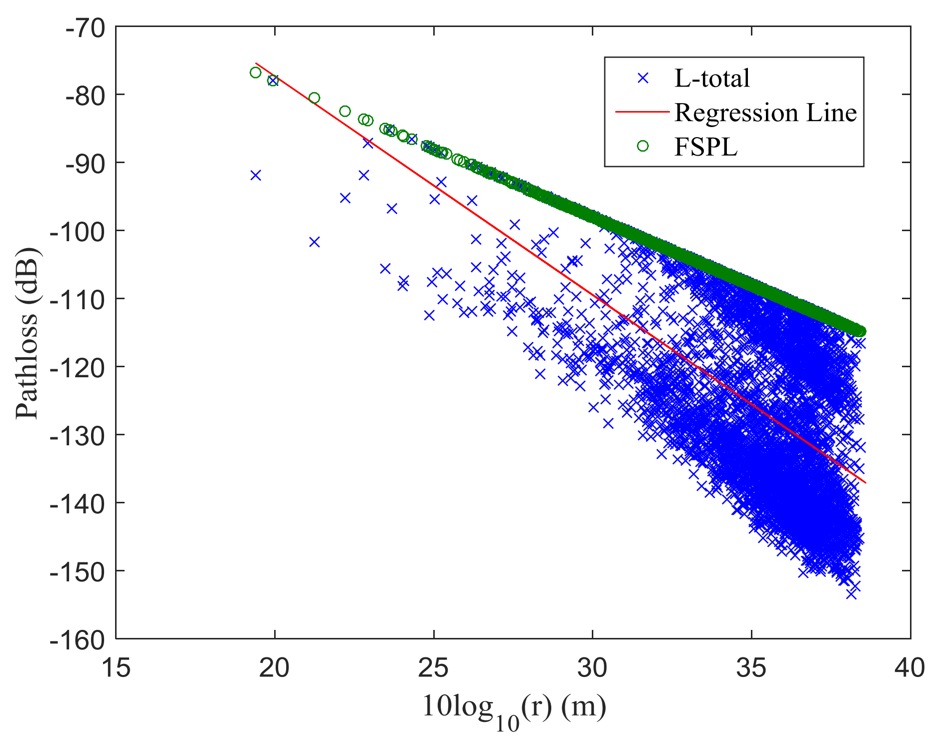

Figure 6-9:Path loss plot versus distance for terminal heights at 1 μ_{hB}.

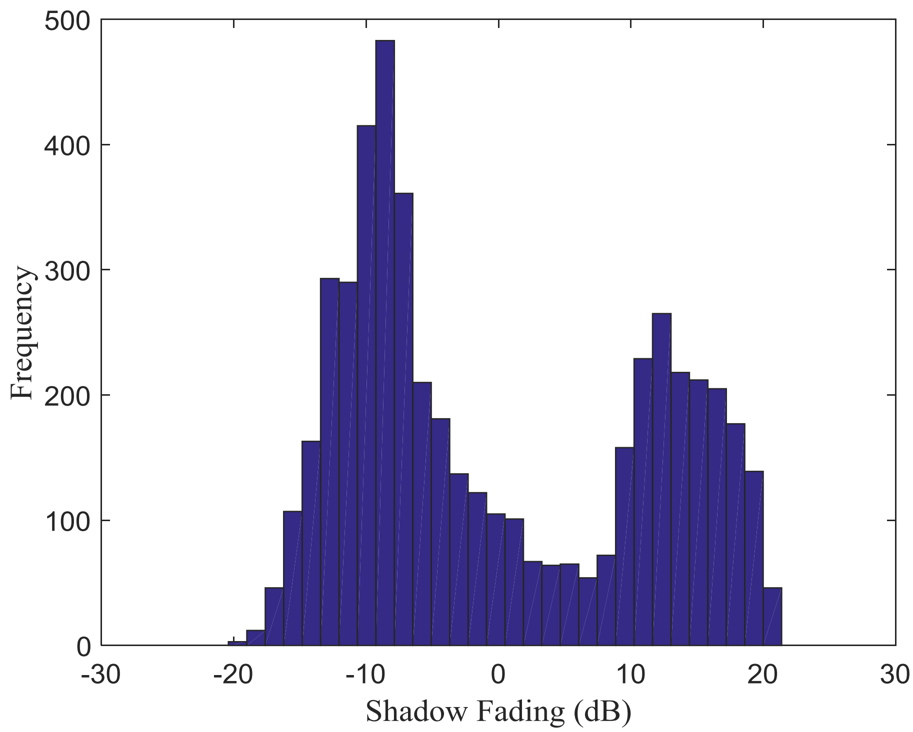

Figure 6-10: Shadowing distribution for terminal heights at 1 μ_{hB} .

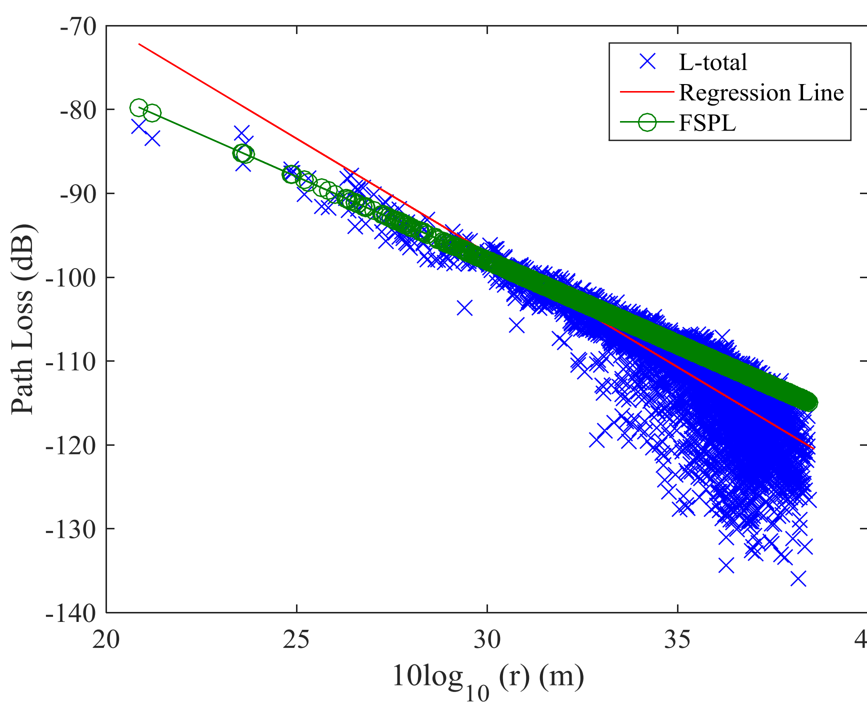

Figure 6-11: Path loss plot versus distance for terminal heights at 1.75 μ_{hB} .

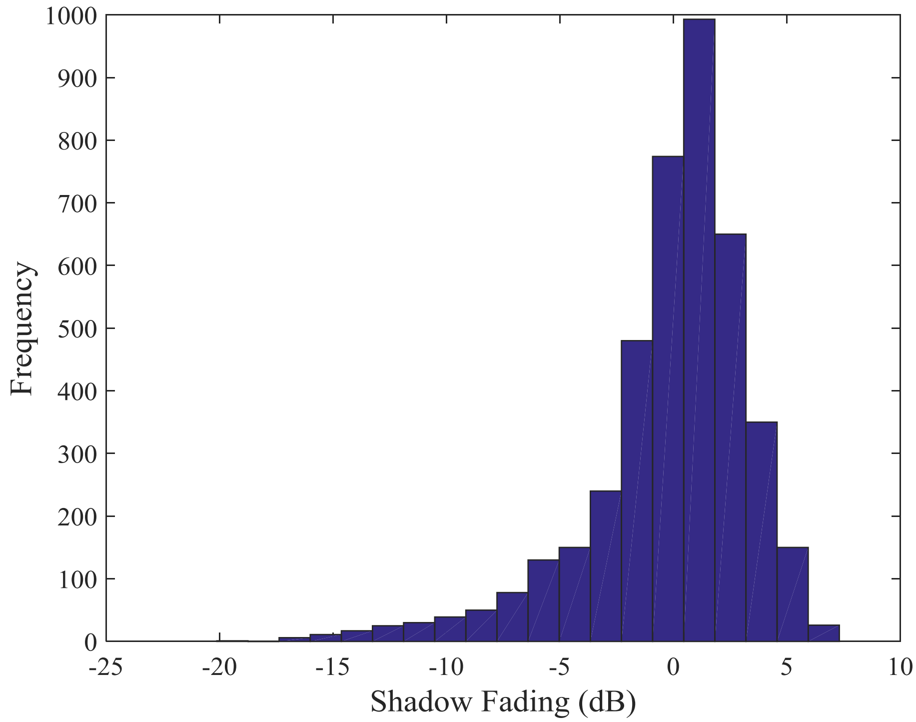

Figure 6-12: Shadowing distribution for terminal heights at 1.75 μ_{hB} .

It is seen that in low terminal heights, distribution of shadowing follows Lognormal. As terminal heights increase, more and more of the terminals experience LOS or semi-LOS signals. Semi-LOS means that the link is not in pure LOS situation but the terminal's received signal strength is better compared to its previous height and it is less blocked by the buildings. This causes the terminals to get closer to LOS path loss line in path loss versus distance plot (FSPL line in the figures). However, as stated before, the degree of improvement for different terminal locations is different, therefore some points will still keep their NLOS situation.

As seen in path loss plot of 8 m terminals, this causes the points get separated into two groups. From these results, it seems the distribution at mean building height follows mix of two Lognormal distributions known as Gaussian Mixture Model (GMM) rather than unimodal Lognormal. It worth to mention that Lognormal distribution results from two main random processes in the model we used in our study. One is the random building height effects and the other one is the random effect due to diffraction from last building down to the terminal [197].

The building height variation effect on diffraction losses is same for all the receivers with same location in the grid. The main reason of the variation of the path loss and consequently the SF behavior for a single location in different heights is because of last building to receiver loss that is different for the receivers in different heights. Otherwise, if diffraction loss due to propagation over the building was the only effective loss, because of central limit theorem, the distribution would always be Lognormal.

As explained before, since design and deployment of fixed wireless systems in SG is necessary to be handled by statistical approaches because of large number of endpoints and geographical area, rather than engineering the links individually, in this section we study the behavior of the standard deviation of equivalent Lognormal shadowing at each height, *i.e.*, without separating links into LOS, semi-LOS and NLOS. However, in order to get more insight into the model of SF distribution with terminal height, we will study parameters of the mixture model in Section 6.4.3. In the rest of this section, we obtained path loss component for each height and fitted shadowing data into Lognormal distribution and obtained its standard deviation. Figure 6-13 and Figure 6-14 show the behavior of path loss component and depth of shadowing with terminal height, respectively. The path loss component expectedly decreases as terminal height increases and shadowing standard deviation has a maximum at 8-m height (*i.e.*, mean building height).

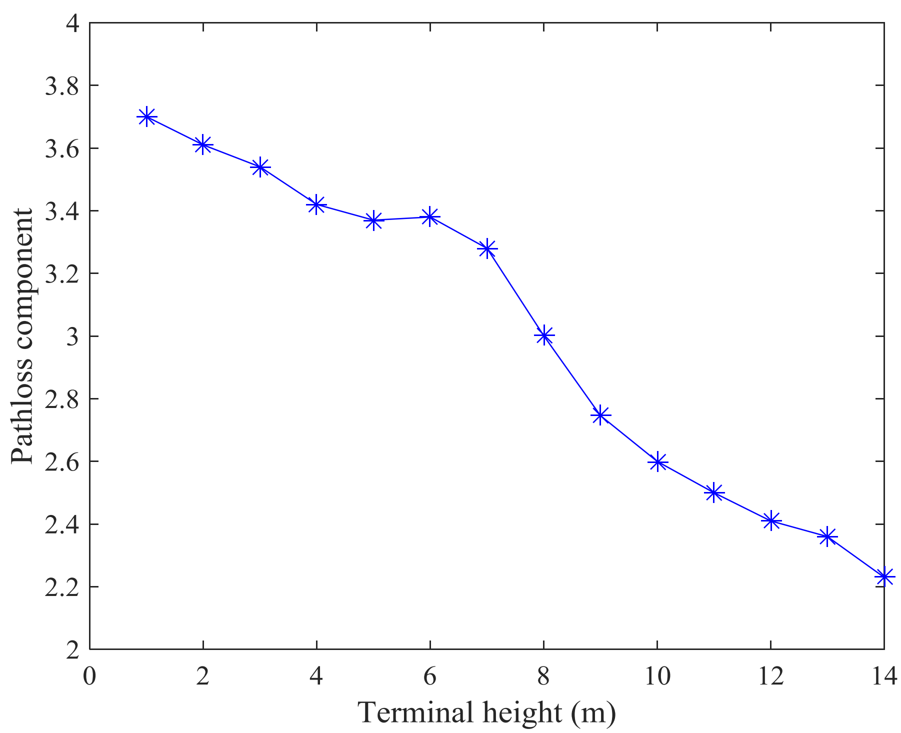

Figure 6-13: Path loss component variation with terminal heights.

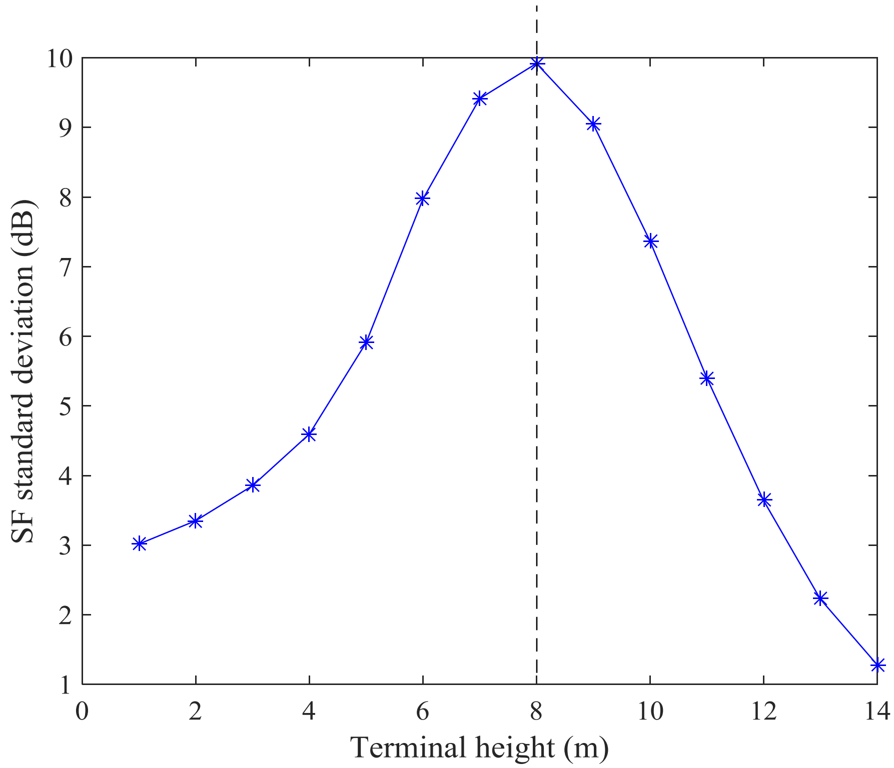

Figure 6-14: Shadow fading standard deviation variation with terminal heights.

We repeated these simulations for suburban model with different mean building heights from 5 m - 9 m, while building height variance and separation was kept fixed. Figure 6-15 shows the effect of area's mean building height on peak of the SF. For the ease of tracking the trend, a 2D colour plot also is plotted in Figure 6-16. It is seen that the maximum of the SF standard deviation occurs when terminal height and mean building heights are equal. Moreover, it is observed that the peaks of standard deviations are not changing significantly with mean building height. In the following section we will show that the maximum value of the shadowing standard deviation is mostly affected by building height variance.

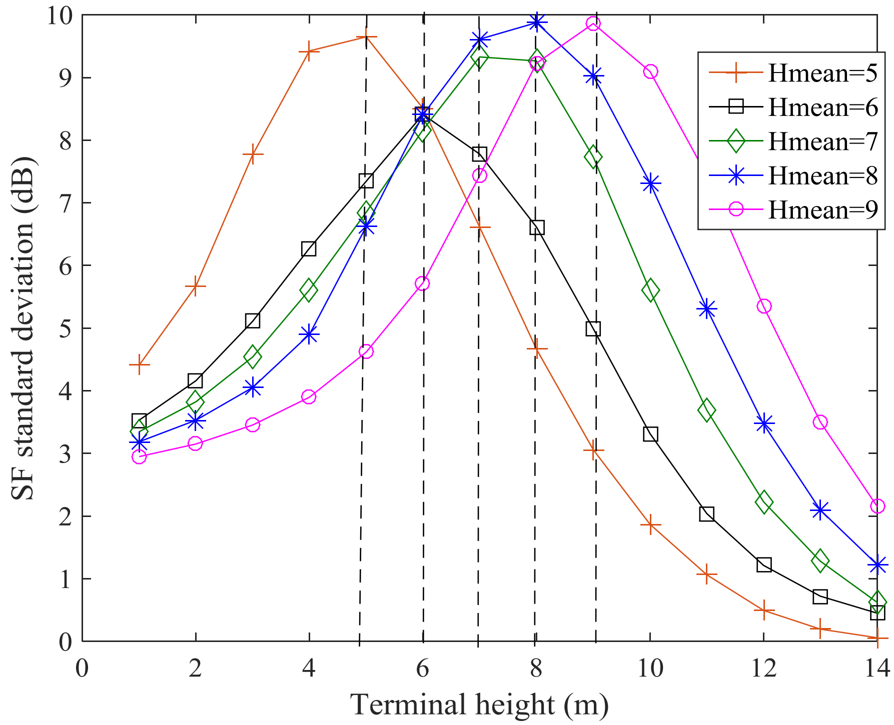

Figure 6-15: Effect of area's mean building height on shadow fading standard deviation.

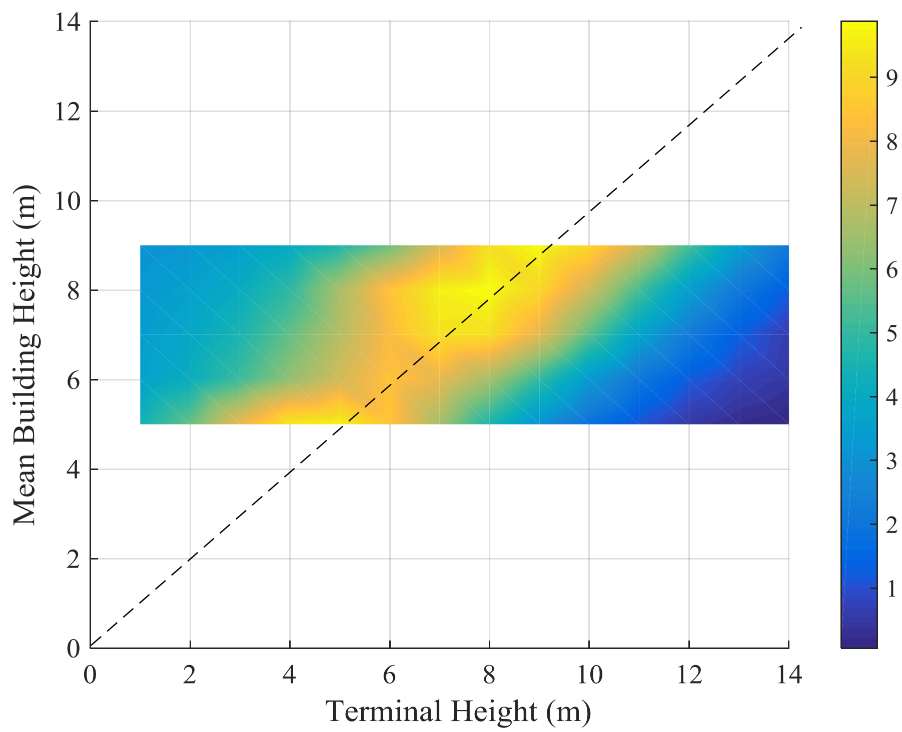

Figure 6-16: SF standard deviation variation with area's mean building height and terminal heights (2D colour plot).

6.4.2 Effect of Area Building Height Variance on the Depth of Shadow Fading

The Monte-Carlo simulation for 5000 links was run 6 times, each times changing the grid's building heights standard deviation from 0 m to 5 m in 1 m steps. This replicates wide variety of suburbans with planning policy of buildings with fixed heights (σ=0) or with very variant heights (σ=5). Then we calculated the path loss and SF for the links within each run. Figure 6-17 shows the variation of path loss component with terminal heights for different buildings height variances. As it was expected, increasing terminal height decreases the path loss component, *i.e.*, smaller mean path loss. According to the results, path loss component of an area with larger building height variance is higher compared to an area with smaller variance.

Figure 6-18 shows the variation of SF standard deviation with terminal height for different building height variation. As it was shown in previous section, the maximum depth of SF occurs at area's mean building height (here 8 m). It is seen that SF standard deviation for the area with larger building height variation is higher than the areas with less variant building heights for all the terminal heights. In Figure 6-19 we plotted the maximum of shadowing standard deviation that happens at mean building height and we conclude that the depth of SF increases with the variance of the building's height.

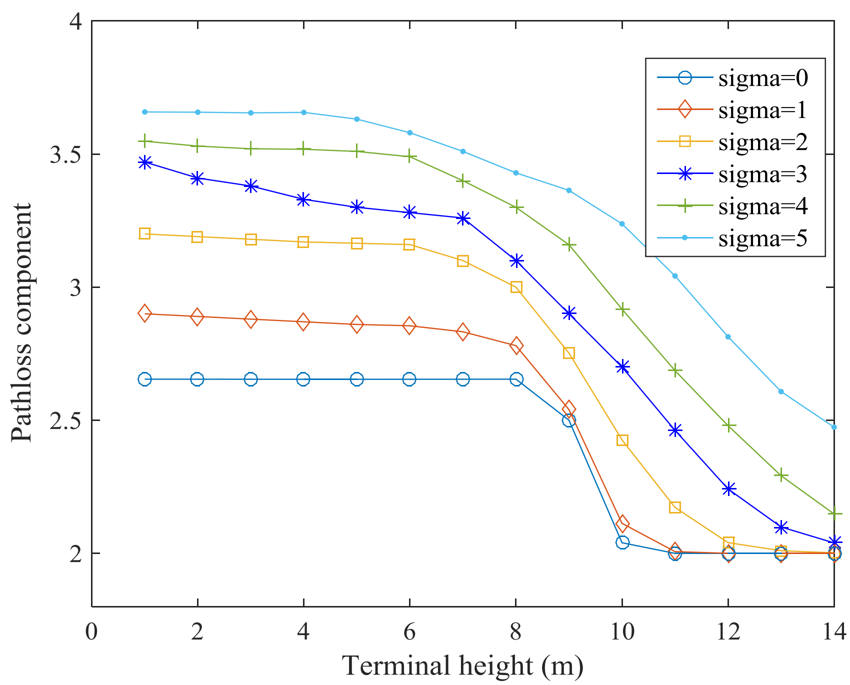

Figure 6-17: Path loss component variation with terminal heights for different buildings height variation with μ_{hB} =8 m.

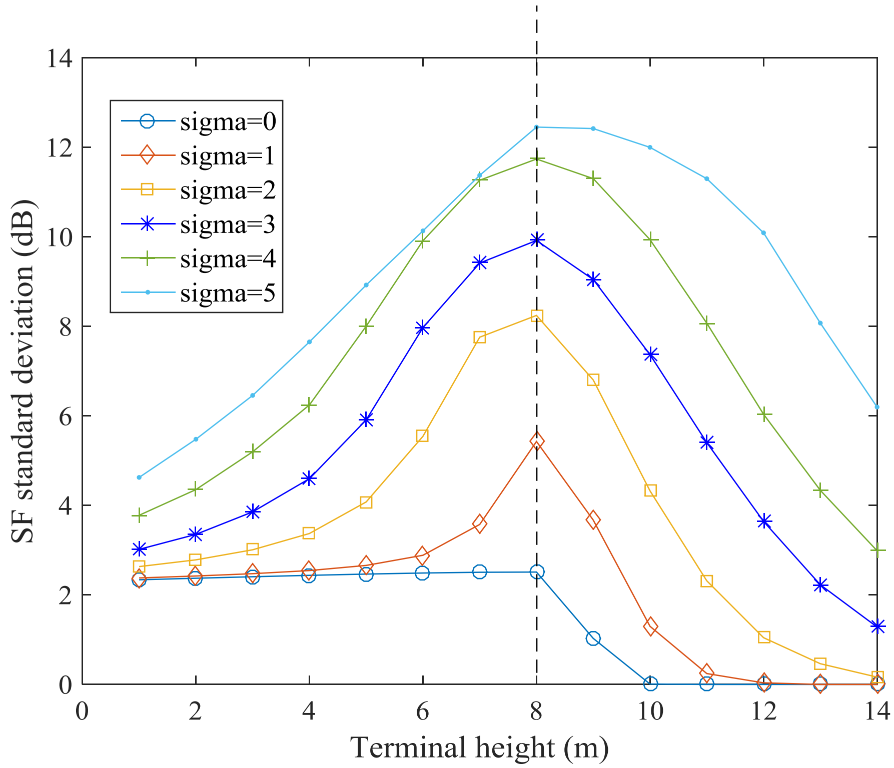

Figure 6-18: Shadow Fading Standard Deviation variation with terminal heights for different buildings height variation with μ_{hB}=8 m.

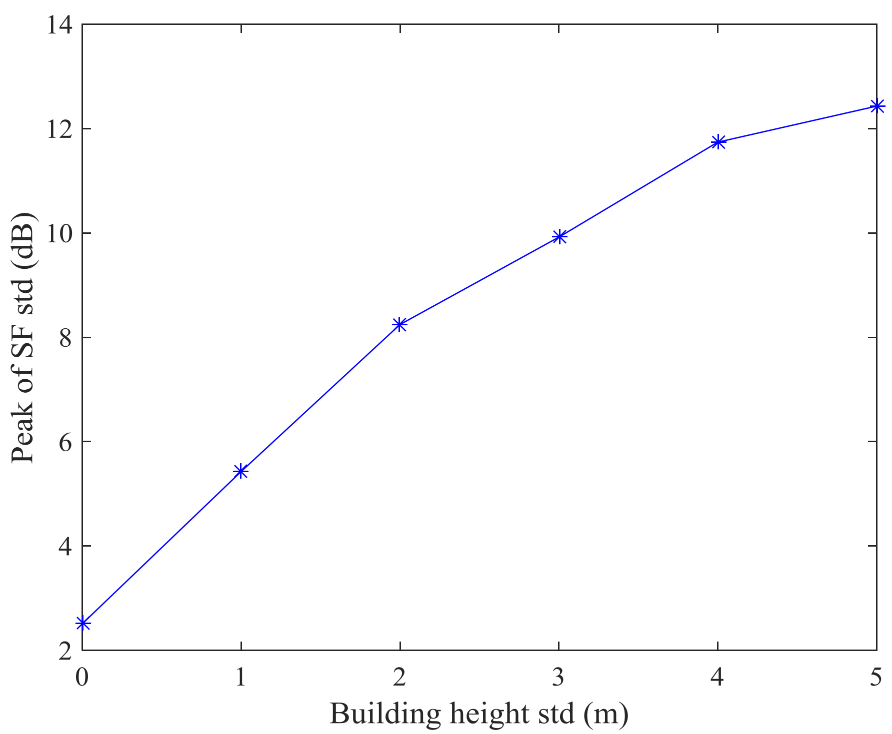

Figure 6-19: Effect of buildings height variation on the peak of shadow fading standard deviation ($_{hB}$ =8 m).

6.4.3 Effect of Terminal Height on the Distribution of Shadow Fading

In this section, we characterize the observed behavior of SF distribution around mean building height. As mentioned before, distribution looks to be fitted better with a mix of two Gaussian Lognormal known as bimodal Gaussian Mixture Model (GMM) rather than unimodal Lognormal distribution. In the following we will argue about how reasonable this model is and will determine the best number of components needed to fit into GMM using Akaike Information Criterion (AIC) and Bayesian Information Criterion (BIC) and further we will study the parameters of the proposed model and their dependency on building height characteristics.

In general, finite mixture models are a convex combination of two or more probability distribution function and provide a natural representation of heterogeneity in a finite data set. They are capable of approximating any arbitrary distribution [198]. Popular mixture models are Gaussian, Poisson, Gamma, Negative Binomial, Weibull, Exponential, and any combination of those, widely used in the broad types of research fields such as Astronomical analysis, Disease survivals studies, voice and image processing [199]–[201]. According to the results presented in previous section, the histogram of SF shows two distinct bump due to separation between links with strong and weak signals in the path loss plot. Considering the fact that the building heights have random effect on improving signal quality when terminal is around average rooftop height, and consequently the central limit theorem effect, use of Gaussian Mixture Model with two component (bimodality) will be a reasonable choice.

The probability density function of a Gaussian mixture model with K components is defined as [198]

$$p(s\,|\,\Theta) = \sum_{k=1}^{K} \alpha_k N(s\,|\,(\mu_k, \sigma_k^2)) \;, \tag{6.21}$$

where N is Gaussian distribution with mixing portion α ($\sum_{i=1}^{K} \alpha_i = 1$) and mean and standard deviation of μ and σ, respectively, and

$$\Theta = (\alpha_{i=1...K},\ \mu_{i=1...K},\ \sigma_{1...K}^2) \tag{6.22}$$

is set of parameters. Then, for a given univariate SF data set, S, with N number of independent observations, the likelihood function of the data is given by

$$\ell(\Theta \mid S) = \prod_{i=1}^{N} \sum_{k=1}^{K} \alpha_k N(s_i \mid (\mu_k, \sigma_k^2)) \ . \tag{6.23}$$

Then the problem of Gaussian mixture estimation from N observation will be to find the set of parameter Θ that gives the maximum likelihood (ML) estimation solution as

$$\Theta^* = \arg\max_{\Theta} \ell(\Theta \mid S) \ . \tag{6.24}$$

Among the various parameter estimation methods, ML method implemented by EM algorithm [202] has been widely used. The EM algorithm is a general optimization technique and provides a method to iteratively update model parameters such that the log-likelihood of the data is guaranteed not to decrease at each step. It is famous for its simplicity and monotonic convergence that leads to estimation within the admissible range if the initial values are within the admissible range. On the other hand, EM has been proven to have some drawbacks as well, such as slow convergence, and need for suitable stopping rules and dependence on the choice of initial values in order to reach the global maximum. These issues have been dealt with many people in the literature [203], [204].

The standard *gmdistribution* object of MATLAB was used in order to fit the SF data obtained for different suburban building height scenarios into GMM with K components. This object in fact implements the above-mentioned EM algorithm and the details of it can be found in [198]. Initial values were provided to the function as following: the initial mean values were selected by calculating mean of points with positive and negative shadowing, respectively. This provides a close estimation to the final the mean. However for the standard deviation there was no specific estimation and their value was chosen randomly. The mixture portion parameters were chosen equally for both modes. However, in order to prevent algorithm to trap into flat log-likelihood estimations (which is shown to be a problem associated with EM algorithm), we repeated GMM estimation 100 times each time providing new random standard deviation values as initial values and at the end estimation with largest log-likelihood was selected as output. Maximum acceptable error of EM algorithm was set at 1e-10.

Before extracting bimodal GMM we first show that at the average rooftop heights shadowing can be better estimated with two modes (K = 2) rather than K = 1. We compare AIC [205] and BIC [206] values of the estimations obtained from MATLAB runs once with K = 2 and once with K = 1 for 5000 SF observations at mean building height. The estimation that corresponds to a lower AIC and BIC values means a better fit. Figure 6-20 shows the proper values for the number of GMM components for different simulation data (different mean building heights) at different TS heights. As expected, the height that corresponds to mean building height is better fitted with K = 2 rather than K = 1. So in the following, we will focus on fitting the shadowing data at average building height using GMM with two components.

a. Bimodal GMM parameter variation with area's mean building height

The above-mentioned approach was used to obtain the parameters of the Gaussian mixture distributions with two modes (K = 2) for the SF data of TSs at mean building height for different simulation runs. Area's mean building height was changed from 5 m to 10 m in 1 m steps between the simulation runs. Figure 6-21 shows an example of SF normalized histogram observed at terminal height of 8 m for an area with 8 m mean building height and 3 m building height standard deviation. The parameters of the interest are specified on the figure and mainly are means and standard deviations of the two distributions. It is obvious that σ_1 and μ_1 mainly correspond to links with deep shadowing and σ_2 and μ_2 correspond to less shadowed links (not necessarily LOS though).

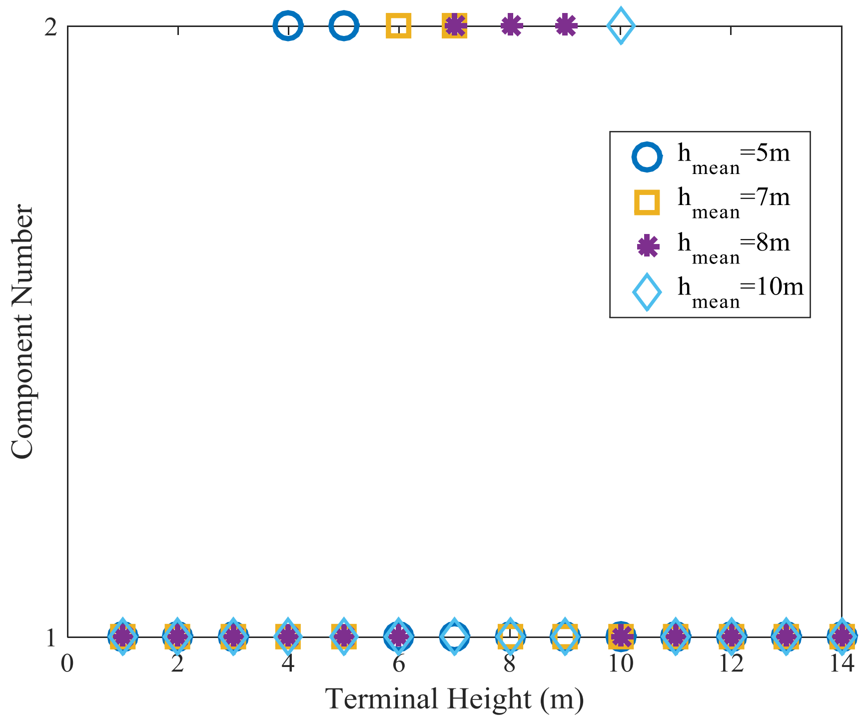

Figure 6-20: Comparing suitability of fitting with two GMM components versus unimodal fitting at different TS heights.

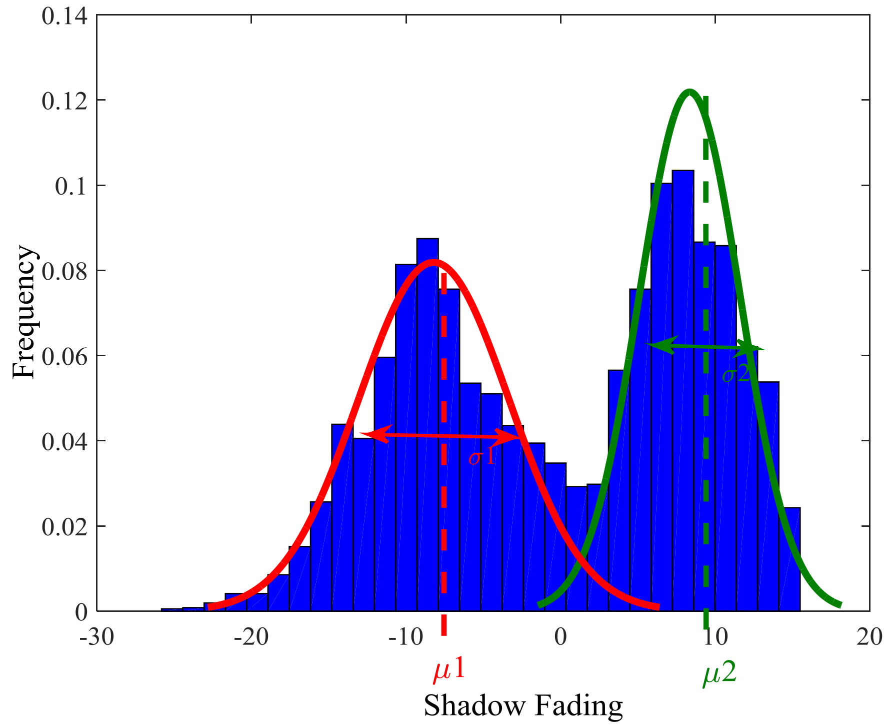

Figure 6-21: Shadow fading normalized histogram for terminal heights at 1 μ_{hB} for an area with 8 m mean building height.

Figure 6-22 and Figure 6-23 are comparing the mean and standard deviation variation of the GMM with mean building height variation, respectively. It is observed that the distance between the means ($\Delta\mu = \mu 2 - \mu 1$) is independent of the mean building height. The standard deviation of the first component which corresponds to deeply shadowed links decreases slightly and there is also slight increase in standard deviation of links corresponds to less obstructed one. However, the variation of standard deviations is small (within 1 dB). In summary, the mean building height has negligible effect on parameters of the Bimodal Gaussian model.

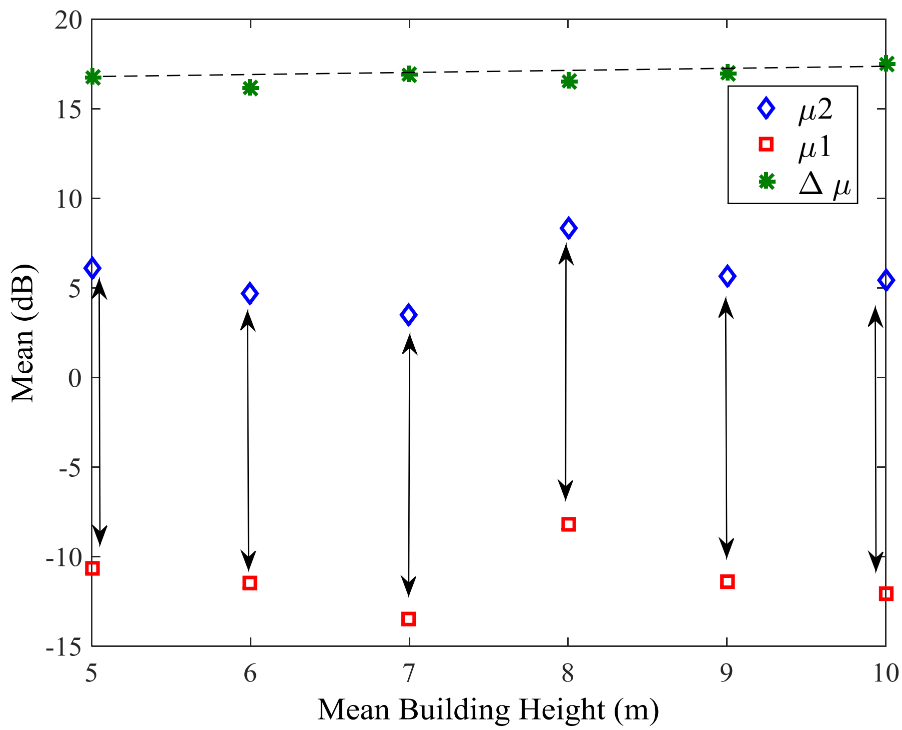

Figure 6-22: Variation of the GMM means and separation in different mean building height.

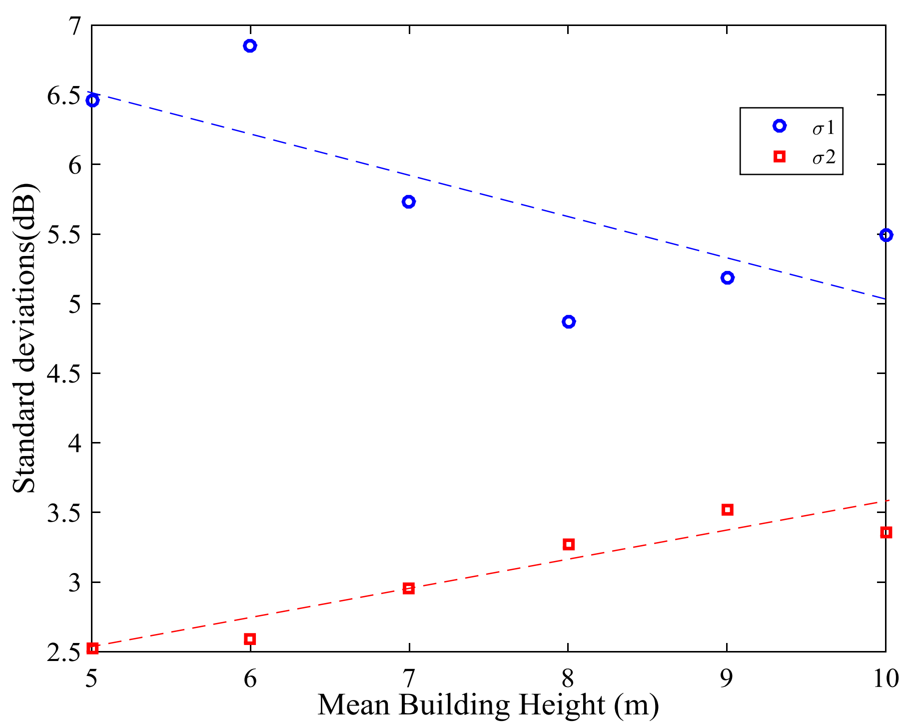

Figure 6-23: Variation of the GMM standard deviations in different mean building height.

The sensitivity of likelihood ratio test to the assumption of Gaussian distribution requires additional independent tests of bimodality. A useful and intuitive statistic is the *separation of the means relative to their width* [207]

$$D = \frac{|\mu_1 - \mu_2|}{\sqrt{(\sigma_1^2 + \sigma_2^2)/2}} \ , \tag{6.25}$$

where it was shown that D>2 is an indication that a clean separation between the modes is made by the EM algorithm and validity of the results is assured. In other word, if GMM method detects two modes with small separation (D<2), such split is not meaningful. Table 6-2 shows the calculated separations of the means relative to their width (D) for the results presented above. In all cases the D parameter was larger than 3 which is in agreement with the results presented in Figure 6-20.

Table 6-2: Separation of GMM means relative to width in areas with different mean building heights.

Mean Building Height (m)	5	6	7	8	9	10
D	3.4	3.1	3.7	3.9	3.8	3.8

b. Bimodal GMM parameter variation with building height variance

Similar to part *a*, several simulation scenarios were analyzed in order to characterize the effect of building height variation on the parameters of the bimodal GMM. Buildings height standard deviations of 0 m up to 6 m with 1 m steps were analyzed. In all the scenarios, mean building heights were chosen fixed 8 m. Figure 6-24 and Figure 6-25 show the variation of means and standard deviation with building height standard deviation, respectively. It is observed that the distance between means increases with building height variances. This implies that in general in a suburban environment with larger height variation, the links that are shadowed will have larger average depth of shadowing and the links that are less obstructed will have better signal quality compared to an environment with smaller building height variation. However, shadowing standard deviation for both modes increases as shown in Figure 6-25. The *portion* parameter of each mode in percentage (as was introduced in (6.22)) is plotted in Figure 6-26. It is seen that both mode contributes almost equal amount under all building height variation. This result is useful when calculating SF random value for link budget calculations when terminals are deployed at area's mean building height. Table 6-3 shows the calculated D parameters for each case. In all of the scenarios, D is larger than 2.5, therefore the presented bimodal distribution parameters are meaningful.

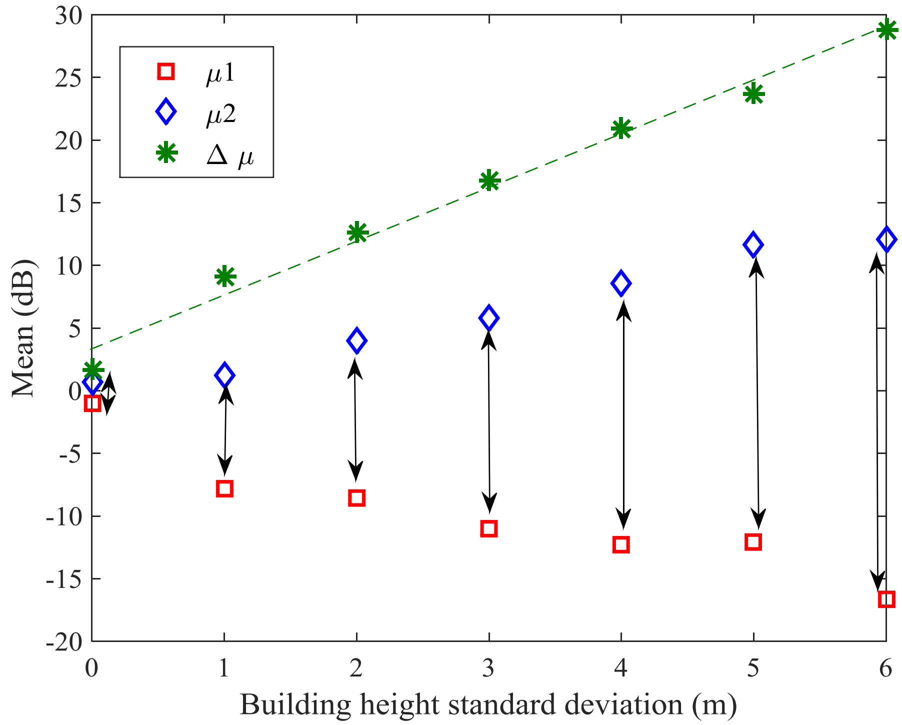

Figure 6-24: Variation of the GMM mean and separation parameter with building height variation.

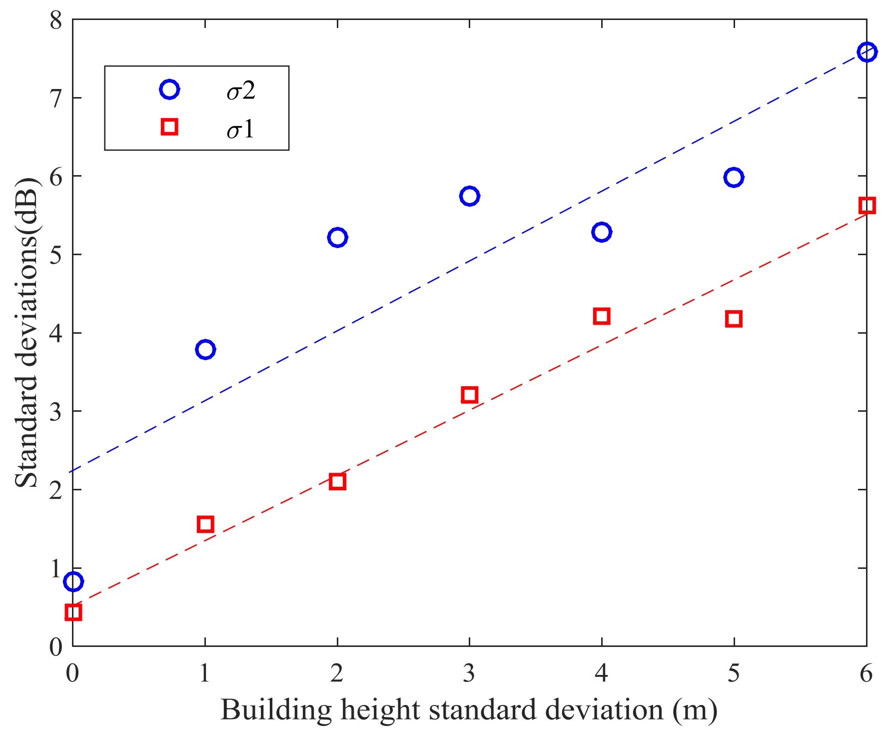

Figure 6-25: Variation of the GMM standard deviations with building height variation.

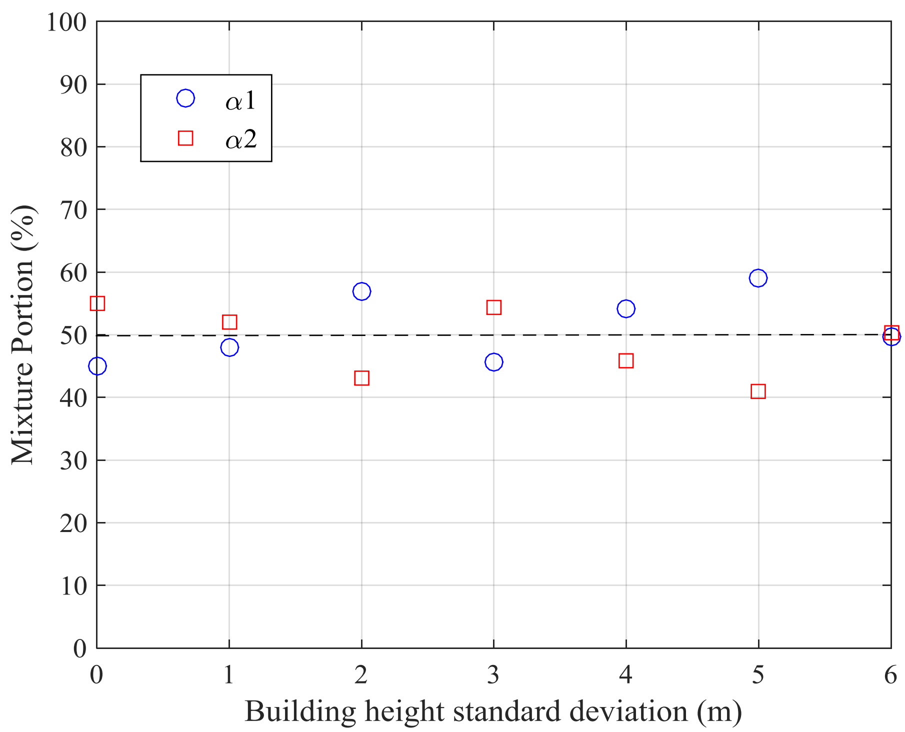

Figure 6-26: Portion in percentage for each of the modes in applied bimodal Gaussian distribution at mean building height.

Table 6-3: Separation of means relative to width in different building height standard deviation.

Standard deviation of building heights (m)	0	1	2	3	4	5	6
D	2.5	3.1	3.2	3.6	4.3	4.5	4.3

c. Correction factors

In order to generalize the results for any suburban environment with similar mean building height and variance, we obtain relative standard deviation of bimodal distribution at mean building height compared to Lognormal distribution at 2 m terminal height. These numbers can be used as correction factors to calculate bimodal parameters when area's typical shadowing standard deviation is known at low terminal heights and terminals are going to be deployed at mean building height. This is frequently encountered in many SG applications.

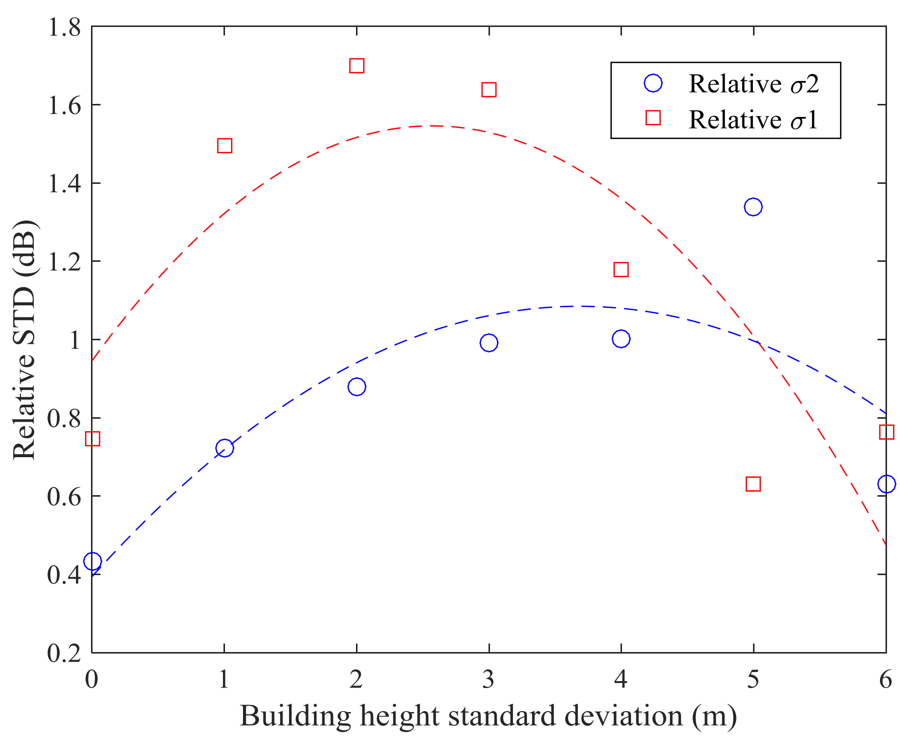

Figure 6-27: Relative standard deviation of GMM at mean building height to the standard deviation of Lognormal distribution at lower TS height (*i.e.*, 2 m).

6.4.4 Effect on System Edge and Area Coverage

As described in Section 6.3.2, large scale fading has direct impact on the coverage of the fixed wireless systems such that both edge and area coverages decreases with increasing the depth of shadowing. In this section, we use standard deviation of the equivalent Lognormal representation of SF distribution for different terminal heights, obtained in section 6.4.1, to show its impact on the coverage probabilities. It should be noted that here the calculation for coverage is only based on adequate received signal level. In practice outage can happen not only because of inadequate signal level but also inadequate signal to noise ratio. The presented results below are obtained for an area with mean building height and standard deviation and separation of 8 m, 3 m and 30 m, respectively and the parameter mentioned in Table 6-1. Figure 6-28 shows the coverage probability for both area and edge coverage at different heights.

Since the maximum depth of shadowing occures at mean building height, the coverage is most degraded compared to other heights at this height. This plot has important implication for designers who may not consider increase in depth of shadowing at terminal heights which recent deployments are occurring at and end up having a system with unexpected lower coverage. Similar results was driven in NIST document in which it was shown that having 6 dB difference in link budget may end up significant impact on coverage and required number of base stations to support a typical Smart Grid deployment scenario [4].

Figure 6-29 compares the radius of a system with 90% successful edge coverages at different terminal heights which was obtained using equation (6.20). Results imply that having terminal at higher heights will not necessarily increase the radius of successful coverages and terminals at the edge may even suffer more. The radius of the coverage area is minimum at mean building heights due to peak of the shadowing depth.

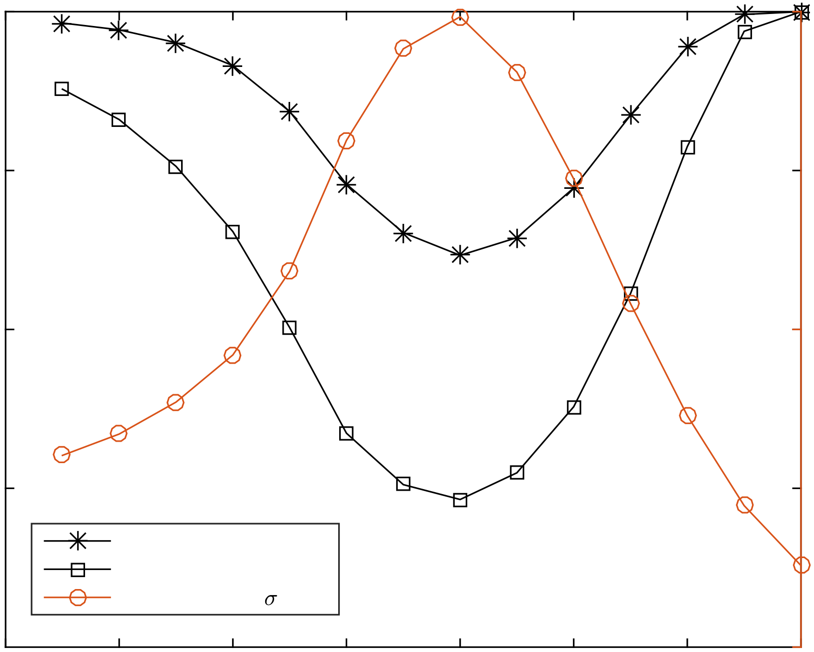

Figure 6-28: Impact of Shadow Fading behavior on Edge and Area Coverage.

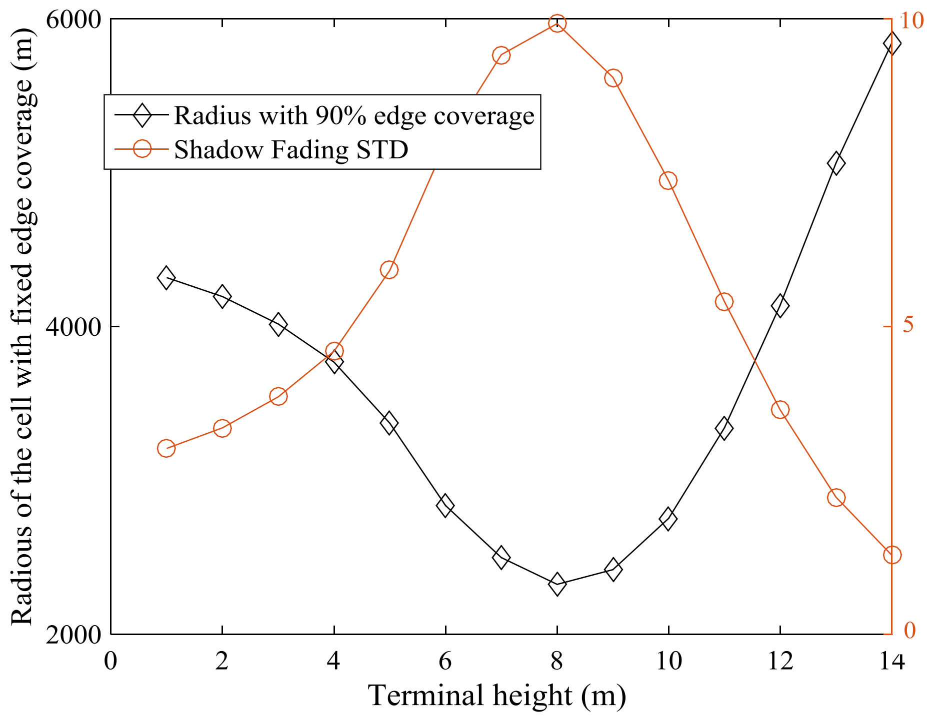

Figure 6-29: Impact of Shadow Fading behavior on the maximum radius of the system with 90% edge Coverage probability.

6.5 Discussion

While most path loss models for suburban macrocell environments report a steady decrease in mean path loss with increasing terminal height, corresponding models that capture the behavior of shadow fading with terminal height have not been previously reported. A handful of previously reported experimental results, including some collected by us, suggest that shadow fading actually increases until the terminal height reaches the mean building height then decreases rapidly thereafter. However, the results are anecdotal and cannot be easily generalized to other macrocell environments.

In order to reveal more general results, we applied a diffraction model using Fresnel-Kirchhoff integrals to a simulated suburban environment comprised of a large array of flat-roofed buildings with heights given by a normally distributed random variable. Our results revealed that:

1. While increasing the terminal height will reduce mean path loss, it will generally increase the depth of shadow fading such that the maximum shadow fading is observed when the terminal is at the mean building height and decreases as the terminal height rises or falls past this value. For an example in one instance of our simulations, the shadowing standard deviation increased from 3 dB to 10 dB when terminal was raised from 1 m to mean building height(8 m) and then decreased to around 1 dB at higher heights. Similar trend was observed as we changed the buildings mean height within the simulations.
2. The depth of shadow fading increases with the variance of the building heights. For the environment we simulated the peak of shadow fading was increased from 2.5 dB up to 12.5 dB when buildings height standard deviation was changed from 0 m to 5 m while the mean building height was kept fixed at 8 m.
3. When the terminal is well below mean building height, shadowing exhibits a Lognormal distribution but it was observed that it becomes less Lognormal as the terminal height increases and at the transition region which is the region around mean building height of the area, is best represented by a mixture. The effects of building heights mean and variance on parameter of the mixture distribution was also studied. For terminals located at mean building height, it was shown that although mean of GMM modes varies with areas mean building height; the distance between them remains unchanged. This distance was shown increases with building height variance. The standard deviation of each mode of fitted GMM

distribution was shown negligible changes (1 dB) when mean building height varies from 5 m-10 m, while it had increasing behavior with buildings height variance.

4. The behavior of depth of shadowing with terminal height have strong implications on efforts to predict system coverage and outage probabilities when user terminals or relays are elevated such that the benefits due to reduction in mean path loss with terminal height can be cancelled because of increase in shadowing and outage probability may increase unexpectedly. For example, considering the shadow fading variation from 1 dB-10 dB in different terminal heights, the system edge coverage was changed from 100% to 70% and the area coverage was changed from 100% to 85%, respectively, terminals at mean height having the lowest coverage.

In summary, considering the revealed behavior of the shadowing with terminal height will play a key role in designing the emerging SG wireless networks. Although further simulations and measurements are required and recommended to study of the effects of vegetation, non-flan roof top buildings and environment type, comparing measurement and simulation results suggests that the trend that we observed will be apparent, only details may be different.

As an extension for the current work, simulation of the shadow fading in the presence of foliage can give more realistic results. Moreover, other types of environments such as Urban area, can be considered by defining more complicated software simulation models which takes into account the reflection and street canyon effect as well. In our work the observed multimodal distribution of the shadowing was modelled and analyzed by Gaussian Mixture modeling (GMM) with two modes using expectation-maximization algorithms. However, further statistical studies with higher GMM modes or other mixture types, such as Weibull distributions, is recommended in order to model the shadowing distribution in other terminal heights and account for the skewness, *etc*.

Chapter 7:
Conclusions and Recommendations

7.1 Conclusions

The NIST Smart Grid framework wireless modeling tool has been created and populated by the Standards Setting Organizations which proposed their wireless technologies as candidates for the Smart Grid. It has been an effective tool for comparing the relative performance of different terrestrial wireless technologies and to provide initial estimates of network base station requirements to meet coverage, data density, and latency requirements in a wide range of deployment venues. However, there are some limitations we observed in the model which overcoming them can lead to more accurate cost/coverage estimations especially in NLOS Smart Grid deployment scenarios which deployment parameters differs from the conventional ones. Therefore, effective techniques for characterizing and simulating NLOS channels are required to support efficient implementation, deployment and operation of the new generation of wireless networks that support Smart Grid applications such as smart metering and distribution automation. In this thesis we have proposed some significant improvements to methods used to estimate small-scale channel parameters, characterize MIMO wireless channels, and simulate large scale parameters of wireless networks in suburban environments in order to reduce risk of over/under designing the related communication networks, thereby incurring unwanted expenses. The conclusive summary for each chapter of the thesis is as follows.

Previous work has given only limited consideration to the relationship between the Ricean distributions observed by sampling in the temporal, space, frequency and delay domains and the effect of noise and sampling on Ricean K-factor estimation in these domains. In Chapter 2, we proved the equivalence of the Ricean fading distributions observed in the delay, spatial and frequency domains and demonstrated the advantages of estimating the Ricean K-factor from channel frequency response data. More specifically we showed that the Ricean distributions observed in the space and frequency domains are equivalent. In addition, we revealed the relative impact of noise on K-factor estimation based upon data sampled in these domains. We concluded that estimation of K-factor is much easier based upon measurement of the scalar frequency response which can be collected more easily and are less susceptible to noise compared to those based upon measurements collected in the other domains such as delay domain which we showed how sensitive it can be to the selected noise threshold value. Moreover, using the equivalence of K factors in delay and frequency domains, we proposed a bisection algorithm for estimating the noise floor in measurement-based estimates that allows more accurate estimation of the delay spread. This reliable technique can be used for many applications such as on-site channel parameter estimation and revealing more accurate parameters by removing the uncertainties of detecting the true LOS and last multipath component from CIR when SNR or K-factor is low or Two-Wave with Diffuse Power (TWDP) or Hyper Rayleigh fading channel exist.

Although it is well known that one can estimate the channel impulse response from scalar frequency response data with sufficiently high Ricean K-factor using the Hilbert transform, many of the steps required to fully exploit this technique have not been previously revealed. In Chapter 3, using relationship between the Ricean K-factor associated with the scalar frequency response and the error in the estimated channel impulse response we developed a useful test using Ricean K-factor calculated from scalar response as the benchmark for determining whether a given scalar frequency response is suitable for processing using the Hilbert transform. We used channel K-factor, mean excess delay and RMS delay spreads as the error metrics and showed that when K is higher than 8 dB, the Hilbert estimation relative error for all of the selected error metrics will not exceed 10%. Effects of different SNR values on the amount of error increase at this threshold K-factor value were studied. We showed the amount of error one should expect when using Hilbert to estimate the above-mentioned channel parameters compared to when Hilbert is applied to a noise-free channel.

In Chapter 4, we revealed the manner in which the autocorrelation and cross correlation properties of LS codes degrade with decreasing the channel SNR and reduced bit resolution of the receiver ADC. This type of performance characterization of the LS codes is useful since knowing the level of degradation as the signal-to-noise ratio decreases helps the minimum transmit power level required to characterize the channel to be predicted accordingly when doing channel sounding. In this chapter we showed that under the effect of noise, LS sequences correlation DR reduces to finite value and the interference free window is no longer hold and the amount of reduction depends on the sequence length and channel SNR. Generally, LS sequences with longer length show more correlation DR and amount of DR reduction under noise is less compared to shorter sequences. According to our simulation, LS sequences which have been used in practice are resilient to noise up to 5-10 dB channel SNRs. Lowering SNR results in the performance reduction. Comparing these sequences with traditionally used PN sequences, noise-free LS sequences shows superior DR (both AC and CC) compared to PN sequences, but under certain channel SNR, their AC dynamic is comparable to PN sequence of the same length. However, LS sequences outperform PN considering its CC DR. Moreover, we showed that increasing receiver ADC bit resolution from 2 to 5 bits will increase DR values up to 10 dB but using an ADC with resolution of more than 5 bits will not improve the DR significantly. We concluded that ADC resolution has less effect on dynamic range of sequences compared to choosing proper family type and length of sequence and method of correlation. For example using periodic instead of aperiodic correlation we obtained significant improvement in dynamic range for the sample PN sequences that we used in our simulation. However, both types of correlation revealed very similar DR for LS sequences under different channel SNRs. The results in this chapter paved the path to design , implement and characterize a MIMO 2×2 channel sounder that uses LS sequences, as described in Chapter 5.

In Chapter 5, we showed how LS coded transmissions can be combined with our new technique of using fibre delay lines to permit a single channel receiver to effectively characterize multiple receiving antennas simultaneously to realize a particularly simple and effective dynamic MIMO channel sounder. In particular, we showed that the multi-channel receiver can be replaced by a single-channel receiver equipped with a set of fibre delay lines. This allows the responses from the array of receiving antennas to be stacked in time and observed with a much less expensive single-port correlation-based receiver. This overcomes the previous works limitation in measuring MIMO channel responses in fast varying environments where limited by many factors such as: cost, accuracy in non-stationary channels, and long duration of measurements. In addition, we proposed an efficient method of using fibre delay line to expand the channel sounder for higher number of MIMO schemes. We demonstrated the proposed concept along with required calibrations on a bench-top measurement setup in order to verify the noise floor prediction and study the added phase noise due to use of fibre delay line. Limitations of our channel sounder along with solutions to improve them were discussed. In summary the proposed channel sounder will outperform other commercial ones providing better Doppler range performance while having a comparable noise performance. Moreover, it will reduce large amount of hardware and labor cost for future measurement campaigns because of simpler receiver and shorter measurement time.

In Chapter 6, we demonstrated how shadow fading varies as a function of terminal height and building height distribution and the manner in which this affects the system link budget. While by intuition people may assume shadow fading decreases continuously as terminal antenna heights increases, according to our measurements and simulation results, its behavior is different which has significant implications on system's coverage. We showed that while mean path gain always tends to increase as terminal height increases, the depth of shadow fading reaches its maximum value when the terminal height approaches the area's mean building height. As the terminal height rises or falls past this value, the depth of shadow fading decreases. In addition, our results indicate that shadow fading follows a Lognormal distribution less and less closely as the terminal height increases. For terminals at mean building height, it's better represented by Gaussian Mixture model than Lognormal distribution. The parameters of this distribution with respect to area's building height variation were studied. We further showed that the above-mentioned effects can have a remarkable impact on the edge and area coverage of communication link and can cause one to overestimate the corresponding improvements in coverage when raising the terminals from ground level to the pole-top, and must therefore be accounted for in NLOS fixed wireless systems design.

7.2 Recommendations

In **Chapter 2 and 3**, we mainly simulated the Ricean propagation channel with maximum one specular component. Although this is the most common type of channel impulse responses seen in the practice, the applicability of the proposed techniques is recommended to be further investigated for two-wave with diffuse power which can produce a link worse than Rayleigh fading and are more likely happen in a system with terminal antennas statistically deployed near the ground or within structures such as underground tunnels. In **Chapter 3,** we obtained amount of increase in relative estimation error when Hilbert was used to estimate the channel K-factor, mean excess delay and RMS delay spreads within different channel SNRs while the channel K-factor was set to 8 dB. However, this evaluation can be extended to channels with other K-factors to generate a comprehensive error behavior of Hilbert in K-SNR plane. Other error metrics such as error of CIR amplitudes or phases correlation can be studies similar to what we did in this chapter.

The proposed channel sounder in **Chapter 5** was mainly focuses on MIMO 2by2**.** An extension and performance evaluation of the proposed technique for higher number of transmitter and receiver antennas is recommended. However, it can be challenging to record the responses of the large number of MIMO antennas or channels with large maximum excess delay within one snapshot. This is mainly because of narrow Interference Free Window zone that LS sequences can provide. A possible method for overcoming this problem is to find another family of the sequences with larger IFW zone. Moreover, LS sequences that was studied in **Chapter 4**, has been shown not to be energy efficient. More dynamic range under noisy channels can be achieved using energy efficient type of sequences.

The results presented in **Chapter 6** are based on measurement and simulation results from typical suburban environment with flattop buildings and ignore the effect of foliage. As an extension for the current work, simulation of the shadow fading in presence of foliage can give more realistic results. Moreover, other types of environments, such as urban areas, can be considered by defining more complicated software simulation models that takes into account the reflection and street canyon effect as well. In our work the observed multimodal distribution of the shadowing was modelled and analyzed by Gaussian Mixture modeling (GMM) with two modes using expectation-maximization algorithms. However, further statistical studies with higher GMM modes or other mixture types such as Weibull distributions are recommended in order to model the shadowing distribution in other terminal heights and account for the skewness, *etc.*

References

[1] The National Institute of Standards and Technology (NIST) Framework and Roadmap for Smart Grid Interoperability Standard [Online]. Available: http://www.nist.gov/smartgrid/, visited on Oct. 2014.

[2] U.S Department of Energy, National Energy Technology Laboratory (NETL) [Online]. Available: http://www.netl.doe.gov/smartgrid, visited on Oct. 2015.

[3] Electric Power Research Institute (EPRI), [Online]. Available: http://smartgrid.epri.com/Comms.aspx, visited on Feb. 2016.

[4] "NIST Smart Grid Interoperability Panel Priority Action Plan 2: Guidelines for assessing wireless standards for smart grid applications," National Institute of Standards and Technology, NISTIR 7761 Rev. 1, June 2014.

[5] "PAP02: Wireless Communications for the Smart Grid v2.0," [Online]. Available : http://collaborate.nist.gov/twiki-sggrid/bin/view/SmartGrid/PAP02Wireless. visited on Dec. 2015.

[6] Y. Yan, Y. Qian, H. Sharif, and D. Tipper, "A survey on Smart Grid communication infrastructures: Motivations, requirements and challenges," *IEEE Commun. Surv. Tutorials,* vol.15, no.1, pp. 5-20, 2013.

[7] S. Guzelgoz, H. Arslan, A. Islam, and A. Domijan, "A review of wireless and PLC propagation channel characteristics for smart grid environments," *J. of Elect. and Comput. Eng.*, Aug. 2011.

[8] L. Zheng, and D. Tse, "Diversity and multiplexing: a fundamental tradeoff in multiple-antenna channels," *IEEE Trans. Inf. Theory,* vol. 49, no.5, pp. 1073-1096, May 2003.

[9] D. Gesbert, M. Shafi, S. Da-shan, P. J. Smith, and A. Naguib, "From theory to practice: an overview of MIMO space-time coded wireless systems," *IEEE J. Sel. Areas Commun,* vol. 21, no. 3, pp. 281-302, Apr 2003.

[10] Y. Chen, and N. C. Beaulieu, "Maximum likelihood estimation of the K factor in Ricean fading channels," *IEEE Commun. Lett.* , vol. 9, no. 12, pp. 1040-1042, Dec. 2005.

[11] L. J. Greenstein, D. G. Michelson, and V. Erceg, "Moment-method estimation of the Ricean K-factor," *IEEE Commun. Lett.*, vol. 3, no. 6, pp. 175– 176, June 1999.

[12] A. Abdi, C. Tepedelenlioglu, M. Kaveh, and G. Giannakis, "On the estimation of the K parameter for the Rice fading distribution," *IEEE Commun. Lett.*, vol. 5, pp. 92- 94, Mar.

2001.

[13] C. Tepedelenlioglu, A. Abdi, and G. Giannakis, “The Ricean K factor: estimation and performance analysis,” *IEEE Trans. Commun.*, vol. 2, pp. 799–809, July 2003.

[14] K. Witrisal, K. Yong-Ho, and R. Prasad, “A new method to measure parameters of frequency-selective radio channels using power measurements,” *IEEE Trans. Commun.*, vol. 49, no. 10, pp. 1788,1800, Oct 2001.

[15] B. P. Donaldson, M. Fattouche, and R. W. Donaldson, “Characterization of in-building UHF wireless radio communication channels using spectral energy measurements,” *IEEE Trans. Antennas Propag.* , vol.44, no.1, pp.80-86, Jan 1996.

[16] J. H. Choi, H. K. Chung, H. Lee, J. Cha and H. Lee, “Code-Division multiplexing based MIMO channel sounder with Loosely Synchronous codes and Kasami codes,” in *Proc. IEEE VTC*, pp. 1,5, 25-28 Sep. 2006.

[17] K. Kuroda, K. Sakaguchi, J. I. Takada, and K. Araki, “FDM based MIMO spatio-temporal channel sounder,” *IEEE Pers. Commun. Symp.*, vol. 2, pp. 559-562 vol.2, 27-30 Oct. 2002.

[18] W. Ciccognani, A. Durantini, and D. Cassioli, “Time domain propagation measurements of the UWB indoor channel using PN-sequence in the FCC-compliant band 3.6–6 GHz,” *IEEE Trans. Antennas Propag.*, vol. 53, no. 4, pp. 1542–1549, Apr. 2005.”

[19] J. B. Anderson, “Antenna arrays in mobile communications: gain, diversity, and channel capacity,” *IEEE Antennas Propag. Mag.*, vol. 42, no. 2, pp. 12- 16, April 2000.

[20] S. C. Kim, H. L. Bertoni, and M. Stern, “Pulse propagation characteristics at 2.4 GHz inside buildings,” *IEEE Trans. Veh. Technol.*, vol. 45, pp. 579–592, Aug. 1996.

[21] A. F. Molisch and F. Tufevsson, “Propagation channel models for next- generation wireless communications systems,” *IEICE Trans. Commun.*, vol. 97, no. 10, pp. 2022–2034, 2014.

[22] S. Salous, P. Filippidis, R. Lewenz, I. Hawkins, N. Razavi-Ghods, and M. Abdallah, “Parallel receiver channel sounder for spatial and MIMO characterisation of the mobile radio channel,” *Proc. IEEE Commun.*, vol. 152, no. 6, pp. 912-918, Dec. 2005.

[23] L. Welch, “Lower bounds on the maximum cross correlation of signals,” *IEEE Trans. Inf. Theory* , vol. 20, no. 3, pp. 397-399, May 1974.

[24] M. Kim, S. Kim, H. Lee, H. Lee, and H. You, “Performance comparison of some codes in

code division multiplexing based MIMO channel sounder architecture," in *Proc. IEEE ICACT*, vol. 2, no., pp. 1343,1346, Feb. 2008.

[25] P. Nobles and F. Halsall, "Delay spread measurements within a building at 2 GHz, 5 GHz and 17 GHz," in *Proc. Inst. Elect. Eng. Colloq*., pp. 1–6, Oct. 1996.

[26] K. G. Tan, and T. A. Rahman, "Receiving antenna height dependence of radio propagation path loss in fixed wireless access environment," in *Proc. IEEE Microw.*, vol. 3, pp. 797-800 vol.3, 1999.

[27] V. S. Abhayawardhana, I. J. Wassell, D. Crosby, M. P. Sellars, and M.G. Brown, "Comparison of empirical propagation path loss models for fixed wireless access systems," in *Proc. IEEE VTC*, vol. 1, pp. 73-77, April 2005

[28] S. Majedi, and F. Farzaneh, "A new empirical-physical method for calculation of path loss for fixed wireless access in suburban areas," *IEEE IST Symp.* , vol., no., pp. 92-96, Aug. 2008.

[29] K. G. Tan, and T. A. Rahman, "The effect of receiving antenna height on temporal fading characteristics in fixed-to-fixed radio propagation channel," in *Proc. IEEE Microw.*, vol. 3, pp. 801-804, 1999.

[30] J. W. Porter, J. A. Thweatt, "Microwave propagation characteristics in the MMDS frequency band," in *Proc. IEEE ICC*, vol. 3, pp. 1578-1582, Jun. 2000.

[31] J. Nasreddine, J. Riihijärvi, A. Achtzehn, and P. Mähönen, "The world is not flat: Wireless communications in 3D environments," *IEEE International Symposium on a World of Wireless, Mobile and Multimedia Networks*, Spain, June 2013.

[32] D. Greenwood, and L. Hanzo, *Characterization of mobile radio channels*, R. Steele, Ed. London, U.K., Pentech, 1992, pp. 92–185.

[33] S. Catreux, V. Erceg, D. Gesbert, and R. W. Heath, "Adaptive modulation and MIMO coding for broadband wireless data networks," *IEEE Commun. Mag*., vol. 40, no. 6, June pp. 108–115, 2002.

[34] M. D. Austin and G. L. Stüber, "Velocity adaptive handoff algorithms for microcellular systems," *IEEE Trans. Veh. Technol*., vol. 43, no. 3, pp. 549–561, Aug. 1994.

[35] W. C. Y. Lee, "Estimate of local average power of a mobile radio signal," *IEEE Trans. Veh. Technol.*, vol. 34, no. 1, pp. 22–27, Feb. 1985.

[36] S. Salous, *Radio Propagation Measurement and Channel Modelling*, Wiley, 2013, ch. 4.

[37] K. Talukdar and W. Lawing, “Estimation of the parameters of the Rice distribution,” *J. Acoust. Soc. Am.*, vol. 89, no. 3, pp. 1193–1197, Mar. 1991.

[38] P. K. Rastogi and O. Holt, “On detecting reflections in presence of scattering from amplitude statistics with application to D region partial reflections,” *J. Radio Sci*., vol. 16, pp. 1431–1443, 1981

[39] A. O. Kaya, L. J. Greenstein and W. Trappe, "Characterizing indoor wireless channels via ray tracing combined with stochastic modeling," *IEEE Trans. Wireless Commun.*, vol. 8, no. 8, pp. 4165-4175, Aug. 2009.

[40] A. N. Morabito, D. B. Percival, J. D. Sahr, Z. M. P. Berkowitz and L. E. Vertatschitsch, "Ricean parameter estimation using phase information in low SNR environments," *IEEE Commun. Lett.*, vol. 12, no. 4, pp. 244-246, Apr. 2008.

[41] V. Erceg, D. G. Michelson, S. S. Ghassemzadeh, L. J. Greenstein, A. J. Rustako, P. B. Guerlain, M. K. Dennison, R. Roman, D. J. Barnickel, S. C. Wang, and R. R. Miller, "A model for the multipath delay profile of fixed wireless channels," *IEEE J. Sel. Areas Commun*., vol. 17, no. 3, pp. 399,410, Mar. 1999.

[42] A. Paier , J. Karedal , N. Czink , C. Dumard , T. Zemen , F. Tufvesson , A. Molisch and C. F. Mecklenbräuker "Characterization of vehicle-to-vehicle radio channels from measurements at 5.2 GHz", *Wireless Pers. Commun.*, vol. 50, no. 1, pp. 19 -32, 2009.

[43] J. P. Rossi, "Influence of measurement conditions on the evaluation of some radio channel parameters," *IEEE Trans. Veh, Technol.*, vol. 48, no. 4, pp. 1304-1316, Jul 1999.

[44] T. Zwick, T. J. Beukema, and H. Nam, "Wideband channel sounder with measurements and model for the 60 GHz indoor radio channel," *IEEE Trans. Veh. Technol.*, vol. 54, no. 4, pp. 1266-1277, July 2005.

[45] K. Takamizawa, S. Y. Seidel, and T. S. Rappaport, "Indoor radio channel models for manufacturing environments," in *Proc. IEEE Energy Inform. Technol.*, vol. 2, pp. 750-754, Apr. 1989.

[46] T. S. Rappaport and S. Y. Seidel, “900 MHz multipath propagation measurements for U.S. digital cellular radiotelephone,” *IEEE Trans. Veh. Technol.*, vol. 39, pp. 132–139, May 1990.

[47] A. Hammoudeh, D. A. Scammell, and M. G. Sanchez, "Measurements and analysis of the indoor wideband millimeter wave wireless radio channel and frequency diversity

characterization," *IEEE Trans. Antennas Propag.*, vol. 51, no. 10, pp. 2974-2986, Oct. 2003.

[48] Z. Min, W. Muqing, S. Yanzhi, Y. Deshui, D. Shiping, Z. Panfeng, Z. Xiangbing, and G. Shuyun, "Analysis and Modeling for Train-Ground Wireless Wideband Channel of LTE on High-Speed Railway," in *Proc. IEEE VTC*, pp. 1-5, June 2013.

[49] Y. He, M. Wu, M. Zhao, S. Di, S. Ge, and X. Li, "A MIMO Channel Measurement Method Based on Optimum m-Sequence Pairs," in *Proc. IEEE WiCOM*, pp. 1-4, Sep. 2012.

[50] T. Zhou, C. Tao, L. Liu and Z. Tan, "Ricean K-factor measurements and analysis for wideband radio channels in high-speed railway U-shape cutting scenarios," in *Proc. IEEE VTC*, pp. 1-5, May 2014.

[51] L. Liu, "Position-Based Modeling for wireless channel on high-speed railway under a viaduct at 2.35 GHz," in *IEEE J. Sel. Areas Commun.*, vol. 30, no. 4, pp. 834-845, May 2012.

[52] D. M. Krizman, B. J. Ellison, and T. S. Rappaport, "Modeling and simulation of narrowband phase from the wideband channel impulse response," in *Proc. IEEE VTC*, vol. 1, pp. 67-71, May 1997.

[53] T. S. Rappaport, *Wireless Communications: Principles and Practice*, Prentice Hall, 1996.

[54] A. Papoulis, *Probability, Random Variables, and Stochastic Processes,*1st ed., McGraw-Hill, 1965.

[55] R. H. Clarke, “A statistical theory of mobile-radio reception,” *Bell Syst. Tech. J.*, vol. 47, pp. 957-1000, Aug. 1968.

[56] D. de la Vega, S. Lopez, J. M. Matías, U. Gil, I. Pena, M. Ma Velez, J. L. Ordiales, and P. Angueira, "Generalization of the Lee Method for the Analysis of the Signal Variability," *IEEE Trans. Veh. Technol.*, vol. 58, no. 2, pp. 506-516, Feb. 2009.

[57] A. F. Molisch and M. Steinbauer, “Condensed parameters for characterizing wideband mobile radio channels”, *J. Wireless Inform. Networks*, vol. 6, pp. 133-154, July 1999.

[58] P. Peebles, Probability, *Random Variables and Random Signal Principles*, 4th ed., Singapore, McGraw-Hill, 2001, pp. 81-82.

[59] P. Vandenameele, *Space Division Multiple Access for Wireless Local Area Networks*, MA, Kluwer Academic, 2001.

[60] J. Hansen, "An analytical calculation of power delay profile and delay spread with experimental verification," *IEEE Commun. Lett.*, vol. 7, no. 6, pp. 257-259, June 2003.

[61] M. Jeruchim, P. Balaban, and K. Shanmugan, *Simulation of Communication Systems*, 2nd ed., New York, Kluwer Academic, 2000.

[62] N.V. Smirnov, "Approximate distribution laws for random variables, constructed from empirical data" *Uspekhi Mat. Nauk* , vol. 10, pp. 179–206, 1944.

[63] R. P. Millane, "Phase retrieval in crystallography and optics," *J. Opt. Soc. Am.* vol. 7 pp. 394–411, 1990.

[64] J. C. Dainty, and J. R. Fienup, *Phase retrieval and image reconstruction for astronomy*, in H. Stark, Editor, *Image Recovery: Theory and Application*, New York, Academic Press, 1987.

[65] O. Bunk, A. Diaz, F. Pfeiffer, C. David, B. Schmitt, D. K. Satapathy, and J. F. van der Veen, "Diffractive imaging for periodic samples: retrieving one-dimensional concentration profiles across microfluidic channels," *Acta Cryst*. Vol. 63, 306– 314, 2007.

[66] A. Walther, "The question of phase retrieval in optics," *Opt. Acta,* vol.10 pp. 41–49, 1963.

[67] J. R. Fienup, "Phase retrieval algorithms: A comparison," *Applied Optics J.*, vol. 21, no. 15, pp. 2758–2768, 1982.

[68] H. Hauptman, "The direct methods of X-ray crystallography," *AAAS J.*, vol. 233, no. 4760, pp. 178–183, Jul. 1986.

[69] J. L. C. Sanz, "Mathematical considerations for the problem of Fourier transform phase retrieval from magnitude," *SIAM J. Appl. Math*., vol. 45, no. 4, pp. 651–664, 1985.

[70] R. W. Gerchberg and W. O. Saxton, "A practical algorithm for the determination of phase from image and diffraction plane pictures," *Optik J.*, vol. 35, no. 2, pp. 237–246, Nov. 1972.

[71] E. Candes, T. Strohmer, and V. Voroninski, "PhaseLift: Exact and stable signal recovery from magnitude measurements via convex programming," *Comm. Pure Appl. Math*., pp. 1241–1274, 2013.

[72] M. H. Hayes, J. S. Lim, and A. V. Oppenheim, "Signal reconstruction from phase or magnitude," *IEEE Trans. Acoust., Speech Signal Process.*, vol. 28, no. 6, pp. 672-680, Dec. 1980.

[73] A. Bayram, A. M. Attiya, and A. Safaai-Jazi, "Frequency-domain measurement of indoor

UWB channels," *Microw. Opt. Technol. Lett.*, vol.44, no. 2, pp. 118–123, Jan. 2005.

[74] A. H. Muqaibel, "Measurements of UWB through-the-wall propagation using spectrum analyzer and the Hilbert transform," *Microw. Opt.Technol. Lett*., vol. 50, no. 2, pp. 465–470, Feb. 2008.

[75] I. Páez, S. Loredo, L. Valle, and R. P. Torres, "Experimental estimation of wideband radio channel parameters with the use of a spectrumanalyzer and the Hilbert transform," *Microw. Opt. Technol. Lett.*, vol.34, no. 5, pp. 393–397, Sep. 2002.

[76] D. Granados-Lieberman, M. Valtierra-Rodriguez, L. A. Morales-Hernandez, R. J. Romero-Troncoso, and R. A. Osornio-Rios, "A Hilbert transform-based smart sensor for detection, classification, and quantification of power quality disturbances," *J. Sensors*, vol. 13, no. 5, pp. 5507–5527, Apr. 2013.

[77] N. Suljanovi, A. Mujčić, M. Zajc and J. Tasič "Approximate computation of high-frequency characteristics for power line with horizontal disposition and middle-phase to ground coupling," *Elsevier J. Elect. Power Syst.*, vol. 69, pp. 17-24, Apr. 2004.

[78] A. Carballar, and M. A. Muriel, "Phase reconstruction from reflectivity in fibre Bragg gratings," *J. Lightwave Technol.*, vol. 15, no. 8, pp. 1314-1322, Aug. 1997.

[79] M. J. Erro , I. Arnedo , M. A. G. Laso , T. Lopetegui and M. A. Muriel, "Phase-reconstruction in photonic crystals from S-parameter magnitude in microstrip technology", *Opt. Quantum Elect.*, vol. 39, no. 4, Feb. 2007.

[80] D. Cassioli, and A. Mecozzi, "Minimum-phase impulse response channels," *IEEE Trans. Commun.*, vol. 57, no. 12, pp. 3529-3532, Dec. 2009.

[81] D. R. Morgan, "Adaptive multipath cancellation for digital data communications," *IEEE Trans Commun*, vol. 26, no . 9, pp.1380-1390, Sep.1978.

[82] P. Perry and T. J. Brazil, Hilbert-transform-derived relative group delay, *IEEE Trans. Microw. Theory*, vol. 45, 1214-1225, 1977.

[83] B. Hassibi, T. Kailath, A. H. Sayed, *Linear estimation* Englewood Cliffs, N.J., Prentice Hall, 2000, p. 193.

[84] S. Loredo, G. León, S. Zapatero, and F. Las-Heras, "Measurement of low-gain antennas in non-anechoic test sites through wideband channel characterization and echo cancellation," *IEEE Antennas Propag. Mag*., vol. 51, no. 1, pp. 128–135, Feb. 2009.

[85] Y. Yang, G. Xu, and H. Ling, "An experimental investigation of wideband MIMO

channel characteristics based on outdoor Non-LOS measurements at 1.8 GHz," *IEEE Trans. Antennas and Propag.*, vol. 54, no. 11, pp. 3274-3284, Nov. 2006.

[86] G. S. Dahman, R. J. C. Bultitude, and R. H. M. Hafez, "The use of frequency-orthogonal pseudonoise (FOPN) sounding signals for identifying transmissions from different transmit antennas," *IEEE Antennas Propag. Lett*., vol. 8, pp. 657-660, 2009.

[87] C. Garcia-Pardo, J. Molina-Garcia-Pardo, and L. Juan-Llacer, "Time-domain MIMO channel sounder based on code-division multiplexing," *IEEE Trans. Instrum. Meas.*, vol. 61, no. 8, pp. 2325,2327, Aug. 2012.

[88] E. Garcia, J. A. Paredes, F. J. Alvarez, M. C. Perez and J. J. Garcia, "Spreading sequences in active sensing: A review," *Elsevier J. Signal Process*., vol. 106 , pp. 88 -105 , 2015.

[89] A. Mitra, "On pseudo-random and orthogonal binary spreading sequences," *IJITM J.*, vol. 4, no. 2, Apr. 2008.

[90] V. Kolmonen, P. Almers, J. Salmi, J. Koivunen, K. Haneda, A. Richter, F. Tufvesson, A. F. Molisch, and P. Vainikainen, "A dynamic dual-Link wideband MIMO channel sounder for 5.3 GHz," *IEEE Trans. Instrum. Meas.*, vol. 59, no. 4, pp. 873,883, Apr. 2010.

[91] X. Zeng, J. Q. Liu, and L. Hu, "Generalized Kasami sequences: The large set," *IEEE Trans. Inform. Theory,* vol. 53, no. 7, pp. 2587-2598, July 2007.

[92] T. Kasami, "Weight distribution formula for some class of cyclic codes," University of Illinois, Urbana, Rept. R-265, Apr. 1966.

[93] R. Gold, "Maximal recursive sequences with 3-valued recursive cross-correlation functions (Corresp.)," *IEEE Trans. Inform. Theory*, vol. 14, no. 1, pp. 154-156, Jan. 1968.

[94] E. H. Dinan, and B. Jabbari, "Spreading codes for direct sequence CDMA and wideband CDMA cellular networks," *IEEE Commun. Mag.*, vol. 36, no. 9, pp. 48-54, Sep. 1998.

[95] M. Soltanalian, and P. Stoica, "Computational design of sequences with good correlation properties," *IEEE Trans. Signal Process.*, , vol. 60, no. 5, pp. 2180-2193, May 2012.

[96] M. Darnell, and A. H. Kemp, "Synthesis of multilevel complementary sequences," *IEEE Lett*. vol. 24, no. 19, pp. 1251–1252, Sep. 1988.

[97] M. Darnell, "Multi-level signals with good autocorrelation properties," *in Proc. IEEE ICCA*, vol. 1, pp. 562–566, 1991.

[98] V. I. Levenshtein, "New lower bounds on aperiodic cross correlation of binary codes,", in *Proc. IEEE Inform. Theory*, pp. 471,, 16-21 Aug 1998.

[99] X. H. Tang, P. Z. Fan, and S. Matsufuji, “Lower bounds on the maximum correlation of sequence set with low or zero correlation zone,” *IEE Lett.*, vol. 36, pp. 551–552, Mar. 2000.

[100] D. Sarwate, “Bounds on cross correlation and autocorrelation of sequences,” *IEEE Trans. Inf. Theory*, vol. 25, pp. 720–724, 1979.

[101] X. Deng, and P. Fan, “Spreading sequence sets with zero correlation zone,” *IEEE Lett*. vol. 36, no. 11, pp. 993–994, May 2000.

[102] A. Appuswamy, and A. K. Chaturvedi, “A new framework for constructing mutually orthogonal complementary sets and ZCZ sequences,” *IEEE Trans. Inf. Theory*, vol. 52, no. 8, pp. 3817–3826, Aug. 2006.

[103] X. Tang, P. Fan, and J. Lindner, “Multiple binary ZCZ sequence sets with good cross-correlation property based on complementary sequence sets,” *IEEE Trans. Inf. Theory*, vol. 56, pp. 4038–4045, Aug. 2010.

[104] Q. K. Trinh, P. Fan, and E. M. Gabidulin, “Multilevel Hadamard matrices and zero correlation zone sequences,” *IEEE Lett.* vol. 42, no. 13, pp. 748–750, June 2006.

[105] P. Ke, S. Zhang, and F. Lin, “Constructions of binary array set with zero-correlation zone,” *Elsevier J. Inform. Sci.*, vol. 197, pp. 197-206, Aug. 2012.

[106] D. Li, ‘The perspectives of large area synchronous CDMA technology for the fourth-generation mobile radio,” *IEEE Commun. Mag.*, vol. 41, no. 3, pp. 114–118. Mar. 2003.

[107] C. Garcia-Pardo, J. Molina-Garcia-Pardo, J. V. Rodríguez, and L. Juan-Llacer, "Comparison between time and frequency domain MIMO channel sounders," in *Proc. IEEE VTC*, pp.1-5, pp. 6-9 Sep. 2010.

[108] M. H. Ullah, M. T. Islam, M. Sing, R. Nordin and B. Bais, “Design of transmitter for CDM based 2×2 multiple input multiple output channel sounder for multipath delay measurement,” *Am. J. Applied Sci*., vol. 9, no. 1, pp. 117-122, 2012.

[109] S. Stanczak, H. Boche, and M. Haardt, “Are LAS-codes a miracle?,” in *Proc. IEEE GLOBECOM*, vol. 1, pp. 589–593, Nov. 2001.

[110] X. Tang, and W. H. Mow, “Design of spreading codes for quasi-synchronous CDMA with intercell interference,” *IEEE J. Sel. Areas Commun*., vol. 24, pp. 84–93, 2006.

[111] S. Ni, H. Wei, J. S. Blogh, and L. Hanzo, "Network performance of asynchronous UTRA-like FDD/CDMA systems using loosely synchronised spreading codes," in *Proc. IEEE*

VTC, vol. 2, pp. 1359-1363, Oct. 2003.

[112] R. L. Cooper, and D. D. Stancil, "Improved channel sounding using zero correlation zone sequences," in *Proc. IEEE GLOBECOM*, pp.1-6, Dec. 2009.

[113] J. K. Kayani, and S. F. Russell, *Implementation of self-noise suppression techniques for ultrasonic correlation systems*, in D. Thompson, Editor, *Review of Progress in Quantitative Nondestructive Evaluation*, New York, Plenum Press Div Plenum Publishing Corp, 1997.

[114] M. C. Pérez, J. Urena, A. Hernández, A. Jimenez, D. Ruiz, F. J. Alvarez, and C. De Marziani, "Performance comparison of different codes in an ultrasonic positioning system using DS-CDMA," in *Proc. IEEE WISP*, pp. 125-130, Aug. 2009.

[115] P. C. Fannin, A. Molina, S. S. Swords, and P. J. Cullen, "Digital signal processing techniques applied to mobile radio channel sounding," in *Proc. IEE Radar Signal Process.*, vol. 138, no. 5, pp. 502-508, Oct. 1991.

[116] H. K. Chung, N. Vloeberghs, H. K. Kwon, S. J. Lee and K. C. Lee, "MIMO channel sounder implementation and effects of sounder impairment on statistics of multipath delay spread," in *Proc. IEEE VTC*, pp. 349-353, Sep. 2005.

[117] D. Li, “LAS-CDMA,” *Tech. Rep.*, Third Generation Partnership Project 2, CWTS, WG-1, Apr. 2000.

[118] M. J. E. Golay, “Complementary series,” *IRE Trans. Inf. Theory*, vol. 7 pp. 82–87, 1961.

[119] M. J. E. Golay, “Note on complementary series,” in *Proc. IRE*, vol. 84, Jan. 1962.

[120] S. Eliahou, M. Kervaire, and B. Saffari, “A new restriction on the lengths of golay complementary sequences,” *Elsevier J. Combinatorial Theory*, vol. 55, pp. 49–59, 1990.

[121] Y. Taki, H. Miyakawa, M. Hatori, and S. Namba, “Even-shift orthogonal sequences,” *IEEE Trans. Inf. Theory*, vol. 15, pp. 295–300, 1969.

[122] P. Fan, “Spreading sequence design and theoretical limits for quasi-synchronous CDMA systems,” *EURASIP J. Wireless Commun. Network.*, pp. 19-31, Jan. 2004.

[123] J. Parsons, *The mobile radio propagation channel*, John Wiley & Sons, 2000.

[124] SMW200A Vector Signal Generator Manual, Rohde& Schwarz, [Online]. Available: https://www.rohde-schwarz.com/in/product/smw200a-productstartpage_63493-38656.html, visited on July 2015.

[125] S. W. Golomb, *Shift Register Sequences, Laguna Hills*, CA, Aegean Park Press, 1981.

[126] G. M. Naidu, O. Sudhakar, and V. Sailaja, “Simulation of BPSK modulation and demodulation on system generator,” *IJSER J.* , vol. 1, no. 2, Oct. 2013.

[127] S. O. Popescu, A. S. Gontean, and G. Budura, "Simulation and implementation of a BPSK modulator on FPGA", in *Proc. IEEE SACI*, pp. 459-463, May 2011.

[128] S. Salous, *Radio propagation measurement and channel modelling*, Wiley, 2013.

[129] D. Cox, “Delay Doppler characteristics of multipath propagation at 910 MHz in a suburban mobile radio environment,” *IEEE Trans. Antennas Propag.*, vol.20, no. 5, pp. 625-635, Sep. 1972.

[130] R. C. Dixon, *Spread Spectrum Systems with Commerical Applications*, John Wiley & Sons, 1994.

[131] R. J. Pirkl, and G. D. Durgin, “Optimal sliding correlator channel sounder design,” *IEEE Trans Wireless Commun.*, vol. 7, no. 9, pp. 3488-3497, Sep. 2008.

[132] M. Hamalainen, A. Nykanen, V. Hovinen, and P. Leppanen, “Digital stepping correlator in a wideband radio channel measurement system,” in *Proc. IEEE PIMRC*, vol. 3, pp. 1120-1124, Sep 1997.

[133] Y. Chen, Z. Zhang, and V. K. Dubey, “Effect of antenna directivity on angular power distribution at mobile terminal in urban macrocells: A geometric channel modeling approach,” *IEEE Wireless Pers. Commun.*, vol. 43, no. 2 ,Oct. 2007.

[134] MEDAV, RUSK Channel Sounder, [Online]. Available: http://www.channelsounder.de, visited on Dec. 2015.

[135] B. T. Maharaj, L. P. Linde, J. W. Wallace and M. A. Jensen,“A cost-effective wideband MIMO channel sounder and initial co-located 2.4 GHz and 5.2 GHz measurements,” in *Proc. IEEE ICASSP*, pp. 981–984, Mar. 2005.

[136] D. Baum and H. Bolcskei, “Impact of phase noise on MIMO channel measurement accuracy,” in *Proc. IEEE VTC*, vol. 3, pp. 1614–1618, Sep. 26–29, 2004.

[137] M. Steinbauer, A. F. Molisch and E. Bonek, "The double-directional radio channel," *IEEE Antennas Propag. Mag.*, vol. 43, no. 4, pp. 51-63, Aug 2001.

[138] R. W. Lorenz, and G. Kadel, "Diversity measurement technique for wideband mobile radio," in *Proc. IEEE GLOBECOM* , vol. 2, pp. 1237-1241, Dec. 1993.

[139] G. Kadel, "Measurement of wideband micro- and macro-diversity characteristics of the mobile radio channel," in *Proc. IEEE VTC*, vol. 1, pp. 165-169, June 1994.

[140] M. Habib Ullah and A. Unggul Priantoro, “A review on multiplexing schemes for MIMO channel sounding,” in *Proc. IEEE IJCSNS*, vol. 9, no. 6, pp. 294–300, Jun. 2009.

[141] A. Taparugssanagorn and J. Ylitalo, "Characteristics of short-term phase noise of MIMO channel sounding and its effect on capacity estimation," *IEEE Trans. Instrum. Meas.*, vol. 58, no. 1, pp. 196-201, Jan. 2009.

[142] V. M. Kolmonen, J. Kivinen, L. Vuokko, and P. Vainikainen, "5.3 GHz MIMO radio channel sounder," in *Proc. IEEE IMTC*, vol. 3, pp. 1883-1888, May 2005.

[143] J. Kivinen and P. Vainikainen, “Phase noise in a direct-sequence-based channel sounder,” in *Proc. IEEE PIMRC*, vol. 3, pp. 1115–1119, Sep. 1997.

[144] P. Almers, S. Wyne, F. Tufvesson, and A. F. Molisch, “Effect of random- walk phase noise on MIMO measurements,” in *Proc. IEEE VTC*, vol. 1, pp. 141–145, May 2005.

[145] J. Rutman, "Characterization of phase and frequency instabilities in precision frequency sources: Fifteen Years of Progress," in *Proc. IEEE*, vol. 66, pp. 1048-1075, 1978.

[146] A. Taparugssanagorn, J. Ylitalo and B. H. Fleury, "Phase-noise in TDM-switched MIMO channel sounding and its impact on channel capacity estimation," in *Proc. IEEE GLOBECOM*, pp. 4559-4564, Nov. 2007.

[147] F. L. Walls and D. W. Allan, "Measurements of frequency stability," in *Proc. IEEE*, vol. 74, no. 1, pp. 162-168, Jan. 1986.

[148] “Universal Mobile Telecommunications System (UMTS);Base Station (BS) radio transmission and reception (FDD) (3GPP TS 25.104 version 12.5.0 Release 12),” ETSI TS 125 104 V12.5.0., Jan2015.

[149] MITEQ Fibre Optic Transceiver manual, [Online]. Available: https://www.miteq.com/docs/MITEQ_FiberOptic_c40.pdf, visited on Feb. 2016.

[150] Q. H. Chu, J. M. Conrat, and J. Cousin, “Propagation path loss models for LTE-advanced urban relaying systems,” *IEEE APSURSI Symp*., pp. 2797-2800, July 2011.

[151] Q. H. Chu, J. M. Conrat, and J. Cousin, “On the impact of receive antenna height in a LTE-Advanced relaying scenario,” in *Proc. IEEE EUWIT*, pp. 129-132, Sep. 2010.

[152] V. S. Abhayawardhana, I. J. Wassell, D. Crosby, M. P. Sellars, and M. G. Brown, “Use of Random Building Height model for fixed wireless access systems in urban and suburban environments,” *IEEE IST Mobile and Wireless Communications Summit*, Germany, June 2005.

[153] C. L. Hong, I. J. Wassell, G. Athanasiadou, S. Greaves, and M. Sellars, “Wideband channel measurements and characterisation for broadband wireless access,” in *Proc. IEEE ICAP*. vol. 1, pp.429-432, April 2003.

[154] I. Rodriguez, C. Coletti, and T. B. Sorensen, “Evaluation of potential relay locations in an urban macro-cell scenario with applicability to LTE-A,” in *Proc. IEEE VTC*, pp. 1-5, May 2012.

[155] M. Coldrey, L. Manholm, M. Hashemi, S. Falahati, A. Derneryd, and U. Engstrom, “Non-line-of-sight microwave backhaul in heterogeneous networks,” in *Proc. IEEE VTC*, pp. 1-5, Sep. 2013.

[156] W. Joseph, L. Roelens, and L. Martens, “Path loss model for wireless applications at 3500 MHz,” *IEEE APS Symp.*, pp. 4751-4754, July 2006.

[157] C. L. Hong, I. J. Wassell, G. E. Athanasiadou, S. Greaves and M. Sellars, "Wideband tapped delay line channel model at 3.5 GHz for broadband fixed wireless access system as function of subscriber antenna height in suburban environment," in *Proc. IEEE ICSP*, vol. 1, pp. 386-390, Dec. 2003.

[158] J. J. Egli, “Radio Propagation above 40 MC over irregular terrain,” in *Proc. of IEEE IRE* , vol. 45, no. 10, pp.1383-1391, Oct. 1957.

[159] S. R. Saunders, B. G. Evans, “The spatial correlation of shadow fading in macrocellular mobile radio systems,” IEEE Colloq. Propag. Aspects of Future Mobile Syst., pp. 1-6, Oct 1996.

[160] R. Fraile, J. Nasreddine, N. Cardona, and X. Lagrange, “Multiple diffraction shadowing simulation model,” *IEEE Comm. Lett.*, vol. 11, no. 4, pp. 319–321, Apr. 2007.

[161] V. Erceg, L. J. Greenstein, S. Y. Tjandra, S. R. Parkoff, A. Gupta, B. Kulic, A. A. Julius, and R. Bianchi, “An empirically based path loss model for wireless channels in suburban environments,” *IEEE J. Sel. Areas Commun.*, vol. 17, no. 7, pp. 1205-1211, July 1999.

[162] J. Turkka, and M. Renfors, “Path loss measurements for a non-line-of-sight mobile-to-mobile environment,” in *Proc. IEEE ITST*, pp.274-278, Oct. 2008.

[163] H. L. Bertoni, and L. R. Maciel, “Theoretical prediction of slow fading statistics in urban environments,” in *Proc. IEEE ICUPC*, pp. 1-4, Oct 1992.

[164] S. Saunders, *Antennas and propagation for wireless communication systems*, England, Wiley, 2007, ch. 9.

[165] H. Chung and H. Bertoni, “Range-dependent path-loss model in residential areas for the VHF and UHF bands,” *IEEE Trans. Antennas Propag.*. vol. 50, pp.1-11, Jan. 2002.

[166] K. Konstantinou, S. Kang, T. Brown, and C. Tzaras, “Measurement and modelling of the propagation channel between low-height terminals,” *IET Microw. Antennas Propag.,* vol. 5, no. 4,pp.412-418, March 2011.

[167] K. Konstantinou, S. Kang, and C. Tzaras, “A measurement-based model for mobile-to-mobile UMTS links,” in *Proc. IEEE VTC*, pp. 529-533, April 2007.

[168] T. B. Welch, J. R. Wood, R. W. McParlin, L. K. Schulze, T. P. Flaherty, S. G. Carlone Hanson, R. J. Cahill, and R. A. Foran, “Very near ground RF propagation measurements for wireless systems,” in *Proc. IEEE VTC*, vol. 3, pp. 2556-2558, April 2000.

[169] S. R. Saunders and F. Bonar, “Mobile radio propagation in built-up areas: a numerical model of slow fading,” in *Proc. IEEE VTC*, pp. 295-300, May 1999.

[170] C. Chrysanthou and H. L. Bertoni, “Variability of sector averaged signals for UHF propagation in cities,” *IEEE Trans. Veh. Tech.*, vol. 39, no. 4, pp. 352-358, Nov. 1990.

[171] R. Fraile, J. F. Monserrat, D. Calabuig, and N. Cardona, “Analysis and validation of a shadowing simulation model suited for dynamic and heterogeneous wireless networks,” in *Proc. IEEE WCNC* , pp. 1-5, April 2010.

[172] F. Fuschini, V. Degli-Esposti, and G. Falciasecca, “A statistical model for over rooftop propagation,” *IEEE Trans. Antennas Propag.*, vol. 52, no. 1, pp. 230–239, Jan. 2004.

[173] M. Barbiroli, C. Carciofi, G. Falciasecca, M. Frullone, P. Grazioso, and A. Varini, “A new statistical approach for urban environment propagation modeling,” *IEEE Trans. Veh. Technol*, vol. 51, no. 5, pp. 1234-1241, Sep. 2002.

[174] S. Saunders and F. Bonar, “A propagation model for slow fading in urban mobile radio systems,” in *Proc. IEEE ICAP* , vol. 1, pp. 160–163, April 1991.

[175] L. Piazzi, and H. L. Bertoni, “On screen placement for building representation in urban environments considering 2D multiple diffraction problems,” in *Proc. IEEE VTC* , vol.4, pp. 1977-1981, Sep. 1999.

[176] S. R. Saunders, and F. R. Bonar, “Prediction of mobile radio wave propagation over buildings of irregular heights and spacings,” *IEEE Trans. Antennas Propag.*, vol. 42, no. 2, pp. 137-144, Feb. 1994.

[177] J. V. Rodriguez, M. J. Garcia-Martinez, J. M. Molina-Garcia-Pardo, and L. Juan-Llacer,

"On building modeling for multiple diffraction analysis in urban environments considering spherical-wave incidence," in *Proc. IEEE ISWCS*, pp. 60-62, 6-8 Sep. 2006.

[178] L. E. Vogler, "The attenuation of electromagnetic waves by multiple knife-edge diffraction," *NITA, Tech. Rep.*, Boulder, Colourado, Oct. 1981.

[179] J. Deygout, "Correction factor for multiple knife-edge diffraction," *IEEE Trans. Antennas Propag.* , vol. 39, no. 8, pp. 1256-1258, Aug. 1991.

[180] J. Walfisch, and H. L. Bertoni, "A theoretical model of UHF propagation in urban environments," *IEEE Trans. Antennas Propag.*, vol. 36, no. 12, pp 1788-179, 1988.

[181] L. R. Maciel, H. L. Bertoni, and H. Xia, "Unified approach to prediction of propagation over buildings for all ranges of base station antenna height," *IEEE Trans. Veh. Tech.*, vol. 42, no. 1, pp. 41-45, Feb. 1993.

[182] H. Xia, "A simplified analytical model for predicting path loss in urban and suburban environments," *IEEE Trans. Veh. Tech,* vol. 46, no. 4, pp. 1040-1046, Nov 1997.

[183] J. M. Hernando, "Comments on A simplified analytical model for predicting path loss in urban and suburban environments," *IEEE Trans. Veh. Tech*, vol. 48, no. 5, pp. 1740-1740, Sep. 1999.

[184] D. Crosby, S. Greaves, and A. Hopper, "The effect of building height variation on the multiple diffraction loss component of the Walfisch-Bertoni model," in *Proc. IEEE PIMRC*, vol. 2, pp. 1805-1809, Sep. 2003.

[185] J. H. Whitteker, "Fresnel-Kirchhof theory applied to terrain diffraction problems", *Radio Sci.*, vol. 25, no. 5, pp. 837-851, 1990.

[186] L. Piazzi and H. Bertoni, "A path loss formulation for wireless applications considering terrain effects for urban environments," in *Proc. IEEE VTC*, pp. 159–161, May 1998.

[187] L. Piazzi and H. L. Bertoni, "Effect of terrain on path loss in urban environments for wireless applications," *IEEE Trans. Antennas Propag.*, vol. 46, pp. 1138–1147, Aug. 1998.

[188] K. Allsebrook and J. D. Parson, "Mobile radio propagation in British cities at frequencies in the VHF and UHF Bands," *IEEE Trans. Veh. Tech..*, vol. 26, pp. 313-322, Nov. 1977.

[189] F. Ikegami, S. Yoshida, T. Takeuchi, and M. Umehira, "Propagation factors controlling mean field strength on urban streets,"4 *IEEE Trans. Antennas Propag.*, vol. 32, pp. 822-829, Aug. 1980.

[190] F. Ikegami, T. Takeuchi, and S. Yoshida, “Theoretical prediction of mean field strength for urban mobile radio,” *IEEE Trans. Antennas Propag.*, vol. 39, pp. 299-302, Mar. 1991.

[191] L. B. Felsen and N. Marcuvitz, *Radiation and Scattering of Waves,* Englewood Cliffs, NJ, Prentice-Hall, 1973, pp. 652-665.

[192] H. L. Bertoni, W. Honcharenko, L. R. Macel, and H. Xia, “UHF propagation prediction for wireless personal communications,” in *Proc. IEEE* , vol.82, no.9, pp. 1333-1359, Sep. 1994.

[193] “Prediction methods for the terrestrial land mobile service in the VHF and UHF bands,” ITU-R P.529-2–7, [Online]. Available: https://www.itu.int/dms_pubrec/itu-r/rec/p/R-REC-P.529-2-199510-S!!PDF-E.pdf, visited on Dec. 2014.

[194] M. A. Alim, M. M. Rahman, M. M. Hossain, and A. Al-Nahid, “Analysis of large scale propagation models for mobile communications in urban areas,” *IJCSIS J.* , vol. 7, no. 1, 2010.

[195] W. C. Jakes, *Microwave Mobile Communications*, NY, IEEE Press, 1994.

[196] “Residential - mixed housing urban and suburban zones: Proposed Auckland Unitary Plan: Fact Sheet” Auckland Council [Online]. Available: http://www.aucklandcouncil.govt.nz/EN/planspoliciesprojects/plansstrategies/unitaryplan/Documents/Key%20topics%20in%20detail/upkeytopicsmixedhousingurbanandsuburbanzones.pdf. visited on Mar. 2016.

[197] A Guran , R Mittra , P J Moser , *Electromagnetic wave interactions,* World Scientific, ch. 3, pp. 93-137

[198] G. J. McLachlan and D. Peel, *Finite mixture models, Wiley Series in Probability and Statistics*, New York, Wiley, 2000.

[199] E. T. Lee and J. W. Wang, *Statistical methods for survival data analysis*, Third ed., New York, John Wiley &Sons, 2003.

[200] J. M. Nemec, and A. F. L. Nemec, “The stellar population of galaxies,” *IAU Symp.*, Kluwer Academic Press, 1992.

[201] T. Toda, A.W. Black, and K. Tokuda, “Voice conversion based on maximum-likelihood estimation of spectral parameter trajectory,” *IEEE Trans. Speech Audio Process*, vol. 15, no. 8, pp. 2222-2235, Nov. 2007.

[202] A. P. Dempster, N. M. Laird, and D. Rubin, “Maximum likelihood from incomplete data

via the EM algorithm," *Royal Statistical Society J.,* vol. 39, no. 1, pp. 1–38, 1977.

[203] R. S. Pilla, and B. G. Lindsay, "Alternative EM methods for nonparametric finite mixture models," *Biometrika J.,* vol. 103, pp. 535–550, 2001.

[204] W. Seidel, K. Mosler, and M. Alker, 2000 "A cautionary note on likelihood ratio tests in mixture models," *AISM J.*, vol. 52, pp. 481–487, Sep. 2000.

[205] H. Akaike, "A new look at the statistical model identification," *IEEE Trans. Autom. Control, ,* vol. 19, no. 6, pp. 716-723, Dec 1974.

[206] "G. Schwarz, "Estimating the dimension of a model," *AISM J.*, vol. 6, no. 2, pp. 461–464, Mar. 1978.

[207] K. A. Ashman, C. M. Bird, and S. E. Zepf, "Detecting bimodality in astronomical dataset," *Astron.J.*, vol. 108, pp. 2348-2361, 1994.

[208] B. Diallo, "Characterization of fixed wireless channels for use in distribution automation networks," M.A.Sc. Thesis, Dept. Elect. Eng., UBC, Vancouver, Canada, BC, 2011.

[209] Q. Yu, and R. J. Johnson, "Smart grid communications equipment: EMI, safety, and environmental compliance testing considerations," *Bell Labs Tech* . J., 16: 109–131.

Appendix - Measurement of Shadow Fading in a Suburban Macrocell Environment

In this appendix, we describe the measurement setup and the results which were obtained by some of former students of UBC Radio Science Lab during studying the effect of terminal antenna height on path loss component and SF location variability [208]. There was a 1.9GHz antennas mounted on the roof of our van adjustable at terminal height of 2 m, 5 m and 7 m, respectively. The measurement data was collected at 80 fixed locations at suburban neighborhoods with generally flat terrain, light to moderate foliage and one or two-storey houses between 300 m and 3 km from BC Hydro's Edmonds facility in Burnaby, BC (see Figure A-1). The building density at the site was 100 structures per square kilometer with an average separation between structures of 20 m. The measured data were collected in the form of three successive 120-second sweeps. Each sweep yielded 501 samples for a total of 1503 received signal strength samples at each location. Further detail of our tri-band CW channel sounder and data collection methodology can be found in [208].

The recorded data were linearly averaged to yield the average path gain at each location and at each terminal height by estimating the regression line that best fits the measured data in a least squares sense (see Figure A-2 see and Figure A-3). As expected, the path loss component was decreasing function of terminal antenna height. While we were expecting the same behavior for SF location variability, we observed unexpected behavior such that by increasing terminal height it was increasing and after a point it started decreasing (as shown in Figure A-4). This is consistent with our proposed SF standard deviation model in which it increases with terminal height until after passing the mean building height it starts decreasing. Looking into previous works, such behavior was observed in previous measurement-based studies but it was ignored totally. This motivated us to look into it with more rigorous simulation approach using general model of similar suburban environment as is described in chapter 6.

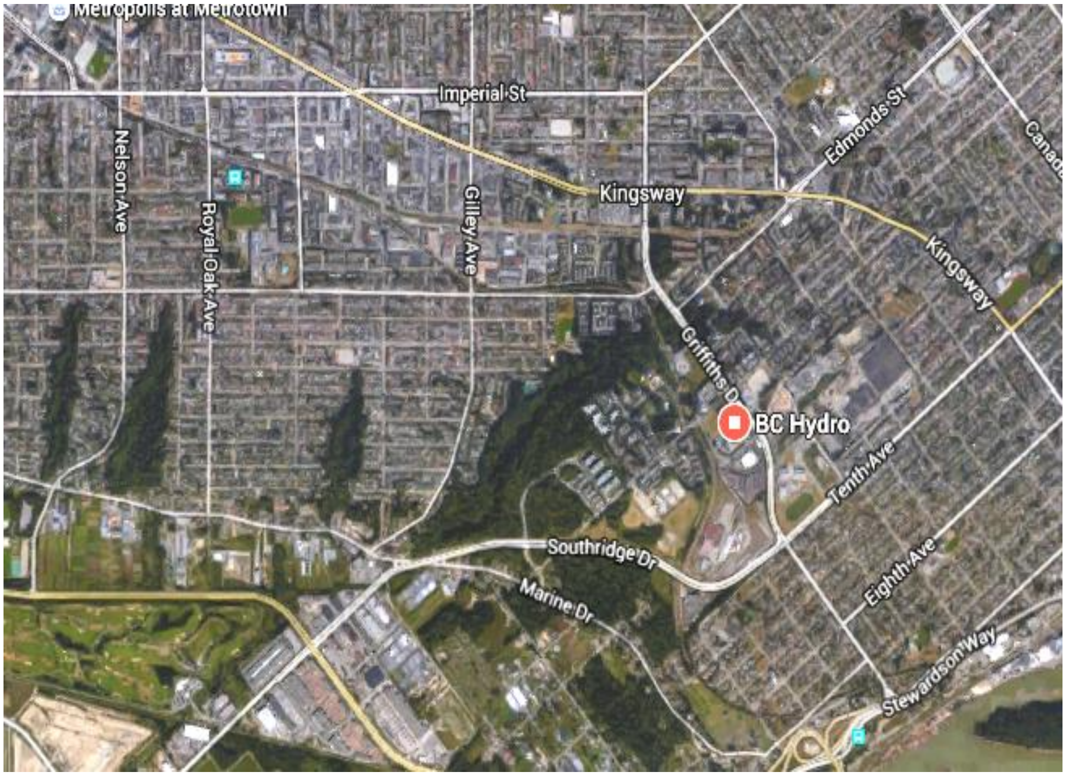

Figure A- 1: Measurement site view (BC Hydro building as the location of transmitter antenna)

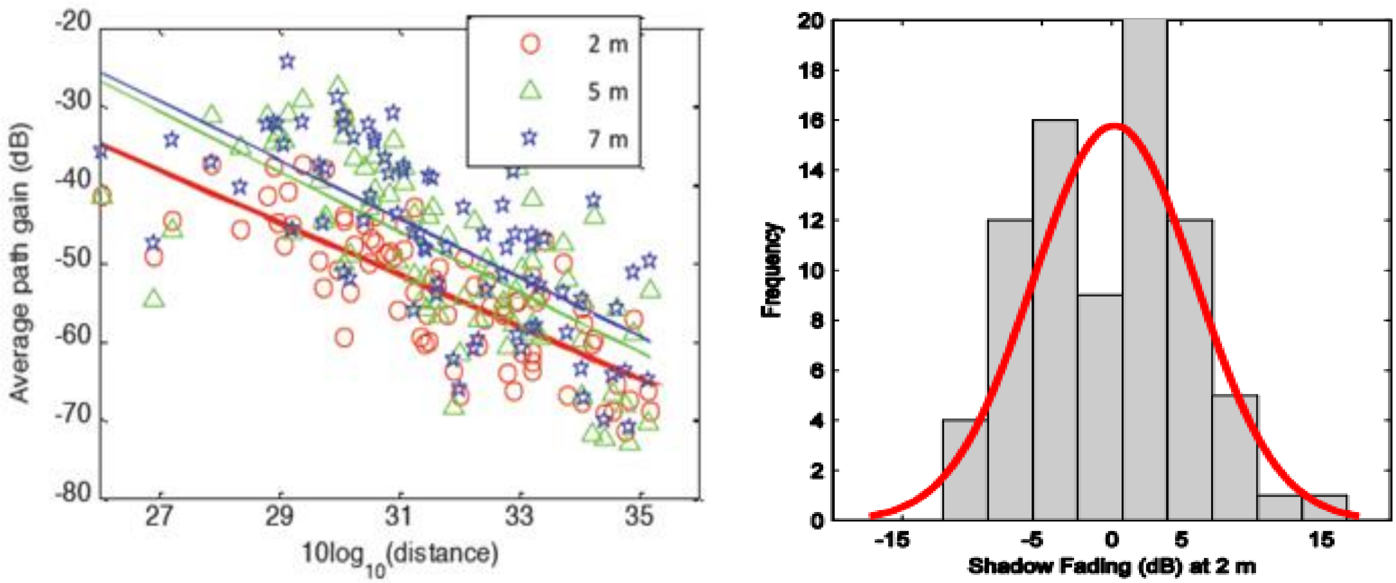

(a) (b)

Figure A- 2: (a) Measured path gain versus distance for 2, 5 and 7 m terminal heights (b) Measured Shadowing distribution at terminal height of 2 m.

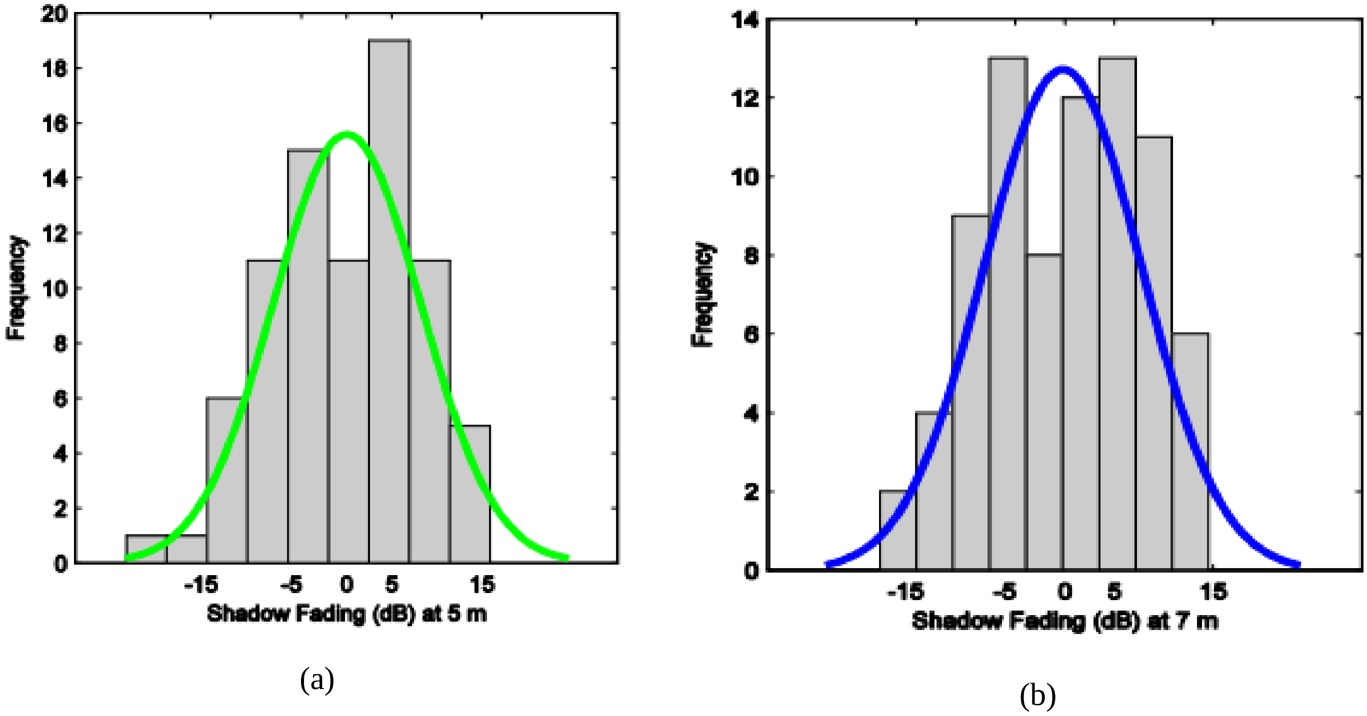

Figure A- 3: Measured Shadowing distribution at terminal height of (a) 5 m. (b) 7 m.

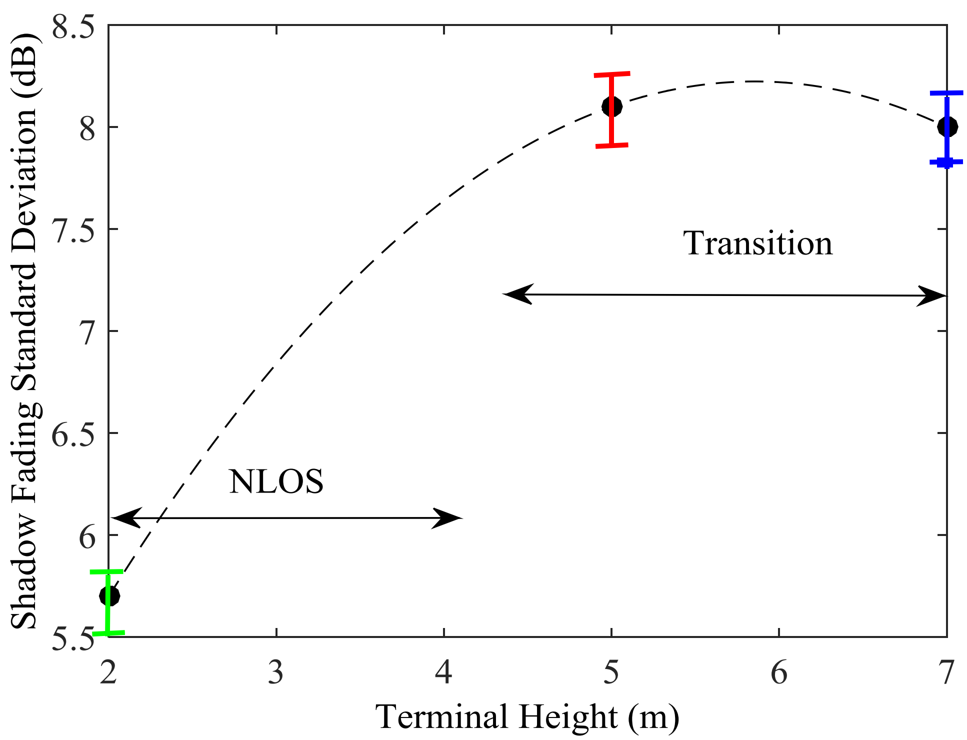

Figure A- 4: Measured Shadow Fading standard deviation variation with terminal height.